Searching for Dark Matter with Boosted Higgs Decays in Proton-Proton Collisions at $\sqrt{s} = 13$ TeV with the ATLAS Detector

Nikola Lazar Whallon

A dissertation
submitted in partial fulfillment of the
requirements for the degree of

Doctor of Philosophy

University of Washington

2018

Reading Committee:

Shih-Chieh Hsu, Chair

Gordon Watts

Stephen Sharpe

Program Authorized to Offer Degree:
Physics

University of Washington

Abstract

Searching for Dark Matter with Boosted Higgs Decays in Proton-Proton Collisions at $\sqrt{s} = 13$ TeV with the ATLAS Detector

Nikola Lazar Whallon

Chair of the Supervisory Committee:
Dr. Shih-Chieh Hsu
Physics

If Dark Matter particles interact with Standard Model particles, it could be possible to pair produce Dark Matter particles in association with a detectable Standard Model particle at a collider such as the LHC. If this associated particle is a Higgs boson, the process is called "mono-Higgs," since the resulting signature is a single Higgs boson balanced by missing energy from the undetected Dark Matter particles. Various Dark Matter models predict that this process could result in very boosted Higgs bosons that, if they decay to a pair of b-quarks, are reconstructed as jets using boosted Higgs tagging techniques. This thesis presents the results of a mono-Higgs search using 79.8 fb^{-1} of proton-proton collision data collected at a center-of-mass energy of 13 TeV by the ATLAS detector. The observed data are found to be consistent with the expected Standard Model backgrounds. The results are interpreted and exclusion limits are set using a Z' two-Higgs-doublet model where the pseudo-scalar Higgs particle, A, couples to Dark Matter. In order to increase the sensitivity reach of the search, new boosted Higgs tagging techniques are explored and a variable radius track jet Higgs tagging technique is employed.

TABLE OF CONTENTS

LIST OF FIGURES

LIST OF TABLES

ACKNOWLEDGMENTS

I would like to thank the many supportive friends, family, and professional colleagues who have enabled me to carry out the research presented here and to earn my degree. I would like to thank my advisor, Shih-Chieh Hsu, whose daily hard work and energetic spirit has inspired and motivated me to carry out this research. For their superb mentor-ship and personal support, I would like to thank Sam Meehan and Dan Guest. Special thanks to Qi Zeng, Nurfikri Norjoharuddeen, and Jie Yu whose close collaboration and shared experiences on Higgs tagging projects I benefited from and enjoyed. I would like to thank Karolos Potamianos, Hide Oide, and Timon Heim for the many technical discussions of software and hardware while working on the ATLAS Pixel detector.

I would like to thank the mono-Higgs analysis team for working together to collectively achieve the results presented in this thesis. In particular, I would like to thank Veronica Fabiani for her work on variable radius track jet b-tagging, as well as our collaborative work on the mono-Higgs analysis framework migration; I would like to thank Andrea Matic for her contributions to the 1-lepton Control Region studies, and Dilia Maria Portillo Quintero for her contributions to the 1-lepton Control Region studies and multi-jet background estimation using a new measure of the missing transverse energy significance; I would like to thank Cheng-Hsin Han, Yun-ju Lu, and Po-Shan Shih for their contributions to the 2-lepton Control Region studies; and I would like to give a special thanks to Philipp Gadow for his crucial role in software maintenance and many critical mono-Higgs studies.

I would like to thank my Ph.D. committee members, who have worked around my strange and tight schedules. I would like to give a special thanks to Paul DeStefano and Nicholas Dreyer, whose company and conversations about physics research frequently gave me motivation. I would also like to thank my parents for their academic, research, and life advice throughout my education.

I would especially like to thank my wife, Yumi Shinobe Whallon, who has graciously endured years of complex travel arrangements and long distances necessary to carry out this work.

DEDICATION

to my parents, Robert Whallon and Nada Rakić

Chapter 1

INTRODUCTION

Dark Matter is one of the most profound problems in physics today. While compelling, if not definitive, evidence for its existence via its gravitational effects has been growing for at least a century, the particle nature of Dark Matter remains a mystery. Indeed, if Dark Matter is only capable of interacting gravitationally, uncovering its particle nature may be as difficult as uncovering the particle nature of gravity - a feat deemed virtually impossible for current experiments and most graviton theories [1]. However, there are several well motivated theories and models that predict Dark Matter interacting with Standard Model particles weakly, perhaps via a new mediator. If this is the case, then there is good reason to search for Dark Matter production in high energy collisions, such as those provided by the Large Hadron Collider.

Presented in this thesis is a search for Dark Matter produced in association with a Higgs boson at the Large Hadron Collider with the ATLAS detector [2]. The Higgs boson decays into two b-quarks that hadronize to form b-hadrons. Several Dark Matter models predict that this signature could result in Higgs bosons with relatively large transverse momenta,[1] resulting in highly collimated b-hadrons. Novel techniques to reconstruct the $h \to b\bar{b}$ decay have been developed and applied to the search to improve signal sensitivity.

Crucial to the identification of b-hadrons is the ability to reconstruct secondary vertices in events where the b-hadron travels a finite distance before decaying. Secondary vertex reconstruction is greatly aided by the tracking precision of pixel detectors. Work on upgrading the current ATLAS Pixel detector and research and development work on the next-generation ATLAS Pixel detector are thus also presented.

This thesis is organized as follows. Chapter 2 introduces the Standard Model of particle physics and our current understanding of the fundamental nature of the universe. Chap-

[1] such particles are said to be "boosted"

ter 3 introduces the concept of Dark Matter, one of the most important missing pieces of our knowledge of the universe, and how one might search for it in a collider experiment. Chapter 4 introduces the Large Hadron Collider and the ATLAS detector used to carry out this Dark Matter search. Chapter 5 describes the Monte Carlo and data samples used to carry out this search. Chapters 7 and 8 describe the object and event selection of the analysis. Chapter 9 describes how Standard Model backgrounds are estimated by the analysis. Chapter 10 describes the sources of experimental and modelling uncertainties. Chapter 11 presents the final results of the analysis and Chapter 12 contains concluding remarks on the research presented here.

The Author's Contributions

ATLAS is one of the largest scientific experiments in the world, and as such, numerous people are involved in the design, construction, operation, and performance studies of the ATLAS detector, and numerous people are involved in the analysis of the data collected by the ATLAS detector. Specific contributions of the author of this thesis to the mono-Higgs search include simplified Dark Matter model recommendations, recommendations for and validity studies of Effective Field Theory Dark Matter models [3], development and maintenance of simulated samples, development and performance studies of boosted Higgs tagging techniques, including the variable radius track jet technique chosen for use in the analysis [4] [5], critical computational optimizations of the variable radius clustering technique, signal and control region studies comparing data and Monte-Carlo simulation, signal acceptance and efficiency studies that aim to understand the improvement to the analysis of the variable radius track jet boosted Higgs tagging technique, and final interpretations of the search results using Dark Matter models [6] [7] [8] [2]. Additional service work in operating and upgrading the ATLAS Pixel detector, as well as research and development work targeting the next generation ATLAS Pixel detector [9], were also carried out.

Chapter 2

THE STANDARD MODEL OF PARTICLE PHYSICS

The Standard Model (SM) of particle physics describes the elementary particles of the universe and how they interact. There are some glaring omissions in the Standard Model, such as the lack of a description of gravitational interactions or the existence of Dark Matter, but for the most part, the Standard Model has had great success in describing the fundamental building blocks of the universe. The most recently confirmed Standard Model particle, the Higgs boson, was discovered in 2012 [10] [11] by both the ATLAS and the CMS experiments, and is used as a tool in this thesis to search for potential Dark Matter signatures.

This Chapter introduces the Standard Model and is organized as follows. Section 2.1 introduces all of the Standard Model particles. Section 2.2 describes basic interactions of Standard Model particles. Section 2.3 describes the Lagrangian formalism of the Standard Model before spontaneous symmetry breaking, and finally, Section 2.4 describes the Higgs mechanism which is responsible for the masses of (most) Standard Model particles. For more details of the Standard Model, the Particle Data Group provides annual reviews which are great references [12].

2.1 Standard Model Particles

Table 2.1 summarizes the elementary particles of the Standard Model. Leptons and quarks make up the elementary fermions, while the photon, gluon, the W, the Z, and the Higgs particles make up the elementary bosons. Fermions are defined as particles whose spin is a half integer ($\frac{1}{2}$, $\frac{3}{2}$, etc), while bosons are defined as particles whose spin is an integer value. There are three fundamental forces defined by the Standard Model: the electromagnetic force, mediated by the photon, the strong force, mediated by the gluon, and the weak force, mediated by the W and Z bosons. However, the Higgs boson can also be thought of as a

Table 2.1: A table summarizing the elementary particles of the Standard Model. In each cell, the upper left corner indicates the particle's most commonly used symbol, the upper right corner indicates the particle's mass, the lower left corner indicates the particle's electric charge, and the lower right corner indicates the particle's spin. Masses for the u-, d-, c-, s-, and b-quarks are given in the $\overline{\text{MS}}$ scheme at a renormalization scale of $\mu = 2$ GeV [12]. The t-quark mass is quoted from experimental measurements [13].

	Fermion Gen I		Fermion Gen II		Fermion Gen III		Bosons	
Leptons	$\boldsymbol{e}$	511 KeV	$\boldsymbol{\mu}$	106 MeV	$\boldsymbol{\tau}$	1.78 GeV	$\boldsymbol{\gamma}$	0
	-1	$1/2$	-1	$1/2$	-1	$1/2$	0	1
	$\boldsymbol{\nu_e}$	< 2.2 eV	$\boldsymbol{\nu_\mu}$	< 170 KeV	$\boldsymbol{\nu_\tau}$	< 15.5 GeV	$\boldsymbol{W^\pm}$	80.4 GeV
	0	$1/2$	0	$1/2$	0	$1/2$	± 1	1
Quarks	$\boldsymbol{u}$	2.15 MeV	$\boldsymbol{c}$	1.28 GeV	$\boldsymbol{t}$	173 GeV	$\boldsymbol{Z}$	91.2 GeV
	$2/3$	$1/2$	$2/3$	$1/2$	$2/3$	$1/2$	0	1
	$\boldsymbol{d}$	4.70 MeV	$\boldsymbol{s}$	93.8 MeV	$\boldsymbol{b}$	4.18 GeV	$\boldsymbol{g}$	0
	$-1/3$	$1/2$	$-1/3$	$1/2$	$-1/3$	$1/2$	0	1
							$\boldsymbol{h}$	125 GeV
							0	0

force mediator, and extensions to the Standard Model often consider a new boson, known as the graviton, which mediates the gravitational force.

The electron, the muon, and the tau are referred to as the "charged leptons," as they possess electric charge, and are often denoted by the character l in this thesis. The electron neutrino, muon neutrino, and tau neutrino do not possess electric charge, and are referred to as the "lepton neutrinos" (or just "neutrinos") and are often denoted by ν_l (or just ν when the generation need not be specified). Occasionally, in the context of the ATLAS experiment, "leptons" refers only to electrons and muons, however this usage is avoided as much as possible in this thesis.

Quarks and charged leptons both carry electric charge, with quarks carrying $\pm\frac{1}{3}$ or $\pm\frac{2}{3}$ and the charged leptons carrying ± 1 electric charge.[2] This means that they can interact via the electromagnetic force mediated by the photon. Lepton neutrinos do not carry electric charge and thus do not participate in electromagnetic interactions. Quarks additionally carry color charge, allowing them to interact via the strong force mediated by the gluon.

Quarks, charged leptons, and lepton neutrinos can all interact via the weak force mediated by the W^+, W^-, and Z vector bosons. Quarks and charged leptons also couple to the Higgs boson. This coupling is the origin of the mass terms in the quark and charged lepton Lagrangians, and will be discussed more in Section 2.4. Neutrinos do not couple to the Higgs boson in the Standard Model, and are massless in the Standard Model.

The force-mediating bosons can also interact with each other, and sometimes with themselves. An overview of Standard Model interactions is given in Section 2.2.

2.2 The Standard Model Interactions

Standard Model interactions can be summarized by interaction vertices that represent particle couplings. These vertices are assigned a vertex factor proportional to a coupling constant. Table 2.2 summarizes the coupling constants of the three Standard Model forces, quoting their values for low energy particle interactions.

At low energies, the coupling constant of the strong force, mediated by the gluon, is

[2] ± 1 unit of this elementary electric charge is equivalent to $\pm 1.602 \times 10^{-19}$ Coulombs in SI units

Table 2.2: A table summarizing coupling constants of the three Standard Model forces. While the coupling constant of the weak force is, in fact, larger than the coupling constant of the electromagnetic force, at low energies, the effective strength of the weak force is kinematically suppressed by the heavy W or Z mass which shows up in the denominator of the propagator term when calculating cross sections using Feynman diagrams.

Force	Mediator(s)	Coupling Constant	Approximate Value
Strong	g	α_s	10^0
Electromagnetic	γ	α	10^{-2}
Weak	$W^{\pm}, Z$	α_W	10^{-1}

approximately two orders of magnitude stronger than the coupling constant of the electromagnetic force, mediated by the photon. The gluon and the photon are both massless, however, the W and Z bosons that mediate the weak force have large masses which suppress the strength of weak interactions. Thus, while the weak coupling constant is larger than the electromagnetic coupling constant, the weak force is much weaker than the electromagnetic force at low energies. The strengths of these coupling constants change for high energies, and at high enough energies the weak force becomes effectively stronger than the electromagnetic force. The interaction vertices of these three forces are summarized in the following subsections.

2.2.1 Quantum Electro Dynamics

Quantum electro dynamics (QED) is characterized by the QED vertex, shown in Figure 2.1. The vertex shows a charged particle and its anti-particle interacting with a photon, with interaction strength proportional to $\sqrt{\alpha}$.

2.2.2 Quantum Chromo Dynamics

Quantum chromo dynamics (QCD) describes the interactions between particles with color charge. The interaction vertices of QCD are shown in Figure 2.2. Quarks and gluons can

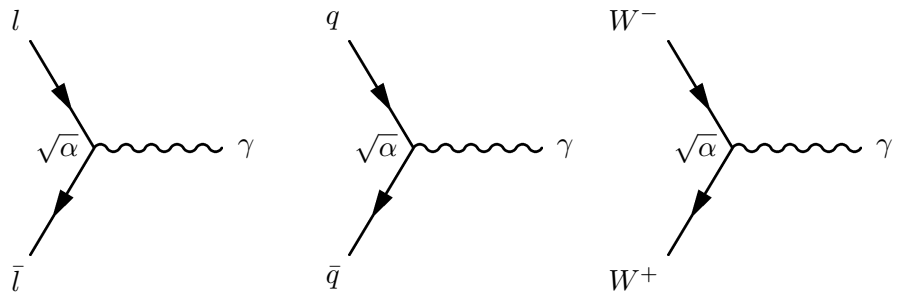

Figure 2.1: The quantum electro dynamics vertices.

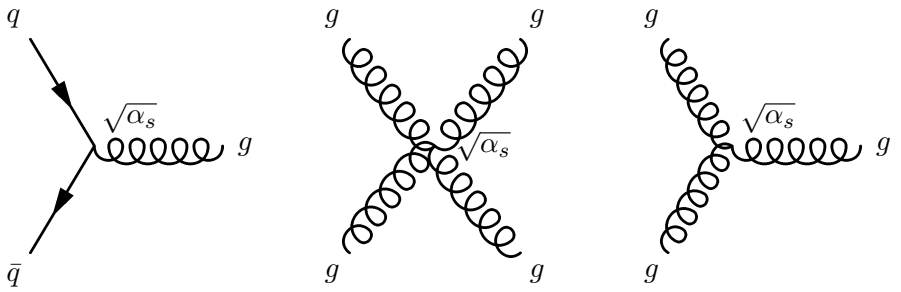

Figure 2.2: The quantum chromo dynamics vertices.

carry colors red, green, or blue.[3] However, QCD vertices must be "colorless" - that is, there must be equal parts red, green, and blue at each QCD vertex. A red anti-quark/anti-gluon can be treated as having both the colors green and blue, and similarly for green anti-quarks/anti-gluons and blue anti-quarks/anti-gluons. Since gluons themselves carry color-charge, gluons can interact directly with other gluons.

2.2.3 Weak Interactions

The neutral weak interaction vertices are shown in Figure 2.3. The Z boson couples to particle/anti-particle pairs of quarks and leptons. Indeed, the Z coupling to quarks and charged leptons mirrors the QED couplings.

The charged weak interaction vertices are shown in Figure 2.4. The leptonic vertices

[3] these "colors" are to be thought of simply as labels for charge - just as there are two types of electric charge ("+" and "−"), there are three types of color charge ("red," "green," and "blue")

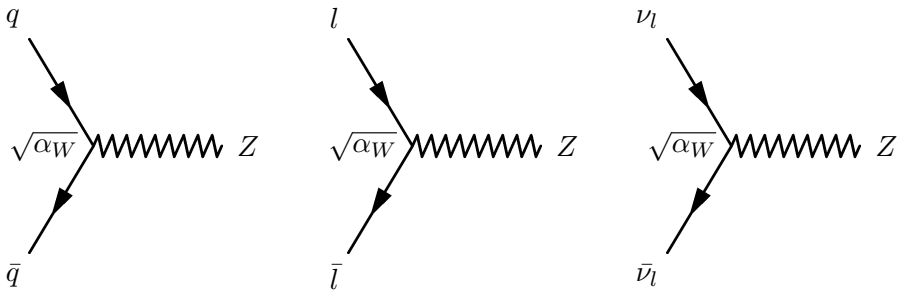

Figure 2.3: The neutral weak interaction vertices.

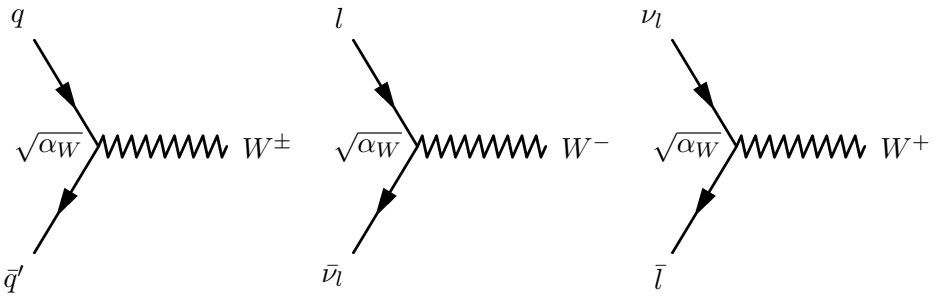

Figure 2.4: The charged weak interaction vertices.

require the interacting charged leptons and lepton neutrinos to be matched, e.g., electrons and anti-electron neutrinos, anti-muons and muon neutrinos, etc.

The criteria for quark-W vertices are somewhat different - any pairing of quarks in a quark-W vertex is acceptable as long as charge conservation and kinematic constraints are met. However, the strength of the vertex factor will depend on the pairing of quarks according to the Cabibbo-Kobayashi-Maskawa (CKM) matrix [14], which describes the mixing of quark mass eigenstates with respect to quark weak eigenstates, as shown in the following equation:

$$\begin{pmatrix} d' \\ s' \\ b' \end{pmatrix} = \begin{pmatrix} V_{ud} & V_{us} & V_{ub} \\ V_{cd} & V_{cs} & V_{cb} \\ V_{td} & V_{ts} & V_{tb} \end{pmatrix} \begin{pmatrix} d \\ s \\ b \end{pmatrix} \tag{2.1}$$

where

$$\begin{pmatrix} V_{ud} & V_{us} & V_{ub} \\ V_{cd} & V_{cs} & V_{cb} \\ V_{td} & V_{ts} & V_{tb} \end{pmatrix} \tag{2.2}$$

is the CKM matrix, the "primed" quarks are the quarks' weak eigenstates, and the "unprimed" quarks are the quarks' mass eigenstates. The magnitude of the V_{ij} is proportional to the strength of the mixing. The approximate V_{ij} magnitudes are shown in the following equation.

$$\begin{pmatrix} |V_{ud}| & |V_{us}| & |V_{ub}| \\ |V_{cd}| & |V_{cs}| & |V_{cb}| \\ |V_{td}| & |V_{ts}| & |V_{tb}| \end{pmatrix} \approx \begin{pmatrix} 0.974 & 0.227 & 0.004 \\ 0.227 & 0.973 & 0.042 \\ 0.008 & 0.042 & 0.999 \end{pmatrix} \tag{2.3}$$

Since $|V_{ud}| > |V_{us}| > |V_{ub}|$, the following is true about u-quark and W interactions:

$$\sigma_{W^+ \to u\bar{d}} > \sigma_{W^+ \to u\bar{s}} > \sigma_{W^+ \to u\bar{b}} \tag{2.4}$$

Similarly, it follows that:

$$\sigma_{W^+ \to c\bar{s}} > \sigma_{W^+ \to c\bar{d}} > \sigma_{W^+ \to c\bar{b}} \tag{2.5}$$

and:

$$\sigma_{t \to bW^+} > \sigma_{t \to sW^+} > \sigma_{t \to dW^+} \tag{2.6}$$

The weak interaction is thus unique in that it is the only interaction which has the ability to change quark generations with a single vertex. However, the physics implied by the CKM matrix does not end there. While the CKM matrix contains nine elements, these elements can be reduced to the four parameters θ_{12}, θ_{13}, θ_{23}, and δ_{13}, where the θ parameters are mixing angles (Euler angles) and δ_{13} is a phase which allows for CP-violating processes. The CKM matrix written in terms of these four parameters is shown in the following Equation:

$$\begin{pmatrix} c_{12}c_{13} & s_{12}c_{13} & s_{13} \cdot e^{-i\delta_{13}} \\ -s_{12}c_{23} - c_{12}s_{23} \cdot e^{i\delta_{13}} & c_{12}c_{23} - s_{12}s_{23}s_{13} \cdot e^{i\delta_{13}} & s_{23}c_{13} \\ s_{12}s_{23} - c_{12}c_{23}s_{13} \cdot e^{i\delta_{13}} & -c_{12}s_{23} - s_{12}c_{23}s_{13} \cdot e^{i\delta_{13}} & c_{23}c_{13} \end{pmatrix} \tag{2.7}$$

where s_{ij} and c_{ij} refer to $\sin(\theta_{ij})$ and $\cos(\theta_{ij})$, respectively. The CP-violating phase δ_{13} is of particular interest as CP-violating processes could explain the particle/anti-particle

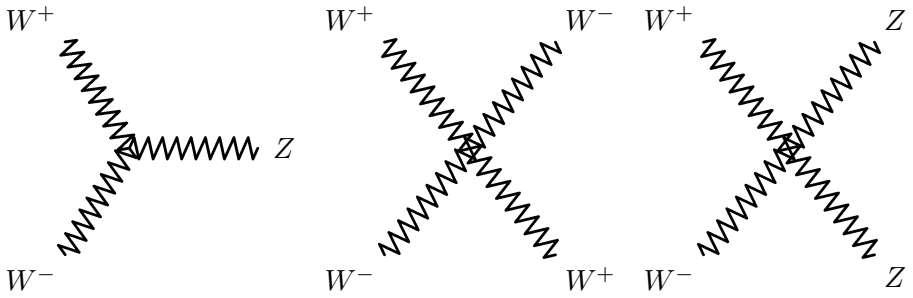

Figure 2.5: Electroweak boson interaction vertices involving just the W and Z vector bosons.

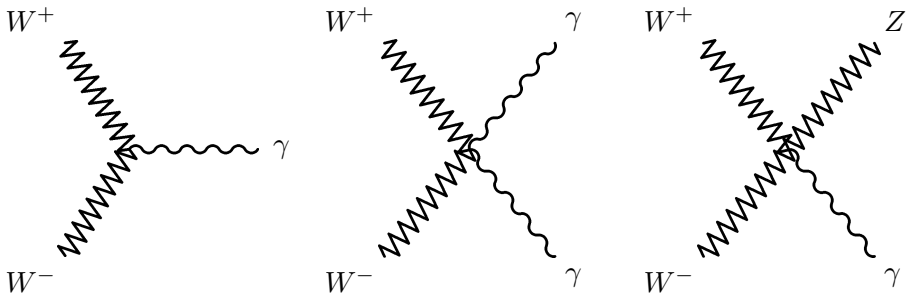

Figure 2.6: Electroweak boson interaction vertices involving a photon.

asymmetry observed in the universe - one of the big problems in physics today. However, the CP-violating processes introduced by the δ_{13} phase are not enough to fully explain this asymmetry.

2.2.4 Electroweak Boson Interactions

Although rare due to very small cross-sections, electroweak bosons can interact in a number of ways with each other. Electroweak boson interaction vertices are shown in Figures 2.5 and 2.6. The cross-sections of these interactions are, however, so small that they are unable to be probed even by the LHC.

2.3 The Standard Model Lagrangian Before Spontaneous Symmetry Breaking

So far, the discussion of the Standard Model has outlined the basic particles and particle interactions without a discussion of the Higgs particle. To understand the significance of

the Higgs field and why it is responsible for the masses of Standard Model particles, it is necessary to discuss the Lagrangian formalism of the Standard Model. This is done in this section with no assumptions made about the potential of the Higgs field. In the following section, Section 2.4, the potential of the Higgs field is then specified, and the consequences described.

To begin, the QCD Lagrangian is written as follows:

$$\mathcal{L}_{\text{QCD}} = \bar{\psi}_i(i(\gamma^\mu D_\mu)_{ij} - m\delta_{ij})\psi_j - \frac{1}{4}G^a_{\mu\nu}G^{\mu\nu}_a \tag{2.8}$$

where G represents the gluon field tensor and ψ the quark Dirac fields. The electroweak (EW) Lagrangian can be written as follows:

$$\mathcal{L}_{EW} = \mathcal{L}_g + \mathcal{L}_f + \mathcal{L}_h + \mathcal{L}_y \tag{2.9}$$

where $\mathcal{L}_g$ is the gauge boson term, $\mathcal{L}_f$ is the fermionic term, $\mathcal{L}_h$ is the Higgs term, and $\mathcal{L}_y$ is the Yukawa term coupling the fermions to the Higgs boson.

The gauge boson term can be written as:

$$\mathcal{L}_g = -\frac{1}{4}B^{\mu\nu}B_{\mu\nu} - \frac{1}{4}W^{i\mu\nu}W^i_{\mu\nu} \tag{2.10}$$

where the four massless vector fields B and $W^i (i = 1, 2, 3)$ will give rise to the four vector bosons γ, Z, W^+, and W^- after spontaneous symmetry breaking.

The Higgs term can be written as:

$$\mathcal{L}_h = (D^\mu\phi)^\dagger(D_\mu\phi) - V(\phi) \tag{2.11}$$

where ϕ is a doublet Higgs field defined to be:

$$\phi = \begin{pmatrix} \phi^+ \\ \phi^0 \end{pmatrix} \tag{2.12}$$

with conjugate:

$$\tilde{\phi} = \begin{pmatrix} \phi^{0*} \\ -\phi^- \end{pmatrix} \tag{2.13}$$

and the form of the Higgs potential, $V(\phi)$, will be left unspecified until Section 2.4.

To write the fermionic and Yukawa terms, it is convenient to break down the fermionic fields for quarks and leptons into their left- and right-handed components. Since fermions are treated as massless before the spontaneous symmetry breaking introduced by the Higgs field, the spin $\frac{1}{2}$ fermions carry a left- or right-handed chirality. Under the Parity operator, which transforms space coordinates $(x, y, z) \rightarrow (-x, -y, -z)$, a left-handed fermion will transform into a right-handed fermion, and vice-versa. Only left-handed fermions interact with the weak bosons, so by separating the lepton and quark fermionic fields into left-handed and right-handed parts, the electric and weak parts of the fermionic Lagrangian can be compartmentalized. This is done by defining the left-handed quark doublet q_L and left-handed lepton doublet l_L as:

$$q_L = \begin{pmatrix} u \\ d \end{pmatrix}_L = \begin{pmatrix} u_L \\ d_L \end{pmatrix} \tag{2.14}$$

$$l_L = \begin{pmatrix} \nu \\ l \end{pmatrix}_L = \begin{pmatrix} \nu_L \\ l_L \end{pmatrix} \tag{2.15}$$

and defining the right-handed quark singlets u_R and d_R and charged lepton singlet e_R. In the Standard Model, neutrinos are assumed to be left-handed, so there is no right-handed lepton neutrino singlet, hence the notation e_R instead of l_R to enforce this point.

To condense notation, the following definitions are also made:

$$\psi_L = q_L + l_L \tag{2.16}$$

$$\psi_R = u_R + d_R + e_R \tag{2.17}$$

Then, the fermion interaction term can finally be written as:

$$\begin{aligned} \mathcal{L}_f &= i\bar{\psi}_L \not{D} \psi_L + i\bar{\psi}_R \not{D} \psi_R + h.c. \\ &= \bar{q}_{L,i} \not{D} q_{L,i} + \bar{l}_{L,i} \not{D} l_{L,i} + \bar{u}_{R,i} \not{D} u_{R,i} + \bar{d}_{R,i} \not{D} d_{R,i} + \bar{e}_{R,i} \not{D} e_{R,i} + h.c. \end{aligned} \tag{2.18}$$

where $h.c.$ refers to the Hermitian conjugate of the proceeding terms and $\not{D}$ is the covariant derivative acting on the left- and right-handed fermionic fields as follows:

$$\not{D} \psi_L = (\partial_\mu + igW_\mu + ig' Y_L B_\mu) \psi_L \tag{2.19}$$

$$\not{D}\psi_R = (\partial_\mu + ig' Y_R B_\mu)\psi_R \tag{2.20}$$

The full Yukawa term can be written as:

$$\mathcal{L}_y = \Gamma^u_{mn}\bar{q}_{L,m}\tilde{\phi}u_{R,n} + \Gamma^d_{mn}\bar{q}_{L,m}\phi d_{R,n} + \Gamma^e_{mn}\bar{l}_{L,m}\phi e_{R,n} + h.c. \tag{2.21}$$

where the m and n are summed over the three fermion generations. After spontaneous symmetry breaking, the scalar Higgs doublet field, ϕ, in the Yukawa term will give rise to fermionic mass terms.

2.4 The Higgs Mechanism and Higgs Interactions

Now, the Higgs potential is specified and the consequences of the potential, the origin of fermion, $W^\pm$ boson, and Z boson masses, is discussed. Renormalizability requires a Higgs potential of the following form:

$$V(\phi) = -\mu^2\phi^\dagger\phi + \lambda(\phi^\dagger\phi)^2 \tag{2.22}$$

with λ a positive constant describing the self-interaction of the ϕ field. For $\mu^2 > 0$, the ground state of this potential does not occur at 0. Instead, there are an infinite number of ground states that satisfy $\phi^\dagger\phi = v^2/2$, where v is referred to as the vacuum expectation value (VEV) of the field. This allows the expectation value of the Higgs doublet field, ϕ, to be written as follows:

$$\langle\phi\rangle = \frac{1}{\sqrt{2}}\begin{pmatrix}0\\ v\end{pmatrix} \tag{2.23}$$

Expanding about the VEV and choosing the unitary guage, the Higgs doublet field can be written as:

$$\phi = \frac{1}{\sqrt{2}}\begin{pmatrix}0\\ v+h\end{pmatrix} = \frac{1}{\sqrt{2}}\begin{pmatrix}0\\ v\end{pmatrix} + \frac{1}{\sqrt{2}}\begin{pmatrix}0\\ h\end{pmatrix} \tag{2.24}$$

with v again being the vacuum expectation value, a constant, and h being the observable singlet scalar Higgs field. Breaking ϕ into the two added terms is useful because the origin of $W^\pm$ boson and Z boson masses is apparent when plugging the v term into the EW Lagrangian's Higgs term, and the origin of fermion masses is apparent when plugging the v term into the EW Lagrangian's Yukawa terms.

For example, the Yukawa term for electrons is:

$$\mathcal{L}_{y,e} = f_e \bar{l}_L \phi e_R + f_e \bar{e}_R \tilde{\phi} l_L \tag{2.25}$$

Plugging in the v term of ϕ, one gets:

$$\begin{aligned} \mathcal{L}_{y,e} &\subset \frac{f_e}{\sqrt{2}} \begin{pmatrix} \bar{\nu}_e & \bar{e} \end{pmatrix}_L \cdot \begin{pmatrix} 0 \\ v \end{pmatrix} \cdot e_R + \frac{f_e}{\sqrt{2}} \bar{e}_R \cdot \begin{pmatrix} v & 0 \end{pmatrix} \cdot \begin{pmatrix} \nu_e \\ e \end{pmatrix}_L \\ &= \frac{v f_e}{\sqrt{2}} \left(\bar{e}_L \cdot e_R + \bar{e}_R \cdot e_L \right) \\ &= \frac{v f_e}{\sqrt{2}} (\bar{e} e) \end{aligned} \tag{2.26}$$

which is, in fact, a mass term, leading to an electron mass of $\frac{v f_e}{\sqrt{2}}$. Plugging the h term of ϕ, one gets:

$$\mathcal{L}_{y,e} \subset \frac{f_e}{\sqrt{2}} (h \bar{e} e) \tag{2.27}$$

representing the interaction between the scalar singlet Higgs field, h. The coupling of this interaction is equal to $f_e/\sqrt{2} = m_e/v$.

In other words, the coupling of fermions to the Higgs boson is directly proportional to the fermions' masses, meaning the Higgs boson couples most strongly to top quarks, then to bottom quarks, then to charm quarks, etc. Since top quarks are heavier than the observed mass of the Higgs boson, Higgs decays to top quarks are kinematically forbidden, so the Higgs boson's largest decay branching ratio is actually to bottom quarks, which is the main theoretical motivation behind the work of this thesis to search for the mono-Higgs signature in the channel where the Higgs decays to two bottom quarks.

Chapter 3

DARK MATTER

Early 20$^{\text{th}}$ century observations of the motions of galaxies and stars suggested that gravitational effects produced by matter that is not visible is at play across the universe. These observations led to the concept of "Dark Matter" (DM) - that is, matter that interacts gravitationally, but not electromagnetically.

One such particle has, in fact, been discovered: the neutrino. However, calculations of the neutrino abundance(s) and upper limits on the neutrino mass(es) indicate that neutrinos cannot account for all of (or even a sizable portion of) the Dark Matter in the universe. The existence of the neutrino does establish one very important concept for Dark Matter - Dark Matter need not be explained by the existence of a single new type of particle, but could rather possibly be explained by a whole sector of new particles. Regardless, apart from very specific models and signatures, it is sufficient to consider a single new type of particle as a Dark Matter candidate, and that is what is done here.

This Chapter is organized as follows. Section 3.1 discusses some of the evidence for Dark Matter. Section 3.2 discusses the hypothesis that Dark Matter is comprised of Weakly Interacting Massive Particles. Finally, Section 3.3 outlines how Dark Matter particles might be produced by particle colliders and what signatures they might leave. Additionally, Appendix A discusses the current outlook on Dark Matter models being considered for LHC searches.

3.1 Evidence for Dark Matter

Several observations of the motion of stars within galaxies and the motions of galaxy clusters made in the early 20$^{\text{th}}$ century were inconsistent with Newtonian mechanics but could be explained if there were large sources of gravity that were not visible. Studies of the velocity distributions of stars in nearby galaxies by Jacobus Kapteyn in 1922 [15] and Jan Oort in

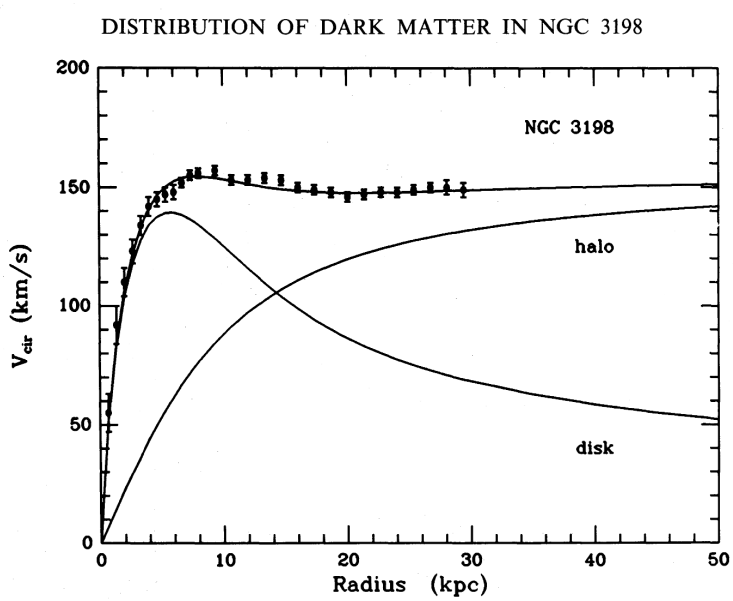

Figure 3.1: The galactic rotation curve of NGC 3198, showing the contributions to the stellar velocity distributions from visible matter ("disk") and from Dark Matter ("halo") [19].

1932 [16] indicated that much more matter must be present in the galaxies than was visible, and observations of the motions of the Coma galaxy cluster by Fritz Zwicky in 1933 [17] also suggested a large contribution to the gravitational forces by objects that were not visible. Later studies of galactic rotation curves (the rotational velocity of stars in a galaxy as a function of their distance from the center of the galaxy) by Vera Rubin and Kent Ford in the 1970's gave further evidence for Dark Matter [18].

The galactic rotation curve of NGC 3198 is shown in Figure 3.1 [19], showing strong evidence for Dark Matter. The rotational velocities of the stars can be inferred from measurements of their redshifts. Accounting for the gravitational forces of all visible stars in the galaxy and applying Newtonian mechanics to calculate this velocity distribution would result in the curve labelled "disk." While this curve does model the data well very close to the galactic center, it does increasingly poorly for stars further from the galactic center. Instead, a model that predicts a halo of Dark Matter around the galaxy fits the data much better.

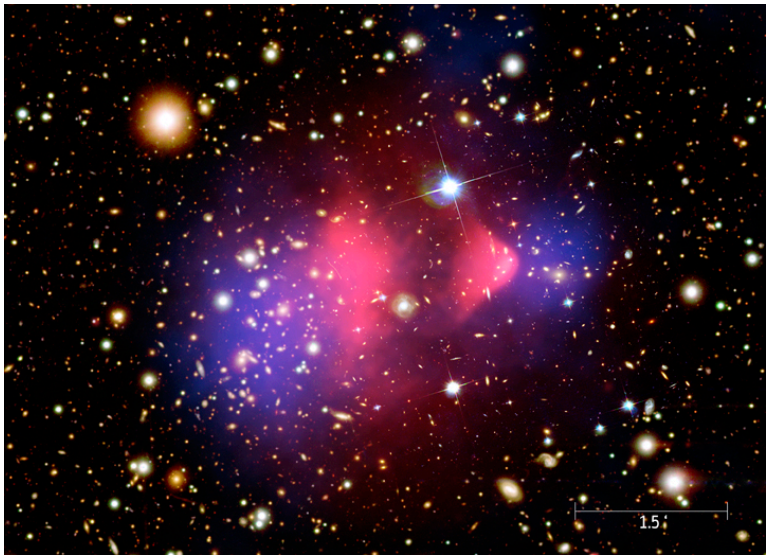

Figure 3.2: An image of the Bullet Cluster, showing two galaxies which have collided. The distribution of baryonic hot gas is highlighted in false-color red while the total distribution of all matter is highlighted in false-color blue [21].

While a model of galaxies that includes a halo of Dark Matter can explain their stellar velocity distributions, it is not the only possible explanation. Other possible models that do not introduce new matter include several modified theories of gravity [20]. However, many of those theories have received little support since the striking observations of the collision of two galaxies, known as the Bullet Cluster, were made [21]. Figure 3.2 shows an image of the Bullet Cluster where the distribution of baryonic hot gas is highlighted in false-color red while the total distribution of all matter, measured using gravitational lensing, is highlighted in false-color blue. The image shows that two galaxies have collided with each other, and while the gaseous matter of the two galaxies interact with each other and slow down, the majority of the matter in the two galaxies pass through each other without interacting. This fits with the assumption that the majority of the matter in the two galaxies is comprised of Dark Matter particles, which may interact gravitationally, but otherwise do not interact significantly with each other or with the baryonic matter.

How much Dark Matter there is in the universe can be inferred from observations of the

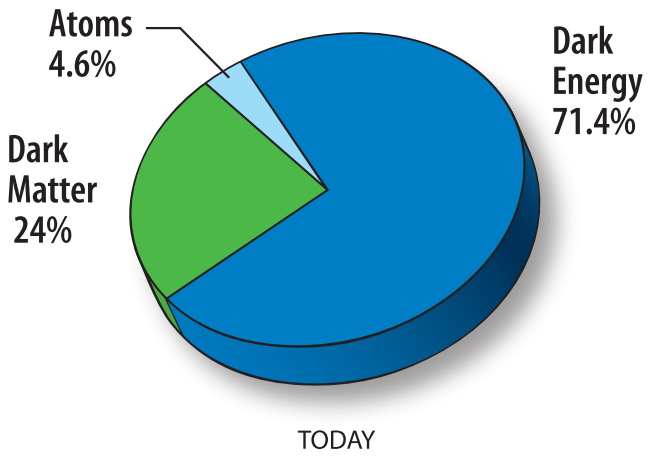

Figure 3.3: Summary breakdown of the composition of the universe, obtained from WMAP observations of the Cosmic Microwave Background [24]

Cosmic Microwave Background. The WMAP [22] and Planck [23] experiments measure the fluctuations of the power spectra of the Cosmic Microwave Background and fit the observed results to the Lamda-CDM model of the universe that contains the parameters Ω_b, Ω_c, and Ω_Λ describing the density of baryonic matter, Dark Matter, and Dark Energy, respectively, in the universe. The results are summarized in the pie chart of Figure 3.3, which shows that roughly a quarter of the universe is comprised of Dark Matter, and only less than 5% of the universe is comprised of the baryonic matter described by the Standard Model. These results make it difficult to overstate the significance of the role of Dark Matter in our understanding of the universe, and motivate the search for the particle nature of Dark Matter as a top priority for physicists today.

3.2 Weakly Interacting Massive Particles and the WIMP Miracle

One of the most attractive and popular theoretical Dark Matter candidates is the Weakly Interacting Massive Particle (WIMP) [25]. There is no precise definition of what would constitute a WIMP, but in general terms, a WIMP would have to be a new fundamental elementary particle with a mass near the weak scale (loosely, from a few $\sim$ GeV to a few

$\sim$ TeV), hence the "massive," and a WIMP would have to interact with Standard Model particles via the gravitational force and possibly either the weak force or a new force with a strength similar to or weaker than that of the weak force. These characteristics of WIMPs are motivated by the desire to explain the abundance of Dark Matter in the universe today.

The amount of Dark Matter that observations indicate exists today could be explained by the thermal freeze out of WIMPs. That is, if WIMPs in the early universe were created by and annihilated to other particles in thermal equilibrium, then as the universe expanded, WIMP annihilation would slow down with the decreasing temperature of the universe, following Boltzmann's Law. This is referred to as the "WIMP miracle" and the abundance of Dark Matter today is sometimes referred to as the "thermal relic abundance," or just "relic abundance."

Measurements from the WMAP experiment predict a relic abundance of $\Omega_c h^2 = 0.1131 \pm 0.0034$ [22], and theoretical derivations of the relic abundance, assuming a single WIMP candidate and assuming the thermal freeze-out model, give the following [12]:

$$\Omega_c h^2 \simeq \frac{0.1 \text{ pb} \cdot c}{\langle \sigma_A v \rangle} \tag{3.1}$$

where h is here the Hubble constant that parameterizes the expansion of the universe, c is the speed of light, σ_A is the WIMP annihilation cross section, v is the relative velocity of the annihilating WIMPs, and $\langle \dots \rangle$ indicates thermal averaging. Applying the measured value of $\Omega_c h^2$ gives an approximation for the WIMP annihilation cross section of $\langle \sigma_A v \rangle \simeq 3 \times 10^{-26}$ cm^3 s^{-1}, which is at the weak-scale.

Throughout the rest of this thesis, Dark Matter is assumed to be composed of WIMPs, and the two terms are used interchangeably. The character used to indicate a WIMP is typically chosen to be "χ," and this character is frequently used here in diagrams and plots.

3.3 Searching for Dark Matter at Colliders: Mono-X

In order to detect DM outside of gravitational observations, it must be assumed that DM and SM particles interact via a new force. Figure 3.4 shows how DM particles might interact with SM particles, where what is filled in for the "blob" depends on the specific model postulated.

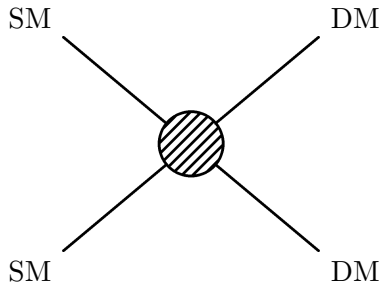

Figure 3.4: A pseudo-Feynman diagram illustrating how SM particles and DM particles might interact.

Without specifying any additional details, it is already possible to discuss the basic principles of searching for DM if one treats Figure 3.4 as a pseudo-Feynman diagram. For example, if time is taken as moving from the left to the right, the diagram will represent two SM particles annihilating to produce two DM particles - a process one can imagine taking place at a particle collider. As such, searches for this particular process are known as "collider searches," which is the main topic of this thesis. However, if time is taken as moving from the right to the left, the diagram will represent two DM particles annihilating to produce two SM particles. This kind of process is most likely to occur in parts of the universe where DM is densest. As such, searches for this process are typically carried out by astrophysics experiments, and are referred to as "indirect detection searches" [26]. Finally, taking time as moving from top to bottom (or bottom to top), the diagram represents a DM particle scattering off of a SM particle. Searches for this type of interaction are not unlike searches for neutrinos that scatter off atomic nuclei, and such searches for DM are referred to as "direct detection searches" [27]. The rest of this thesis will focus on "collider searches."

While Figure 3.4 provides a natural mechanism for the production of DM at particle colliders, it does not provide any mechanism for the detection of DM by particle collider experiments. The detectors employed by particle collider experiments have been fine-tuned to detect charged particles, electromagnetic showers, and hadronic showers, but not DM (or even neutrinos). However, if DM at particle colliders is produced in association with

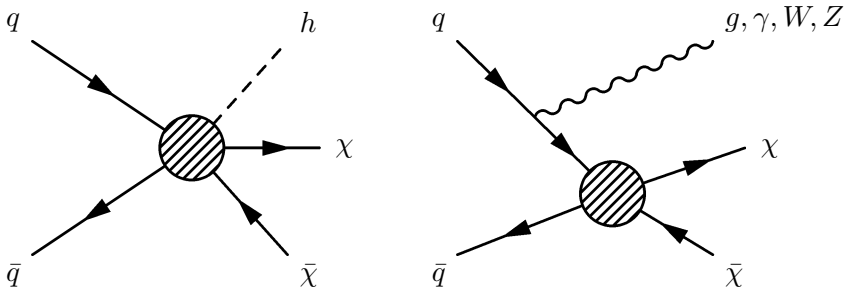

Figure 3.5: Examples of DM processes which could theoretically be produced and detected at particle colliders.

a SM particle, for example a particle produced as initial state radiation (ISR), then it is possible to search for the single SM particle, and infer the production of DM particles via an imbalance in the energy deposited in the detector. This is the basis of the concept of "missing transverse momentum" (or "missing transverse energy" as it is typically referred to in ATLAS) in the detector and will be elaborated on in Chapter 7. Figure 3.5 shows how DM particles might be produced in association with a gluon, a photon, a W or Z boson, or a Higgs boson. This general process, commonly referred to as "mono-X," offers a wealth of signatures to probe with collider experiments.

In the following sections, several mono-X signatures and models will be discussed, followed by an in-depth look at the specific model employed by the mono-Higgs search central to this thesis.

Much of the work on developing robust methods of interpreting LHC results with DM models was carried out by the LHC DM Forum [3]. The author of this thesis contributed to this body of work with recommendations and interpretation studies for several DM models. Much of what follows is a summary of the work of the LHC DM Forum.

3.3.1 EFT Models and their Validity

The subject of Effective Field Theory (EFT) validity was recognized as a serious issue by the end of LHC Run 1. This Section describes why, though for a more in-depth treatment, see Reference [28].

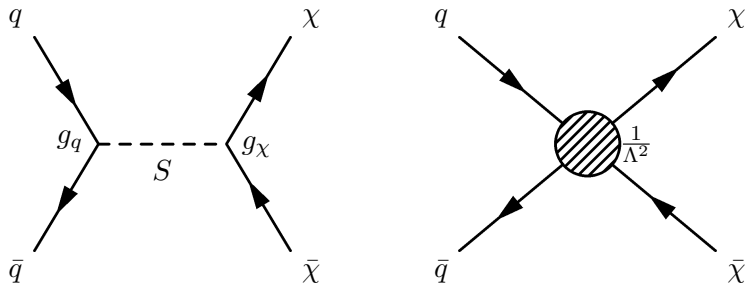

Figure 3.6: An s-channel Feynman diagram illustrating an interaction between quarks and DM particles via a scalar mediator, S, on the left, and the corresponding EFT contact operator interaction on the right.

EFTs are simplifications of complete Quantum Field Theories where the mass of the force mediator is large enough with respect to the momentum transfer of a physical process that mediator exchange can be replaced by a contact operator. The basic idea of an EFT is illustrated with a specific example in Figure 3.6. The model considered in Figure 3.6 introduces a new scalar mediator, S, which couples to both quarks and DM according to the following Lagrangian:

$$\mathcal{L}_S \supset \frac{1}{2}M^2S^2 - g_q q\bar{q}S - g_\chi \chi\bar{\chi}S \tag{3.2}$$

where M is the mass of S, g_χ is the coupling strength of S to DM, and g_q is the coupling strength of S to quarks.

The tree-level s-channel Feynman diagram of Figure 3.6 can be replaced with the more simple contact operator diagram of Figure 3.6, given that the momentum transfer of the interaction is much smaller than the mass of the scalar mediator.

Mathematically, this can be seen by expanding the S propagator term in powers of $\frac{Q_{\text{tr}}}{M}$:

$$\frac{1}{Q_{\text{tr}}^2 - M^2} = -\frac{1}{M^2}\left(1 + \frac{Q_{\text{tr}}^2}{M^2} + \mathcal{O}\left(\frac{Q_{\text{tr}}^4}{M^4}\right)\right) \tag{3.3}$$

where Q_{tr} is the momentum transfer of the process.

If $Q_{\text{tr}} \ll M$, the propagator term can be simplified to just:

$$\lim_{Q_{\text{tr}} \ll M} \frac{1}{Q_{\text{tr}}^2 - M^2} = -\frac{1}{M^2} \tag{3.4}$$

Multiplying the propagator term by the vertex factors g_q and g_χ, a new effective vertex factor can be constructed:

$$\frac{1}{\Lambda^2} = \frac{g_q g_\chi}{M^2} \tag{3.5}$$

where Λ is referred to as the mass scale of the EFT. The contact operator representing the interaction between DM and quarks can thus be constructed with this new effective vertex factor:

$$\mathcal{O}_s = \frac{1}{\Lambda^2}\chi\bar{\chi}q\bar{q} \tag{3.6}$$

This is the mathematical formulation which is represented by the contact interaction shown in Figure 3.6. As mentioned, this formulation is only valid when the momentum transfer, Q_{tr}, is much smaller than the mass of S. Using the relation between the mass of S and the effective vertex factor defined in Equation 3.5, a constraint on the mass scale Λ can be derived:

$$Q_{\text{tr}} \ll M \rightarrow Q_{\text{tr}} \ll \Lambda\sqrt{g_q g_\chi} \rightarrow \Lambda \gg \frac{Q_{\text{tr}}}{\sqrt{g_q g_\chi}} \tag{3.7}$$

Unitarity constraints require that both g_q and g_χ be less than 4π, so the maximum value of $\sqrt{g_q g_\chi}$ is 4π. For a tree-level s-channel process, such as the one portrayed in Figure 3.6, kinematic constraints require that $Q_{\text{tr}} \geq 2m_\chi$. Assuming a minimum Q_{tr} of $\sim 2m_\chi$ and applying these assumptions and constraints to the condition on Λ presented in Equation 3.7, the following, more concrete, condition on Λ can be constructed:

$$\Lambda > \frac{2m_\chi}{4\pi} \tag{3.8}$$

Variations of this condition on Λ were employed by several LHC Run 1 ATLAS searches for DM. Note that the condition on Λ presented in Equation 3.8 is a loose condition for a few reasons: it drops the $\gg$ in favor of an easier to manage $>$ requirement, it assumes the minimum momentum transfer, $Q_{\text{tr}} = 2m_\chi$, and it assumes maximal g_q and g_χ couplings. Note also that formulating this concrete constraint on Λ required that a specific underlying ultra-violate (UV) complete process be constructed. Thus, the condition is only valid under very narrow interpretation, and since a UV-complete process must be constructed to derive this constraint on Λ, the UV-complete process itself might as well be used in lieu of an

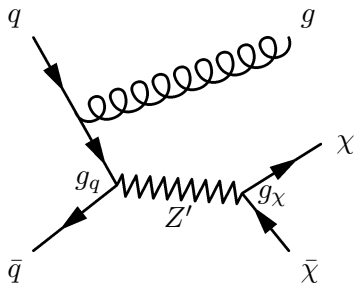

Figure 3.7: The Z' mono-jet simplified model.

EFT operator to begin with. These realizations are what led to the LHC DM community to greatly favor simplified models over EFT models.

3.3.2 Simplified Models

Simplified models specify the mediator which couples to SM particles and to DM, but are not complete theoretical models. Often, simplified models are implementations of a single or a small number of tree-level Feynman diagrams that describe a signal process of interest.

An example of a simplified model is shown in the Feynman diagram of Figure 3.7. This simplified model introduces a new vector boson mediator, Z' (with mass $m_{Z'}$), that couples to quarks with a coupling constant of g_q and to DM (with mass m_χ) with a coupling constant of g_χ (sometimes written as g_{DM}). Z' can also have a coupling to leptons, g_l, but for DM searches, this coupling is typically assumed to be 0 or negligibly small.[4] In the diagram of Figure 3.7, a gluon is radiated as initial state radiation, resulting in a mono-jet signature, as gluons produce physics objects known as "jets" (discussed in greater detail in Chapter 7). However, the initial state radiation could just as well be a photon, W boson, or Z boson, resulting in mono-photon, mono-W, or mono-Z signatures.

Note that while this same mechanism could describe a mono-Higgs signature, it is heavily suppressed by the small Yukawa coupling of the Higgs boson to light quarks. A slightly different approach is necessary to construct a model that produces a mono-Higgs signature, and the approach used by the search presented in this thesis is described in Section 3.3.3.

[4] when g_l is 0, Z' is said to be "leptophobic"

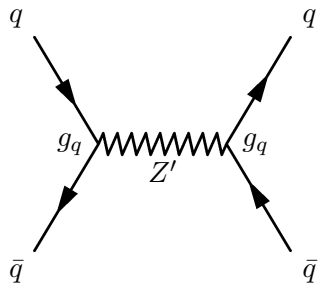

Figure 3.8: A Z' resonance dijet process.

Work on models that can describe both mono-Higgs signatures and other mono-X signatures are presented in Appendix A, and such models will likely become the standard for the interpretation of future collider DM searches.

Also note that since the newly introduced Z' particle couples to quarks, it can also decay to quarks. This process is shown in Figure 3.8 and results in a resonant dijet signature that can be searched for [29]. Whether it is more powerful to search for this model in a mono-X channel or the dijet channel will depend on the couplings g_q and g_χ (and to a lesser extent, on the masses $m_{Z'}$ and m_χ). Intuitively, if g_q is tuned down and g_χ is tuned up, the mono-X channels could become dominant over the dijet channel.

Figures 3.9 and 3.10 show experimental exclusion limits on this Z' DM model as a function of $m_{Z'}$ and m_χ for two different sets of choices of coupling parameters. In Figures 3.9, g_χ is set to 1 and g_q is set to 0.25. In Figures 3.10, g_χ is set to 1 and g_q is set to 0.1. In the case that g_q is set to 0.25, the exclusion limits are dominated by the dijet channel, while when g_q is set to 0.1 the mono-X (labelled in the Figures as $E_{\mathrm{T}}^{\mathrm{Miss}} + X$) exclusion limits carve out a unique region of phase-space. This is a demonstration of how the dijet and mono-X searches are complimentary in the regions of phase-space they are sensitive to for different models, and this guides the choices of model parameters to pick when formulating a mono-X search.

These Z' DM model limits can also be converted to cross section limits as a function of DM mass and then directly compared to the limits set by direct detection experiments. An example of this is shown in Figure 3.11 for $g_\chi = 1$ and $g_q = 0.25$. The figure demonstrates the

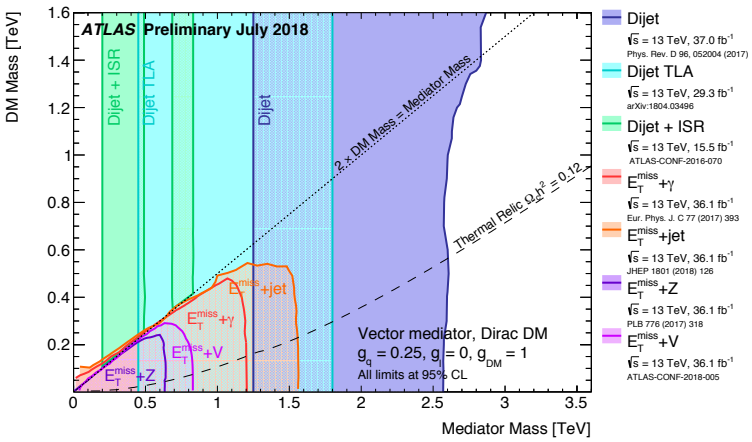

Figure 3.9: Limits on the Z' DM model as a function of $m_{Z'}$ and m_χ for $g_\chi = 1$ and $g_q = 0.25$. With these couplings, the dijet resonance search is the dominant discovery channel over all regions of parameter space [30].

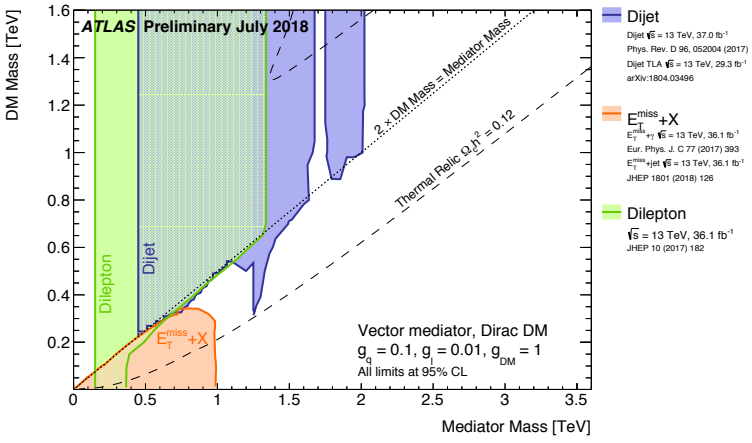

Figure 3.10: Limits on the Z' DM model as a function of $m_{Z'}$ and m_χ for $g_\chi = 1$ and $g_q = 0.1$. With these couplings, mono-X searches are the dominant discovery channel over some regions of parameter space [30].

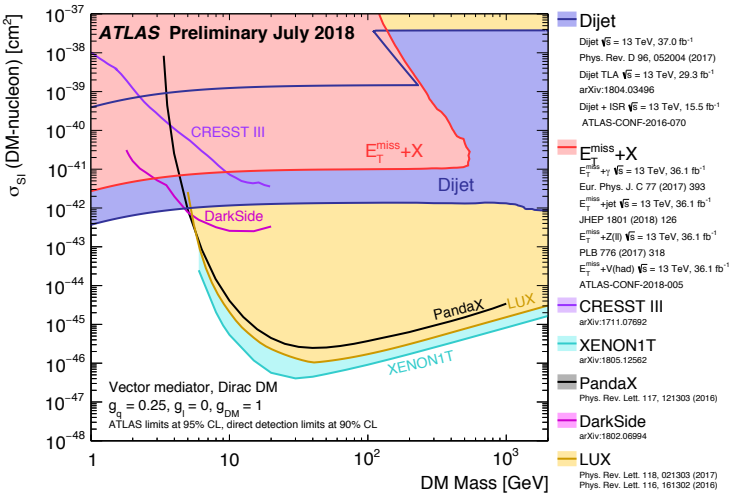

Figure 3.11: Limits on the DM-nucleon scattering cross section from leading direct detection experiments and from both ATLAS dijet and mono-X searches [30].

complimentarity of direct detection experiments and collider searches for DM, as the direct detection experiments offer the most competitive limits for DM masses above $\sim$ 5 GeV, with XENON1T currently the most competitive [31], while collider searches offer the most competitive limits for DM masses below $\sim$ 5 GeV. However, some DM models which can be searched for at colliders cannot be probed at all with direct detection experiments, and vice versa, as will be seen in Section 3.3.3.

While the Z' DM simplified model described thus far can illustrate many of the key points of DM searches at colliders, it is by no means the only simplified model considered. Indeed, scalar DM models, such as the one alluded to in Figure 3.6, are also considered. A mono-jet signature could be described, for example, by the scalar DM simplified model portrayed in Figure 3.12.

Since the Higgs boson is unlikely to be radiated as ISR, a different approach is necessary to construct simplified models in which a mono-Higgs channel could be the dominant discovery channel. One such approach, and the one considered for the DM search of this thesis, is described in Section 3.3.3.

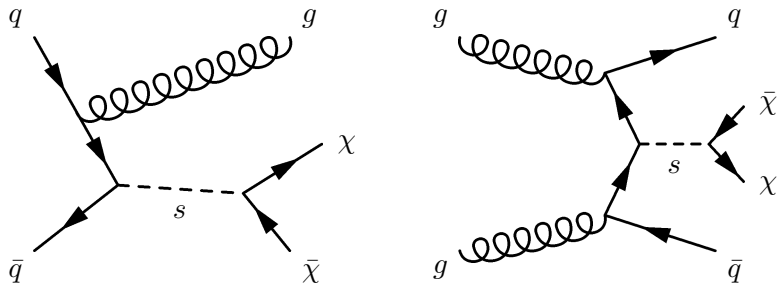

Figure 3.12: A scalar mono-jet simplified model.

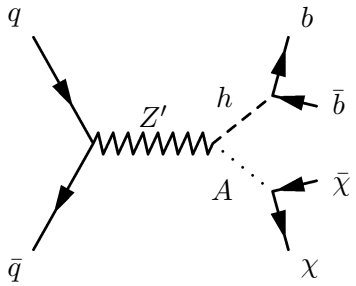

Figure 3.13: The mono-Higgs process using a $Z'-$2HDM simplified model.

3.3.3 The $Z'-$2HDM Model for Mono-Higgs

The $Z'-$2HDM model introduces a new vector boson, Z', to a Type-II two-Higgs-doublet model (2HDM), which introduces, among other particles, a new pseudo-scalar particle A. The full mono-Higgs process described by this model is shown in the Feynman diagram of Figure 3.13. A new vector boson, Z', is produced that decays to a SM Higgs, h, and a new pseudo-scalar Higgs, A. The SM Higgs then decays to a pair of b-quarks while the pseudo-scalar Higgs decays to a pair of DM particles.

In the 2HDM, there are two Higgs doublets, Φ_2 and Φ_1. Which fields the two doublets couple to determines the type of the 2HDM. In the Type-II 2HDM considered here, Φ_2 couples to up-type quarks and Φ_1 couples to down-type quarks and leptons. As such, it makes notation easier to follow to define $\Phi_u = \Phi_2$ and $\Phi_d = \Phi_1$. The couplings of the Higgs doublets to quarks and leptons can thus be described by the following Lagrangian:

$$\mathcal{L} \supset y_u Q \tilde{\Phi}_u \bar{u} + y_d Q \Phi_d \bar{d} + y_e L \Phi_d \bar{e} \tag{3.9}$$

Then, after electroweak symmetry breaking, the two Higgs doublets attain vacuum expectation values v_u and v_d and can be parameterized as follows:

$$\Phi_u = \frac{1}{\sqrt{2}} \begin{pmatrix} \cos(\beta) \cdot H^+ \\ v_u + \cos(\alpha) \cdot h + \sin(\alpha) \cdot H + i \cos(\beta) \cdot A \end{pmatrix} \tag{3.10}$$

$$\Phi_d = \frac{1}{\sqrt{2}} \begin{pmatrix} -\sin(\beta) \cdot H^+ \\ v_d - \sin(\alpha) \cdot h + \cos(\alpha) \cdot H - i \sin(\beta) \cdot A \end{pmatrix} \tag{3.11}$$

where parameter β is related to the vacuum expectation values via:

$$\tan(\beta) \equiv \frac{v_u}{v_d} \tag{3.12}$$

This parameterization reveals five Higgs fields: h and H are neutral scalars, $H^\pm$ are charged scalars, and A is a pseudo-scalar. h and H mix via mixing angle α. In this analysis, it is assumed that h corresponds to the SM Higgs particle whose existence has been confirmed. This assumption then puts the constraint on α that $\alpha = \beta - \pi/2$ and is known as the "alignment limit." Perturbativity requirements on the t-quark Yukawa coupling constrains $\tan(\beta) \geq 0.3$. The remaining parameters of this 2HDM are the masses of H, $H^\pm$, and A. In this analysis, the masses of H, H^+, and H^- are assumed to be always equal to 300 GeV, while the mass of A is allowed to vary. These constraints and assumptions effectively reduce the free parameters of the 2HDM to $\tan(\beta)$ and m_A. While scans on both of these parameters were done in the past, this analysis fixes $\tan(\beta) = 1$ and only considers scans on m_A. This is because previous studies have shown that the kinematic signature of this mono-Higgs process does not depend heavily on $\tan(\beta)$, while variations of m_A can lead to unique kinematic signatures [6].

On top of this 2HDM is introduced a new vector boson, Z' with mass $m_{Z'}$, and a fermionic DM particle, χ with mass m_χ. The Z' particle couples to quarks with coupling strength $g_{Z'}$ and to Ah with coupling strength $g_{Z'} \cdot \sin(\beta) \cdot \cos(\beta)$. The coupling parameter $g_{Z'}$ is set to 0.8 in this analysis. While the previous discussion of dijet versus mono-X searches in Section 3.3.2 would suggest that $g_{Z'}$ be set to 0.1, the value 0.8 was chosen in order to more directly compare the results of this mono-Higgs search to those of the most recent previous analysis iteration [8].

Table 3.1: Summary of $Z'-$2HDM parameters.

Parameter	Constraints	Kinematic Dependence	Chosen Value	Brief Description
m_h	SM Higgs	—	125 GeV	mass of h
m_A	—	yes	300 GeV : 800 GeV	mass of A
m_H	—	—	= 300 GeV	mass of H
$m_{H^\pm}$	—	—	= 300 GeV	mass of $H^\pm$
$\tan(\beta)$	≥ 0.3	minimal	1	v_u/v_d
α	$\beta - \pi/2$	—	$\beta - \pi/2$	h-H mixing
m_χ	—	minimal if $< m_A/2$	100 GeV	mass of χ
$m_{Z'}$	—	yes	600 GeV : 3000 GeV	mass of Z'
$g_{Z'}$	$< 4\pi$	no	0.8	Z'-q coupling

It is assumed that A decays to a $\chi\bar{\chi}$ pair with $\mathcal{BR}(A \to \chi\bar{\chi}) = 100\%$. It has been shown previously that the kinematic dependence of this mono-Higgs signature does not depend significantly on m_χ as long as A is produced on-shell - that is, as long as $m_A > 2m_\chi$. As such, m_χ was chosen to be 100 GeV in this analysis and m_A was scanned from 300 GeV to higher masses, and the results of this analysis are valid for any $m_\chi \leq 100$ GeV.

A summary of all $Z'-$2HDM parameters and their values used in this analysis is shown in Table 3.1. The free parameters chosen for parameter scans are m_A and $m_{Z'}$ - tuning these masses can give a wide range of kinematic signatures useful for defining multiple analysis regions. The kinematic signatures of the model as a function of these masses are detailed further in Section 5.2.2 and Appendix D.

It should be noted that, due to its nature, the $Z'-$2HDM DM model cannot be probed by today's direct detection experiments. This can be seen by reading the Feynman diagram of Figure 3.13 with the time-axis going "up" - a quark and DM particle scatter, producing, in the collision, a Higgs boson. This process would be too suppressed to search for in direct detection experiments unless the energy of the incoming DM particle were much greater than the mass of the Higgs boson.

The process could, in theory, be probed by indirect detection searches if m_A is greater than $m_{Z'} + m_h$. However, if m_A is greater than $m_{Z'} + m_h$, then the collider search channel would become suppressed. Thus, for the case of this model, collider searches and indirect detection searches could give complimentary results.

Chapter 4

THE LARGE HADRON COLLIDER AND THE ATLAS EXPERIMENT

The Large Hadron Collider [32] [33] (LHC) is the world's most advanced and highest energy particle collider. It is a circular collider capable of colliding protons at a center-of-mass energy of $\sqrt{s} = 14$ TeV every 25 ns with an instantaneous luminosity of $2 \times 10^{34}\text{cm}^{-2}\ \text{s}^{-1}$, although it is currently operating at $\sqrt{s} = 13$ TeV. ATLAS [34] (A Toroidal LHC ApparatuS) is one of two general purpose particle detectors built around collision points of the LHC. The ATLAS detector is comprised of several sub-detectors, each optimized for the detection of specific particles or particle properties. Reading out the vast amount of data from all sub-detectors every 25 ns is an incredible technical challenge, and is expected to become an even greater challenge in 2025 when the LHC is upgraded to provide an even higher instantaneous luminosity.

This chapter is organized as follows. The LHC will be introduced in Section 4.1 and the ATLAS detector and its sub-detectors will be introduced in Section 4.2, with special attention given to the Pixel detector which has been crucial for the b-hadron identification critical to the work of this thesis. Finally, the ATLAS trigger and data acquisition system will be discussed in Section 4.3, again with special attention given to the Pixel detector.

4.1 The Larger Hadron Collider (LHC)

The LHC was built and is operated by the European Organization for Nuclear Research (CERN). It is the largest and highest energy particle accelerater in the world, with a circumference of roughly 27 km and located roughly 1 km underneath the Earth's surface near Geneva, Switzerland. The LHC can deliver proton-proton, proton-heavy ion, or heavy ion-heavy ion collisions at its four collision points. At these four collision points are seven detectors which record data from the collisions to analyze. The two biggest detectors, ATLAS [34] and CMS [35], are general purpose particle detectors designed to measure and

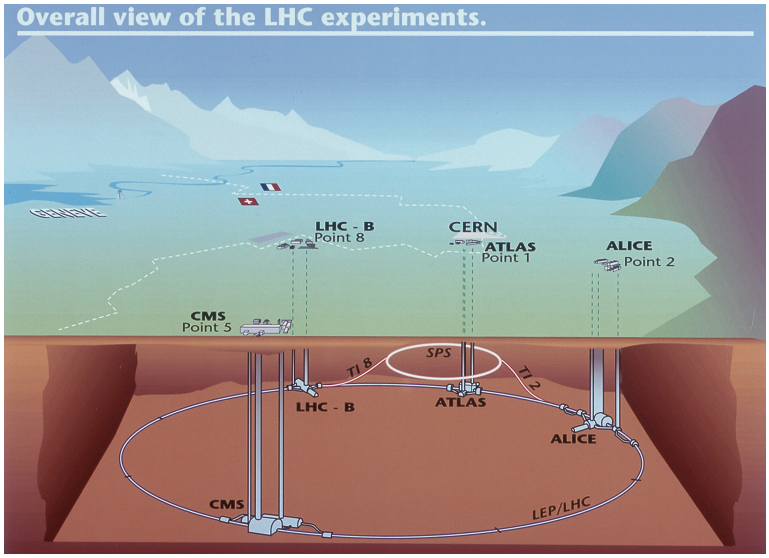

Figure 4.1: An illustration of the LHC showing the four interaction points and four of the seven detectors located around the LHC main ring [41].

search for diverse particle physics processes. The other 5 detectors, ALICE [36], LHCb [37], TOTEM [38], LHCf [39], and MoEDAL [40], are much more specialized, searching for specific physics processes to address specific problems in physics today. An illustration of the LHC is shown in Figure 4.1.

The LHC went online for the first time in 2010, and went offline from 2013 to 2015 for a two year upgrade period. The period f from 2010 to 2013 is referred to as "Run 1," and the period since 2015 until the end of 2018 is referred to as "Run 2." The term "Run" is also used to denote a roughly 24 hr period of time during which protons or heavy ions are circulating in the LHC main ring. To differentiate between these daily Runs and the long Run periods of the LHC, this thesis will refer to the latter as "LHC Run 1," "LHC Run 2," etc, and the former simply as "Run 277892," etc.

The protons used in LHC collisions begin as the nuclei of Hydrogen atoms in a bottle of Hydrogen gas. This gas is fed into a duoplasmatron where it is ionized and the protons are accelerated into a beam by an electric field to an energy of 94 KeV and ejected through an

aperture [42].[5] This 94 KeV proton beam is then fed into the LINAC 2, a linear particle accelerator which accelerates the beam to an energy of 50 MeV via oscillating electric fields. This 50 MeV proton beam is then fed into a series of synchrotron accelerators - first into the Proton Synchrotron Booster, where it is accelerated to 1.4 GeV, then to the Proton Synchrotron, where it is accelerated to 25 GeV, then to the Super Proton Synchrotron, where it is accelerated to 450 GeV, and finally to the LHC main ring, where, during LHC Run 2, it is accelerated to 6.5 TeV.

These synchrotrons utilize radio frequency cavities to accelerate the proton beam, dipole magnets to bend the proton beam along the circulate beam pipes, and quadrupole magnets to focus the proton beam. The LHC main ring has installed over 1000 superconducting dipole magnets, which operate at 7.7 TeV when the proton beam energy is 6.5 TeV, and nearly 400 superconducting quadrupole magnets, which focus the proton beam into nearly 3000 bunches separated 25 ns apart. Each bunch contains approximately 100 billion protons.

It is when the beam is being fed into the LHC main ring that it is split into two oppositely rotating beams. There are four points where the beams are able to cross to produce collisions, referred to as Point 1, Point 2, Point 5, and Point 8. Whether the beams collide or not is controlled by special magnets at the crossing points. ATLAS is situated at Point 1, ALICE at Point 2, CMS at Point 5, and LHCb at Point 8. When enough protons, or heavy ions, have been lost during a Run, they are dumped at Point 6, that is, special magnets direct them towards a target outside of the LHC main ring where they are lost.

4.1.1 Luminosity

The total number of expected events of a particular physical process is determined by the following equation:

$$N = \mathcal{L}\sigma \tag{4.1}$$

where $\mathcal{L}$ is the total integrated luminosity of data collected and σ is the cross section of the physical process. The cross sections for different processes in LHC proton-proton collisions

[5] this process is not unlike the way in which electron beams are created by Cathode Ray Tubes - a technology which dominated televisions for over half a century

is proportional to the sum of the squares of matrix elements of Feynman diagrams times the Parton Distribution Functions (PDFs) of the partons from each proton which collide. The total integrated luminosity of the data collected is the integral over time of the instantaneous luminosity provided by the collider, theoretically given by the following equation:

$$L = \frac{N_b^2 n_b f_r \gamma_r 4\pi\epsilon_n \beta^*}{F} \tag{4.2}$$

Here, N_b is the number of protons per bunch, n_b is the number of filled bunches per beam, f_r is the frequency that the beams travel around the main LHC ring, γ_r is the relativistic gamma factor of the protons, ϵ_n is the normalized transverse beam emittance, β^* is a measure of the beam width in the longitudinal direction, and F is a geometric factor which accounts for the non-zero crossing angle of the two proton beams. While these values can typically all be individually calculated and measured to determine the instantaneous luminosity, ATLAS instead has a series of dedicated detectors used to measure the instantaneous luminosity [43].

4.1.2 Pile-Up

When bunches of protons cross each other at the interaction points of the LHC, a single collision typically does not occur - rather, several partons from several protons in each bunch collide. The most energetic collision is typically referred to as the "hard-scatter" event, while other collisions are referred to as "pile-up" events. The hard-scatter event is typically the event of interest, and the particles resulting from pile-up events can contaminate the hard-scatter event, providing challenges to its reconstruction. In the LHC Run 2, the average number of pile-up events, $\langle\mu\rangle$, is around 30. These events can occur anywhere within the beam-spot.[6] The larger the luminosity, the larger the number of pile-up events. In order to maximize the amount of events which can be produced by the LHC, and data which can be recorded by LHC experiments, pile-up suppression algorithms and techniques are critical.

A powerful way to suppress the contamination from pile-up events is to use tracking detectors with high enough resolution to reconstruct individual interaction vertices. Then,

[6] the beam-spot is the area where the two LHC beams cross and collide

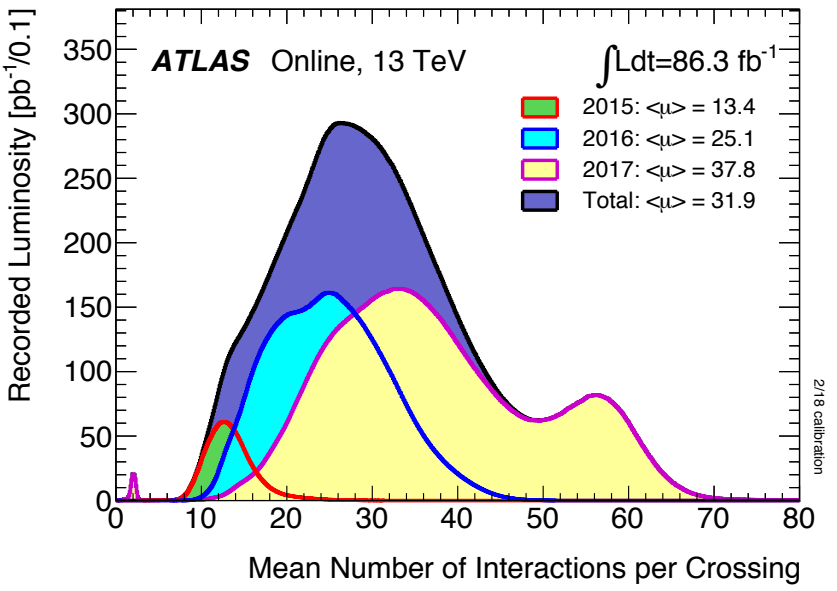

Figure 4.2: The average pile-up distribution for the 2015, 2016, and 2017 ATLAS data taking periods [44].

the primary vertex, being the vertex associated with the hard-scatter event, can be reconstructed, and tracks which are not consistent with having originated from the primary vertex can be vetoed. Other techniques for pile-up suppression based on calorimeter information have also been extensively explored by LHC experiments, and 1 such technique, known as jet-trimming, will be discussed in further detail in Section 7.5.3.

The average pile-up distributions, broken down into 2015, 2016, and 2017 ATLAS data taking periods, is shown in Figure 4.2.

4.2 The ATLAS Detector

An illustration of the ATLAS detector is shown in Figure 4.3. It is constructed to be geometrically cylindrical around the LHC beam axis and is approximately 25 meters in diameter, 44 meters long, and weighs 7000 tons. Proton-proton or heavy ion collisions from the two LHC beams occur at the center of the detector and the resulting particles fly outwards in any direction. ATLAS is comprised of several sub-detectors, each of which

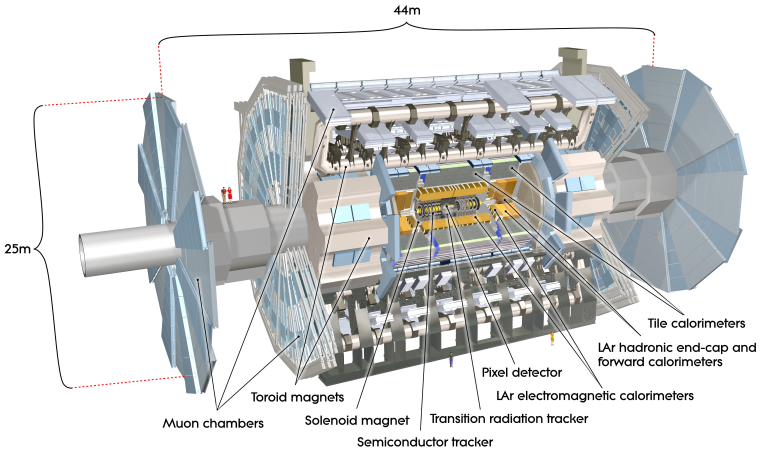

Figure 4.3: A rendering of the ATLAS detector with ATLAS sub-detectors labelled [46].

specializes in measuring kinematic properties of the different types of outgoing particles.

The University of Washington has made many contributions to the design and construction of the current ATLAS detector [45]. Members of the University of Washington ATLAS group designed and developed the manufacturing specification of drift tubes for the ATLAS Forward Muon Chamber, and 1/3 of the tubes were produced at the University of Washington, mounted to the muon chambers, and shipped to CERN. The University of Washington group also was responsible for the design and construction of the Insertable B-Layer (IBL) Support Tube, IBL Precision Tube, the development of firmware and software for the IBL data acquisition system, and the commissioning and operation of the IBL.

ATLAS uses a right-handed coordinate system with the z-axis, or longitudinal axis, parallel to the beam axis, the x-axis pointing towards the center of the LHC, and the y-axis pointing towards the Earth's surface. An azimuthal angle, ϕ, is defined to rotate around the z-axis, and polar angle θ to rotate around the x-axis.

Instead of θ, polar angle measurements are often made using pseudo-rapidity, η, which is defined by Equation 4.3.

$$\eta \equiv -\ln\left(\tan\frac{\theta}{2}\right) \tag{4.3}$$

Differences in η are Lorentz-invariant quantities for massless particles, where a particle's

pseudo-rapidity is equal to its rapidity, y. Since most heavy particles decay into lighter particles promptly, the particles which pass through the ATLAS sub-detectors are usually light leptons, photons, and hadrons, all of which are typically light enough compared to their energies to be treated as massless, and thus pseudo-rapidity is approximately Lorentz-invariant for all particles detected by ATLAS.

Angular distances between particles are typically given by $\Delta\phi$ for a transverse angular distance and $\Delta R = \sqrt{\Delta\phi^2 + \Delta\eta^2}$ for an approximately Lorentz-invariant total angular distance.

Since collisions in ATLAS occur approximately head-on along the z direction, the momenta of the outgoing particles in the $x - y$, or transverse, direction should sum to zero. However, the longitudinal momenta of colliding particles is not necessarily the same. For this reason, the most useful measure of a particle's momentum is its transverse momentum, p_{T}.

Thus, the measurements most often used by ATLAS to fully specify the 4-momenta of particles are p_{T}, η, ϕ, and m (which is assumed to be 0 for the final state, detected particles). These quantities can of course be transformed to give the 4-momenta of particles in the form (E, p_x, p_y, p_z) as well.

The ATLAS detector has three main sets of sub-detectors: the Inner Detector (ID) which measures the trajectory of charged particles, the electromagnetic and hadronic calorimeters, which together measure the energy depositions of primarily electrons, photons, and hadrons, and the Muon Spectrometer (MS) which measures the trajectory of muons. The ID is situated closest to the beam pipe, and the MS is situated the farthest from the beam pipe, with the calorimeters in the middle.

The three sets of sub-detectors are constructed using two main geometries - cylindrical barrel geometries are used for detectors located at central η values, and wheel-shaped end-cap geometries are used for detectors located at forward η values. The basic working principles of each sub-detector are described in the following sections.

4.2.1 The Inner Detector

The ATLAS Inner Detector (ID) is responsible for reconstructing the trajectories of charged particles and is the ATLAS sub-detector system closest to the LHC beam-line. The sensor elements of the ID are designed to record signals as charged particles pass through them, while also minimizing the energy loss of the particles. All sensors in the ID sit in a 2 T magnetic field parallel to the beam-line that is produced by a super-conducting solenoid positioned between the ID and the ATLAS electromagnetic calorimeter. The magnetic field bends the trajectories of charged particles, and reconstructing the curvature of the particle trajectories allows for measurements of the particles' transverse momenta.

A rendering of the ID is shown in Figure 4.4. The ID consists of Pixel, silicon strip Semiconductor Tracker (SCT), and Transition Radiation Tracker (TRT) sub-detectors. The Pixel system [47] consists of four barrel layers and three end-cap layers on each end, with the layer closest to the beam-line, the Insertable B-Layer (IBL) [48], being only 3.3 cm from the beam-line. The Pixel system provides a coverage of $|\eta| < 2.5$. The SCT system [49] consists of four barrel double layers and 18 end-cap layers (9 on each end), and provides a coverage of $|\eta| < 2.5$. The TRT [50] consists of 70 barrel layers and 280 end-cap layers (140 on each end), and provides a coverage of $|\eta| < 2.0$.

The Pixel system provides the highest spatial resolution for hit reconstruction, due to the fine granularity of the pixel sensors, which have a pitch of $50\,\mu\text{m} \times 250\,\mu\text{m}$ oriented in $\Delta\phi \times \Delta\eta$ in the IBL and $50\,\mu\text{m} \times 400\,\mu\text{m}$ oriented in $\Delta\phi \times \Delta\eta$ in the other three Pixel detector layers. These fine granularity sensors, which cover the full range of ϕ and a range of η of $|\eta| < 2.5$, require more than 90 million read-out channels. The outer three Pixel detector barrel layers provide an intrinsic spatial resolution for hits of $14\,\mu\text{m}$ in the $r\phi$ plane, and $115\,\mu\text{m}$ in the z-direction, while the IBL provides an intrinsic spatial resolution for hits of $14\,\mu\text{m}$ in the $r\phi$ plane, and $72\,\mu\text{m}$ in the z-direction. Algorithms taking advantage of charge deposition information are able to further increase these intrinsic resolutions. This high resolution is critical for reconstructing pile-up and secondary vertices. The ability to reliably match tracks with pile-up vertices is essential for reducing contamination of hard-scatter processes due to pile-up events, and the ability to reconstruct and associate tracks

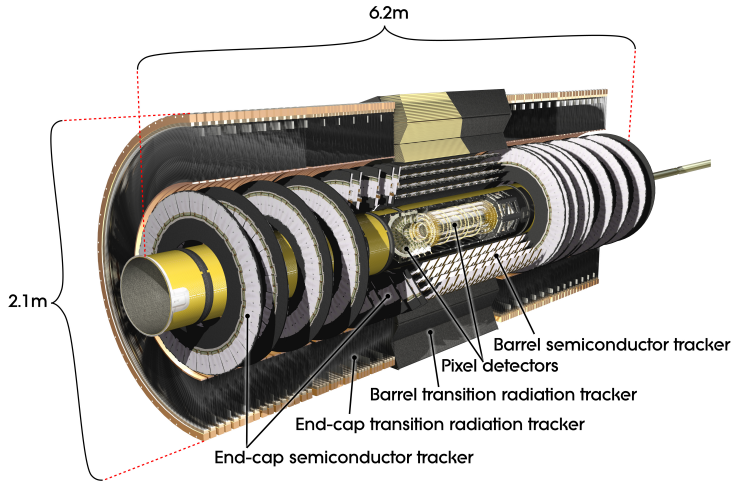

Figure 4.4: A rendering of the ATLAS inner tracker, showing the Pixel, SCT, and TRT sub-detectors [51].

to secondary vertices is essential to tagging algorithms of non-prompt decays, such as the decays of b-hadrons which are important for the main physics analysis of this thesis.

The high resolution of the Pixel detector would not be possible without its inner-most layer, the IBL. The IBL is a new Pixel detector layer installed between LHC Runs 1 and 2. It is situated just 3.3 cm away from the beam-line, whereas the inner-most Pixel detector layer in LHC Run 1 was situated 5 cm away from the beam-line. In addition, the pixel sensor pitch of the IBL is 50 µm×250 µm compared to 50 µm×400 µm for other Pixel detector layers. The closer distance to the beam-line and finer pitch of the pixel sensors allow the IBL to provide the high-resolution position measurements needed for high-resolution tracking. A picture of the IBL being inserted into the Pixel detector is shown in Figure 4.5.

4.2.2 The Calorimeters

ATLAS employs sampling calorimeters to measure the energy of several types of outgoing particles. These calorimeters have layers of passive and active materials. Particles traversing the calorimeters will initiate particle showers in the layers of passive material, and the energy of the showering particles will be recorded by the active material. The ATLAS calorimeter

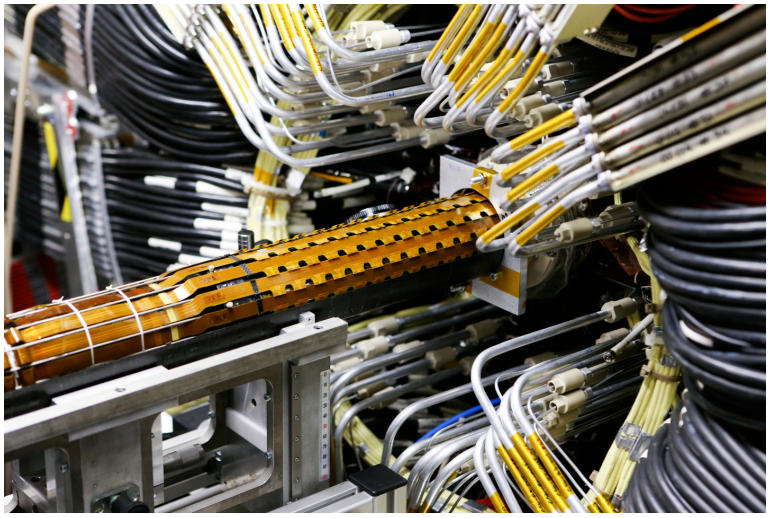

Figure 4.5: A photograph of the IBL being inserted into the center of the ATLAS detector around the LHC beam-line [52].

system consists of barrel and end-cap electromagnetic [53] and hadronic [54] calorimeters, and a rendering of the system is shown in Figure 4.6. The following sub-sections describe the two main calorimeter sub-systems.

The Electromagnetic Calorimeter

The ATLAS electromagnetic calorimeter system consists of three barrel layers and two end-cap layers on either end-cap. In the barrel region, the first, innermost layer has the finest granularity, $(\Delta\eta \times \Delta\phi) = (0.003 \times 0.1)$, the second layer has granularity of $(\Delta\eta \times \Delta\phi) = (0.003 \times 0.1)$, and the third, outermost layer has the coarsest granularity of $(\Delta\eta \times \Delta\phi) = (0.05 \times 0.025)$. Each layer of the electromagnetic calorimeter end-caps is divided into eight modules with granularity up to $(\Delta\eta \times \Delta\phi) = (0.1 \times 0.1)$.

The passive material of the electromagnetic calorimeters is lead, and the active material is liquid argon (LAr). Electrons and photons traversing the passive material produce electromagnetic showers, and the resulting charged particles pass through and ionize the LAr in the active material, producing electrical signals which are captured and read out by attached electrodes. The sampling layers of passive and active materials are arranged in an

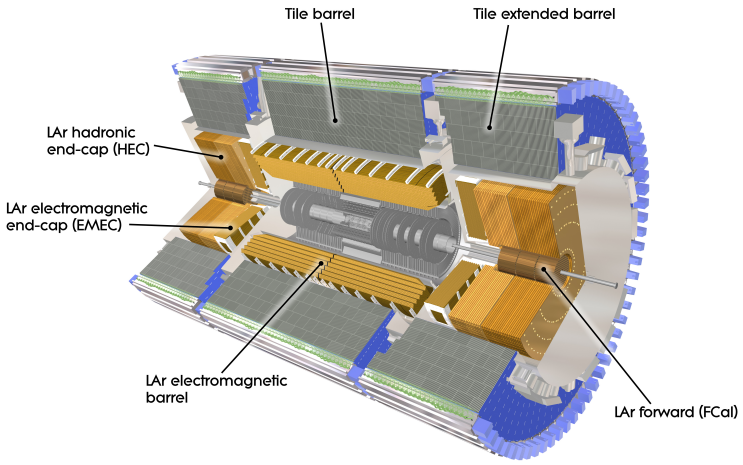

Figure 4.6: A rendering showing the ATLAS calorimeters [55].

accordion geometry for hermiticity, fast read-out, and a high signal-to-noise ratio.

The Hadronic Calorimeter

The ATLAS hadronic calorimeters consist of a barrel calorimeter in the range $|\eta| < 1.7$ and an extended barrel calorimeter in the range $1.5 < |\eta| < 3.2$. These barrel detectors are located around the electromagnetic calorimeter layers, and are designed to absorb hadrons which are not absorbed by the electromagnetic calorimeters.

The passive material of the hadronic calorimeters consists of iron plates and the active material consists of plastic scintillating tiles. Hadrons passing through the passive material undergo hadronic showers, and the resulting charged particles excite valence electrons in the active material, leaving electron-hole pairs. When the excited electrons fall back into their non-excited state, they emit photons that are detected by photon detectors, creating the signal to be read out.

4.2.3 The Muon Spectrometer

While the ATLAS calorimeters are designed to fully absorb most incident particles, there are cases where particles pass through the calorimeters. Neutrinos, for example, do not

interact at all with the ATLAS calorimeters, or other sub-detectors, and indeed are very difficult to detect at all in a collider environment with current technologies, so they are primarily reconstructed as "missing transverse energy." Muons also interact very little with the ATLAS calorimeters. This is because they are Minimum Ionizing Particles at the typical energies at which they are produced in LHC collisions. However, several technologies exist which allow for muon detection past the calorimeter system, and the ATLAS Muon Spectrometer [56] employs four different detector technologies.

The ATLAS Muon Spectrometer (MS) consists of three layers of barrel detectors, three layers of end-cap detectors at each end-cap, and three layers of detectors in the transition region between the barrel and end-caps. A rendering of the MS is shown in Figure 4.7. The barrel region covers the range $|\eta| < 1.05$ and the end-cap region covers the range $1 < |\eta| < 2.8$. The barrel detectors utilize Resistive Plate Chamber (RPC) [57] and Muon Drift Tube (MDT) [58] technologies. The end-cap detectors utilize MDT, Thin Gap Chamber (TGC) [59], and Cathode Strip Chamber (CSC) [60] technologies.

The barrel detector operates in a large magnetic field produced by a large barrel toroid which produces a field that is strongest in the range $|\eta| < 1.4$. Smaller toroid magnets in each end-cap produce magnetic fields which are strongest in the range $1.6 < |\eta| < 2.7$. Muons in the range $1.4 < |\eta| < 1.6$ are bent by a combination of the barrel and end-cap toroid magnets.

As is the case with the Inner Detector, the magnetic fields in the Muon Spectrometer allow for the measurement of muon momenta. These magnetic fields have a nominal strength of 0.5 T. The TGC and RPC detectors provide a very fast response to muon hits, making them ideal detectors to provide muon triggers. The MDT and CSC detectors provide high-resolution spatial measurements of incident muons, which are used for muon track reconstruction. As such, the MS is able to reconstruct muon tracks independently of the ID. Several muon reconstruction and identification algorithms are employed by ATLAS which rely on information from both the ID and the MS.

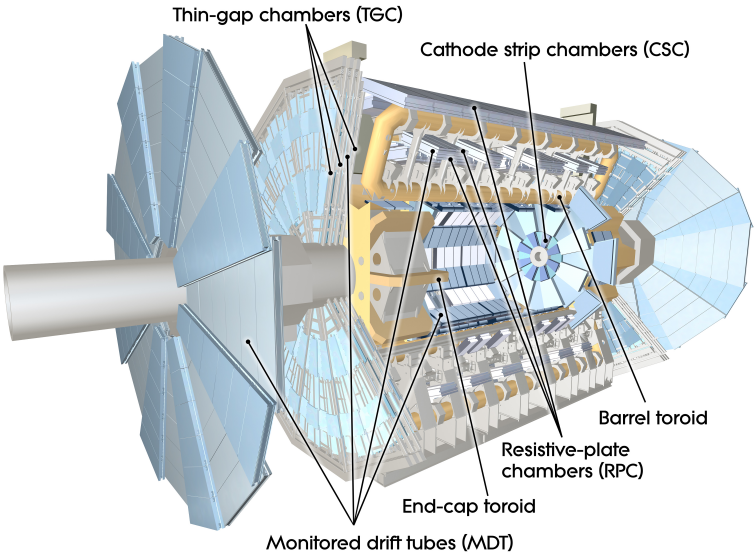

Figure 4.7: A rendering showing the ATLAS Muon Spectrometer and its sub-detectors [61].

4.3 The Trigger and Data Acquisition System

Proton-proton collisions occur roughly once every 25 ns at the ATLAS collision point, corresponding to a 40 MHz event rate. The total data from all ATLAS sub-detectors for a full event corresponds to several MB. As such, fully recording data from all proton-proton collisions would require a bandwith of dozens of TB per second - a feat not feasible with current technology over the long periods of time that ATLAS collects data. Because of this, ATLAS utilizes a trigger system which aims to record a reduced data set of proton-proton collisions which result in physical processes deemed interesting, such as Higgs production.

The ATLAS trigger system operates at two trigger levels, referred to as the Level 1 (L1) trigger and the High Level Trigger (HLT). The L1 trigger utilizes custom hardware to quickly analyze course granularity data from the ATLAS calorimeters and MS. If the L1 trigger decides an event should be kept, it sends a Level 1 Accept (L1A) signal to the full ATLAS detector, initiating a full read-out of all sub-detector data in regions of interest determined by the L1 trigger. The rate of L1As is nominally 100 KHz, reducing the total 40 MHz event rate by a factor of 400. The read-out data is then analyzed by the software-based

HLT. If the HLT decides an event should be kept, the event will be fully reconstructed and sent to long-term storage. The HLT accept rate is nominally 1 KHz. Thus, the combined L1 and HLT triggers effectively reduce the ATLAS event rate by a factor of 40000.

4.3.1 The Pixel Data Acquisition System Upgrade

A new data acquisition (DAQ) system accompanied the installation of the IBL into the Pixel detector system. This new system utilized both upgraded hardware and updated software in order to meet the bandwidth needs of the new IBL detector. In addition, the event rate and instantaneous luminosity of LHC Run 2 demanded a faster DAQ system, requiring the DAQ system of all three previous Pixel detector layers to be upgraded.

In order to ensure successful operation of the Pixel detector in LHC Run 2, the author worked extensively on the upgrade of the Pixel detector DAQ software in 2014 and 2015. Specific contributions were made in updating the DAQ software to run on new 64-bit computers which replaced the 32-bit computers used during LHC Run 1.

Chapter 5

DATA SETS AND MONTE CARLO SAMPLES

Details of the LHC data analyzed and Monte Carlo (MC) simulations used to model the data and generate signal signatures to search for are described in this chapter. Specifically, Section 5.1 describes the LHC data sets collected, and Section 5.2 describes the MC samples used to model the SM backgrounds and the DM signal MC samples generated, including a discussion of the choice of $Z'-$2HDM parameters chosen for simulation.

5.1 LHC Data Sets

The data set used by this analysis consists of the proton-proton collision data collected at $\sqrt{s} = 13$ TeV by the ATLAS detector during 2015, 2016, and 2017 of LHC Run 2. The data recorded during this period is summarized in Figure 5.1.

Of the 93 fb^{-1} luminosity delivered by the LHC, ATLAS recorded data for 86 fb^{-1}, corresponding to a 93% data collection efficiency. The data taking inefficiency can be explained by a few factors. Inefficiencies in the DAQ systems of individual ATLAS sub-detectors, or of ATLAS as a whole, can contribute to the overall data taking inefficiency. Along those same lines, detector dead time, defined as the time during which a detector is non-operational, can occur during data taking runs and contribute to the overall data taking inefficiency. Also, it takes a finite amount of time for the ATLAS detector to ramp up and become fully operational. This ramp up is referred to as a "warm start," and during this time, the ATLAS tracking detectors ramp up the high voltages necessary for their operation, and the Pixel detector system takes time to turn on its preamplifiers. During the ramp up time, the ATLAS detector may be unable to collect data, contributing to the overall data taking inefficiency.

Of the 86 fb^{-1} luminosity of data recorded by ATLAS, 79.8 fb^{-1} was selected for use in physics analyses, including this mono-Higgs analysis. The roughly 6 fb^{-1} of data not used

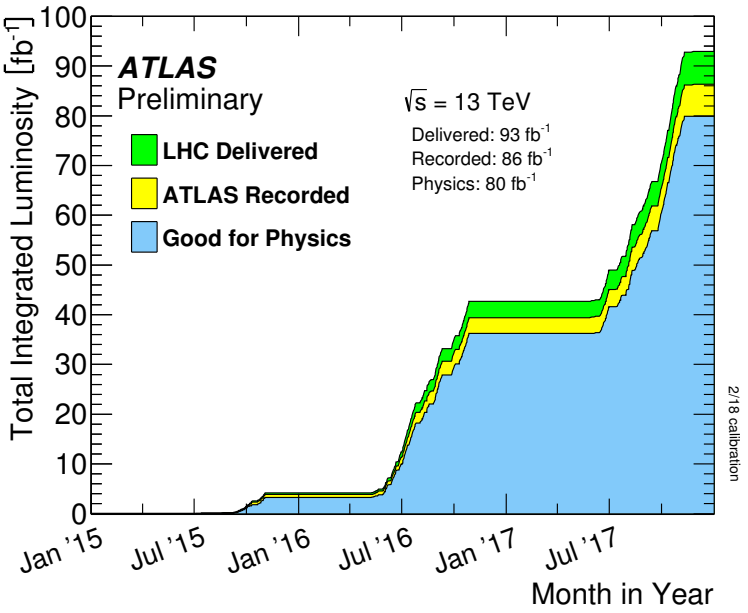

Figure 5.1: Plot of the integrated luminosity delivered by the LHC and recorded by ATLAS during the 2015, 2016, and 2017 data taking periods [62].

corresponds to events collected where data may be incomplete or corrupted due to issues in sub-detector DAQ systems, or to events collected where a substantial number of individual detector modules may be operating sub-optimally. A basic quality selection was applied to recorded data, including the requirement that all the relevant detector components are known to be in good operating condition, and a list of runs deemed good for physics analyses is created. This list is known as the "Good Run List," or GRL. A breakdown of the 79.8 fb^{-1} of integrated luminosity in the GRL by ATLAS data taking periods is shown in Appendix C.

The triggers used during the different data taking periods are described in detail in Chapter 8, but in short, missing transverse energy triggers were used to select Signal Region and some Control Region events and triggers selecting leptons were used to select other Control Region events.

5.2 Monte Carlo Samples

The LHC is capable of providing many proton-proton collisions, and the ATLAS sub-detectors are capable of recording a large amount of data from these collisions. This data is used to test theoretical predictions and physics models using Monte Carlo (MC) simulation.

The rules of the Standard Model are implemented in programs such as MadGraph which are used to generate each possible physics process that can occur in a proton-proton collision, such as the production of a Z boson in association with a gluon. This hard-scatter process is then fed into software such as Pythia which simulates various higher-level physical processes, such as the QCD radiation and hadronization which occur when a quark or gluon is produced in a hard-scatter process. Finally, the final state particles after this step are fed into detector simulation software, such as Geant, where the particles are digitized into the signals that the sub-detectors would measure.

After the digitization step, MC samples look just like recorded data in terms of format and can be fed into the same ATLAS reconstruction software used to analyze data. It is in this way that a consistent reconstruction is applied to both MC samples and to data, allowing for a direct comparison.

After reconstruction, the MC samples may not perfectly model data, even for very well-understood physical processes. Because of this, calibration procedures are used to match MC simulation to data and to derive uncertainties associated with the MC simulation.

Theoretically, one should simulate every single possible physical process with MC in order to compare to data. However, each physics analysis will implement an event selection designed to remove background processes, and in practice it becomes only necessary to produce MC samples of background processes known to pass the event selection. For the mono-Higgs analysis, the background processes considered were multi-jet production, $Z+$ jets and $W+$ jets production, diboson production, $t\bar{t}$ and single top production, and Vh production. In addition to these background processes, Dark Matter signal processes were also simulated using MC to compare to data.

5.2.1 Standard Model Monte Carlo Samples

A summary of the generators, PDFs, shower models, tunes, and cross-section orders used to simulate the background and signal processes is shown in Table 5.1. Z + jets and W + jets events were generated using SHERPA 2.2.1 [63] with the NNPDF3.0 PDF set [64] at NNLO in cross section and were split according to the flavor content and p_{T} of the jets in order to provide higher statistics in the analysis regions. Diboson events were generated with SHERPA 2.2.1 with the NNPDF3.0 PDF set at NLO in cross section.

$t\bar{t}$ events were generated using POWHEG-BOX v2 [65] with the NNPDF3.0 PDF set at NNLO+NNL in cross section and interfaced with PYTHIA 8.230 [66] to simulate particle showers using the A14 tune [67]. Single top events were generated using POWHEG-BOX v2 with the NNPDF3.0 PDF set at NLO or higher in cross section and interfaced with PYTHIA 8.230 to simulate particle showers using the A14 tune.

$qq \to Vh$ samples were generated using POWHEG-BOX v2+GOSAM+MINLO [68] [69] with the NNPDF3.0 PDF set at NNLO (QCD) and NLO (EW) in cross section and interfaced with PYTHIA8.212 using the AZNLO tune [70]. $gg \to Zh$ samples were generated using POWHEG-BOX v2 with the NNPDF3.0 PDF set at NLO+NLL [71] [72] [73] [74] [75] in cross section and interfaced with PYTHIA8.212 using the AZNLO tune.

Multi-jet events were generated with PYTHIA 8 with the NNPDF3.0 PDF set at LO in cross section and PYTHIA 8 was also used to simulate particle showers using the A14 tune.

Minimum bias events are overlaid on all Monte Carlo samples to simulate the effects of pile-up. The Monte Carlo pile-up distributions are then re-weighted to match those of data. Finally, the detector effects on all Monte Carlo samples are simulated using the ATLAS configuration of GEANT 4 [76].

The ATLAS detector conditions were substantially different between the 2015+2016 data taking periods and the 2017 data taking period. Because of this, two different sets of detector conditions were developed for the GEANT simulation and two different sets of MC simulated background and signal samples were generated to compare to 2015+2016 and 2017 independently. These are referred to as mc16a, the set of MC samples to be compared to 2015+2016 data, and mc16d, the set of MC samples to be compared to 2017 data.

Table 5.1: Summary of Monte Carlo samples used by the analysis.

Process	Generator	PDF	Shower Model	Tune	Cross-section Order
Multi-jet	Pythia 8	NNPDF2.3	Pythia 8	A14	LO
Z + jets	Sherpa 2.2.1	NNPDF3.0	Sherpa 2.2.1	Default	NNLO
W + jets	Sherpa 2.2.1	NNPDF3.0	Sherpa 2.2.1	Default	NNLO
Diboson	Sherpa 2.2.1	NNPDF3.0	Sherpa 2.2.1	Default	NLO
$t\bar{t}$	Powheg-Box v2	NNPDF3.0	Pythia 8.230	A14	NNLO+NNLL
Single Top	Powheg-Box v2	NNPDF3.0	Pythia 8.230	A14	NLO or higher
$qq \to Vh$	Powheg-Box v2+GoSam+MiNLO	NNPDF3.0	Pythia 8.212	AZNLO	NNLO (QCD), NLO (EW)
$gg \to Zh$	Powheg-Box v2	NNPDF3.0	Pythia 8.212	AZNLO	NLO+NLL
Z'−2HDM	MadGraph5_aMC@NLO 2.2.3	NNPDF2.3	Pythia 8	A14	LO

5.2.2 Dark Matter Monte Carlo Samples

As mentioned in Section 3.3.3, this analysis studies a 2D parameter space of the Z'−2HDM model by scanning over parameters m_A and $m_{Z'}$. The mass points used for this analysis are summarized in Table 5.2. For each mass point, 50000 hard-scatter events were simulated by MadGraph5_aMC@NLO 2.2.3 [77] with the NNPDF2.3 PDF set [64] at LO in cross section. The events were then interfaced with Pythia 8 and then finally fed into the ATLAS Geant 4 detector simulation.

The choice of mass points followed two guiding principles. The first guiding principle was to choose mass points to provide a wide array of different kinematic signatures in order for the search to cover a larger region of phase-space.

For example, the higher the mass of Z', the more boosted its decay products, h and $A(\chi\bar{\chi})$. The more boosted h and $A(\chi\bar{\chi})$, the more back-to-back they should be. Also, the more boosted h is, the more collimated the b-quark decay products of h should be. Figure 5.2 demonstrates these points by plotting the p_{T} of the Higgs particle, the p_{T} of the combined $\chi\bar{\chi}$ system, the angular separation $\Delta\phi$ between the Higgs particle and the $\chi\bar{\chi}$ system, and the ΔR separation between the b-quark decay products of the Higgs particle as a function of $m_{Z'}$ for a fixed $m_A = 500$ GeV. The figure also shows the leading and sub-leading b-quark p_{T} and the minimum $\Delta\phi$ separation between the two b-quarks from

Table 5.2: Tabulation of the signal mass points used in this analysis.

$m_{Z'}$ \ m_A	300 GeV	400 GeV	500 GeV	600 GeV	700 GeV	800 GeV
600 GeV	×	×				
800 GeV	×	×	×			
1000 GeV		×	×	×		
1200 GeV			×	×	×	
1400 GeV			×	×	×	×
1600 GeV	×		×	×	×	×
1800 GeV			×	×	×	×
2000 GeV		×	×	×	×	×
2200 GeV	×	×	×	×	×	
2400 GeV	×	×	×	×	×	
2600 GeV	×	×	×	×	×	
2800 GeV	×	×	×	×		
3000 GeV	×	×	×	×		

the Higgs decays and the combined $\chi\bar{\chi}$ system. These kinematic variables are all shown at truth-level, immediately after the hard-scatter process and before further shower or detector simulations.

Further truth-level kinematic plots demonstrating the range of kinematics provided by the 2D mass scan chosen for the $Z'-$2HDM samples are shown in Appendix D.

The second guiding principle was to choose mass points to take into account previous limits on the model set by ATLAS. For example, since the mass point ($m_A = 300$ GeV, $m_{Z'} = 1200$ GeV) was completely ruled out by previous searches, this mass point is not considered here. For another example, since previous limits got nowhere close to having sensitivity to the ($m_A = 800$ GeV, $m_{Z'} = 3000$ GeV) mass point, this mass point is not considered either. Also, neither previous iterations of this analysis nor this iteration target the region of phase-space where the Z' is produced off-shell, as the cross section of the mono-Higgs process in this region is highly suppressed and there is no chance of a search being sensitive to it. As such, mass points such as ($m_A = 500$ GeV, $m_{Z'} = 600$ GeV) are not considered.

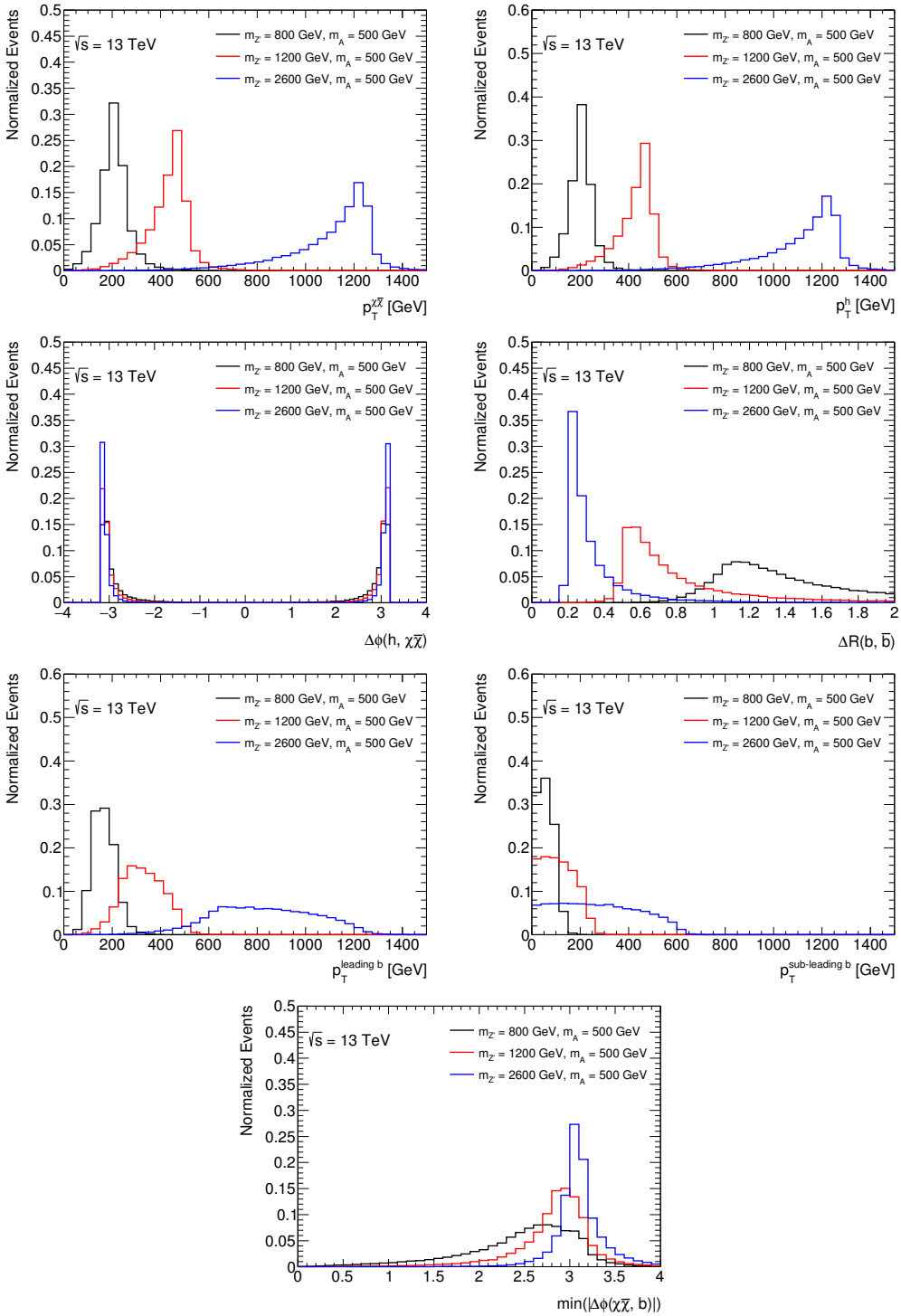

Figure 5.2: Truth-level mono-Higgs kinematic distributions for $m_A = 500$ GeV.

Chapter 6

ANALYSIS OVERVIEW

This search utilized two main analysis channels: a Resolved Channel for relatively low-boost signatures, and a Merged Channel for relatively high-boost signatures. A Signal Region is used to search for an excess over SM background processes associated with the mono-Higgs DM process, and Control Regions are defined to help determine the normalizations of the dominant backgrounds of the Signal Region. This chapter provides an overview of this analysis strategy, and is organized as follows. Section 6.1 describes the Resolved and Merged Channel signatures, motivating the reconstructed physics objects, which are defined in greater detail in Chapter 7, and the event selections, which are defined in greater detail in Chapter 8. Then, Section 6.2 outlines the Signal and Control Regions considered.

6.1 Resolved and Merged Channels

The mono-Higgs signal process results in a Higgs boson produced back-to-back with a $\chi\bar{\chi}$ system. The Higgs boson further decays to b-quarks, which hadronize to b-hadrons. The $\chi\bar{\chi}$ system cannot be detected by ATLAS, so it will leave a signature of missing transverse energy in the ATLAS detector, which is described in more detail in Section 7.7. The b-quark decay products of the Higgs boson will produce hadronic showers, which can be reconstructed as objects called jets. Jets are described in detail in Section 7.5.

If the boost of the produced Higgs boson is low enough, the hadronic shower originating from the b-quarks can be reconstructed as two jets by the standard jet algorithm used by ATLAS, which effectively reconstructs jets as conic objects with radius parameter $R = 0.4$ using calorimeter clusters as input. The Higgs boson can then be reconstructed and identified using this di-jet system. This is the technique employed by the mono-Higgs Resolved Channel, and is shown in a cartoon in Figure 6.1.

If the boost of the produced Higgs boson is too high, the b-quark decay products of the

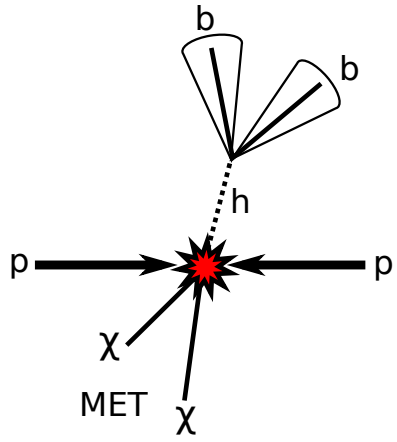

Figure 6.1: A cartoon showing a Resolved Channel mono-Higgs event where the Higgs boson has a low enough boost that its b-quark decay products can be reconstructed as individual $R = 0.4$ calorimeter jets. The Higgs boson decays promptly, though the cartoon shows a finite Higgs boson flight due to illustration constraints.

Higgs boson will become too collimated to reconstruct as conic objects with radius parameter $R = 0.4$. In this case, the Higgs boson is directly reconstructed as a single jet with a large radius parameter of $R = 1.0$ using calorimeter clusters. To aid in the identification of the Higgs boson, the two b-quark decay products of the Higgs are independently reconstructed as variable radius jets using tracks as input. These variable radius track jets do not reconstruct the 4-momentum of the Higgs boson well, but are extremely useful in identifying the b-hadron decays. This Higgs boson reconstruction technique is employed by the mono-Higgs Merged Channel, and is shown in a cartoon in Figure 6.2.

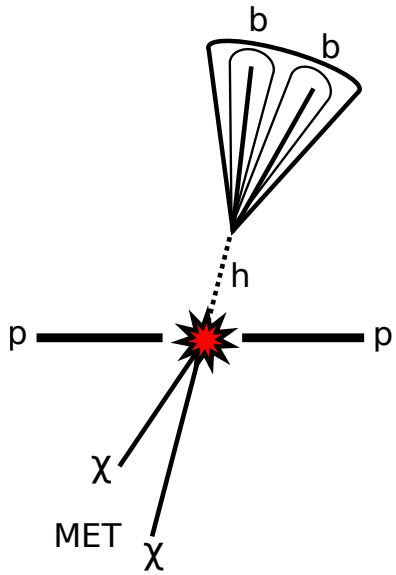

Figure 6.2: A cartoon showing a Merged Channel mono-Higgs event where the Higgs boson has a high boost and is reconstructed using a boosted Higgs tagging technique. The Higgs boson decays promptly, though the cartoon shows a finite Higgs boson flight due to illustration constraints.

6.2 Signal and Control Regions

The Signal Region (SR) aims to select events with large missing transverse energy and a reconstructed Higgs candidate, using either the Resolved Channel technique or the Merged Channel technique. Since no isolated leptons are expected to be produced by signal events, a lepton veto is implemented in the Signal Region, and the Signal Region is often referred to as the 0-lepton Signal Region. The details of the Signal Region event selection are thoroughly detailed in Section 8.3. The dominant backgrounds that contaminate the Signal Region are $Z+$jets, $W+$jets, and $t\bar{t}$. To help determine the normalizations of these backgrounds, dedicated Control Regions (CRs) are defined.

A 1-lepton Control Region selecting one muon or anti-muon is defined to obtain a high-purity of $W+$jets and $t\bar{t}$ events, and a 2-lepton Control Region selecting opposite charge electrons or muons is defined to obtain a high-purity of $Z+$jets events. Apart from the selection on leptons, these three regions are as similar to each other as possible to ensure that the normalizations of backgrounds derived from the Control Regions can be reliably applied to the Signal Region. The full details of the event selections of these three regions are described in Chapter 8, and further discussion of the background modelling using the Control Regions is presented in Chapter 9. A final statistical fit of MC simulated events to data, taking into account all relevant calibrations and their uncertainties, is performed simultaneously on all analysis regions, with the normalizations of $Z+$jets, $W+$jets, and $t\bar{t}$ treated as free parameters. The details of this combined fit are described in Section 11.1.

In addition to separating events into regions based on the number of leptons present, this analysis also bins events in the Signal and Control Regions into the number of jets which are tagged as having originated from b-quarks, known as b-jets. The topic of b-tagging is detailed in Section 7.5.2. Only events which contain two b-jets are considered for the final fit, but some studies of events which contain 0 or one b-jet are also presented. Diagrams schematically showing the Signal and Control Regions used by the analysis, and their SM background compositions, are shown in Figure 6.3.

Event yields in the two b-tag bin after the event selection of the Signal Region are binned in four different bins of missing transverse energy and several bins of the reconstructed Higgs

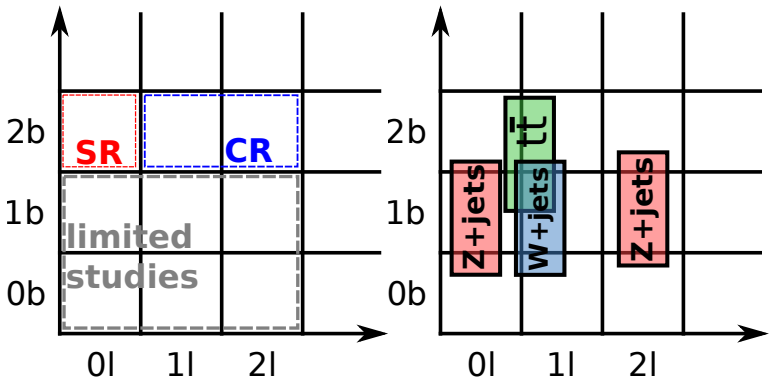

Figure 6.3: 6.3a: a diagram showing the Signal and Control Regions and b-tag binning used to classify events considered by this analysis. 6.3b: the qualitative relative compositions of the dominant backgrounds in the Signal and Control Regions.

candidate mass.

Event yields in the two b-tag bin after the event selection of the Control Regions are binned in four different bins of proxies to the missing transverse energy. The missing transverse energy proxies used by the Control Regions are further discussed in Chapters 8 and 9. The events in the 1-lepton Control Region are additionally binned in the charge of the selected lepton.

A diagram schematically showing the bins for the Signal Region is shown in Figure 6.4. In the figure, the blue dashed line representing the trigger $E_{\mathrm{T}}^{\mathrm{Miss}}$ threshold is to be taken qualitatively as the $E_{\mathrm{T}}^{\mathrm{Miss}}$ trigger threshold ranges from 70 GeV to 110 GeV, depending on the data collection period, and the threshold is applied to the trigger $E_{\mathrm{T}}^{\mathrm{Miss}}$ value, which differs from the full offline $E_{\mathrm{T}}^{\mathrm{Miss}}$ calculation. Details of the $E_{\mathrm{T}}^{\mathrm{Miss}}$ trigger are further discussed in Section 8.1.

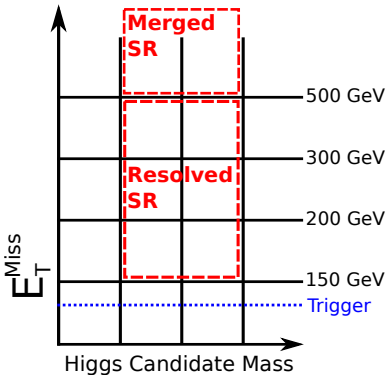

Figure 6.4: Diagram showing the final binning scheme used for the Signal Region. The number of bins of and range of the Higgs candidate mass depends on the analysis channel. The $E_{\mathrm{T}}^{\mathrm{Miss}}$ trigger threshold ranges from 70 GeV to 110 GeV, depending on the data collection period, and the threshold is applied to the trigger $E_{\mathrm{T}}^{\mathrm{Miss}}$ value, which differs from the full offline $E_{\mathrm{T}}^{\mathrm{Miss}}$ calculation, so the blue dashed line representing the trigger $E_{\mathrm{T}}^{\mathrm{Miss}}$ threshold is to be taken qualitatively here.

Chapter 7

PHYSICS OBJECTS

This chapter outlines the physics objects used by this search in the reconstruction of events. Boosted Higgs jet reconstruction is described in depth as several new techniques have been developed with searches like this in mind. Indeed, one such technique, the variable radius track jet technique, is employed by ATLAS for the first time in a search here.

This chapter is organized as follows. The basic calorimeter cluster, tracks, and vertex objects reconstructed by the ATLAS detector are described in Section 7.1. The criteria required for primary vertices is described in Section 7.2. The reconstruction of and selection criteria for electrons are described in Section 7.3 and muons in Section 7.4. The many types of jets that are used by this analysis to reconstruct the Higgs candidate in different kinematic regions are described in Section 7.5. Taus, which are also reconstructed as jets, are described in Section 7.6. The reconstruction of missing transverse energy, or $E_{\mathrm{T}}^{\mathrm{Miss}}$, is discussed next in Section 7.7, as it relies on the reconstruction of previously mentioned objects, and the missing transverse energy significance definitions are described in Section 7.8. Finally Higgs tagging is described in detail in Section 7.9.

7.1 Topological Clusters, Tracks, and Vertices

The most basic information recorded by the ATLAS detectors are energy deposits in calorimeter cells, and hits in the various layers of the ID and MS. Energy deposits in calorimeter cells are clustered using a 3D clustering algorithm into what are known as topological calorimeter clusters, calorimeter clusters, or just topo-clusters. Hits in the ID and MS are connected to form tracks to reconstruct the trajectory of charged particles. Vertices are reconstructed from clusters of tracks, and represent locations where either scatter or decay processes occurred.

Table 7.1: Basic quality selections for tracks used to reconstruct primary and pile-up vertices.

primary/pile-up vertex track selection	
Selection	Purpose
$p_{\mathrm{T}} > 0.4$ GeV	reject soft fake tracks
$\lvert\eta\rvert < 2.5$	in ID fiducial volume
≥ 9 (11) hits between the Pixel and SCT detectors for $\lvert\eta\rvert \leq 1.65$ ($\lvert\eta\rvert > 1.65$)	enough hits for track reconstruction
≤ 1 (2) hits in a Pixel (SCT) detector layer shared by multiple tracks	good hit quality
0 missing hits in the Pixel detector when a hit is expected	good hit quality
≤ 1 missing hits in the SCT detector when hits are expected	good hit quality

7.2 Primary Vertices

Vertex reconstruction in ATLAS during LHC Run 2 is described in detail in Reference [78]. All vertices are required to have at least two tracks, where the basic track selection criteria are outlined in Table 7.1.

Basic p_{T} and η requirements ensure that each track is well contained within the fiducial volume of the ID and of a high enough momentum to reduce the chance that it is a fake track. Requirements on the number of non-shared, and non-missing hits in the ID sub-detectors ensure that there is enough good quality hit information to give confidence in the track reconstruction. The criteria for a "missing hit" in a Pixel or SCT layer is that the track is extrapolated through an active part of the layer, yet a hit is not present in the layer while hits are present in surrounding layers.

The primary vertex in an event is then chosen to be the vertex with the largest $\sum_{\text{tracks}} p_{\mathrm{T}}^2$. This is to ensure that the primary vertex chosen in an event has the greatest activity, and thus represents the hardest scatter process of all vertices in the event. The other, non-primary, vertices are considered pile-up vertices.

Table 7.2: Definitions for the two categories of electrons used in this analysis.

Electron Type	p_{T}[GeV]	$\lvert\eta\rvert$	$d_0/\sigma(d_0)$	$\lvert z_0 \cdot \sin\theta\rvert$ [mm]	Likelihood	Isolation
`VHLoose`	> 7	< 2.47	< 5	< 0.5	`LooseLLHBLayer`	`LooseTrackOnly`
`ZHSignal`	> 27	< 2.47	< 5	< 0.5	`LooseLLHBLayer`	`LooseTrackOnly`

7.3 Electrons

Electrons both leave hits in the ATLAS inner detector layers and deposit energy in the ATLAS electromagnetic calorimeter. As such, an electron is reconstructed from an electromagnetic calorimeter cluster matched to an ID track. The electromagnetic calorimeter cluster is reconstructed using a sliding window algorithm, as described in Reference [79]. To account for energy losses of the electron due to bremsstrahlung, a Gaussian Sum Filter algorithm is used to refit the ID track [80]. Electrons are identified using a likelihood-based variable which takes into account variables related to the electromagnetic calorimeter clusters, such as those which characterize the longitudinal and transverse shower profiles, variables related to the ID tracks (including quality criteria and the presence of high-threshold TRT hits), and variables quantifying the successful matching of the electromagnetic calorimeter cluster and ID track [81].

Several working points of the likelihood variable exist that offer analyses the choice to apply looser or tighter requirements on electrons. This analysis uses the `LooseLLHBLayer` [81] working point. In addition to the likelihood variable, this analysis applies further selection criteria on electrons to form two categories of electrons: `VHLoose` and `ZHSignal`. The definitions of `VHLoose` and `ZHSignal` electrons are summarized in Table 7.2.

The `VHLoose` definition is looser than the `ZHSignal` definition and is used when a high electron efficiency is desired in order to veto events in which electrons are not expected, such as events in the Signal Region. The `ZHSignal` definition is used when a high electron purity is desired, which is the case for some Control Regions.

7.4 Muons

Muons leave tracks in both the ID and the MS, and also leave very small energy deposits in the calorimeters. As such, there are a number of ways that muons can be reconstructed using combinations of information from the ID, the calorimeters, and the MS. Since the η coverages of the ID and MS differ, reconstruction algorithms using information from just one or the other of these detectors have been developed. The four muon reconstruction techniques are summarized here [82]:

1. Combined muons: muons reconstructed from MS tracks matched to ID tracks.

2. Segment-tagged muons: muons reconstructed from ID tracks matched to a MS track segment. The Segment-tagged muon definition is looser than the Combined muon definition and is meant to increase efficiency when muons only pass through one MS chamber.

3. Calorimeter-tagged muons: muons reconstructed from ID tracks matched to an energy deposit in the calorimeter compatible with a Minimum Ionizing Particle in the region $|\eta| < 0.1$, where the MS is only partially instrumented so MS tracks are not available.

4. Extrapolated muons: muons reconstructed from MS tracks matched to the interaction points in the region $2.5 < |\eta| < 2.7$, where the ID is not instrumented so ID tracks are not available.

Using these reconstruction techniques, different muon identification quality definitions can be constructed. The identification classifications used in this analysis are denoted "`Loose`" and "`Medium`."

"`Loose`" muons are defined as muons reconstructed using any of the four reconstruction techniques described. "`Medium`" muons are muons reconstructed using either the Combined muon or Extrapolated muon techniques. In addition, for Combined muons, it is required that there are ≥ 3 hits in at least two MDT layers when $|\eta| > 0.1$, and when $|\eta| < 0.1$, MS

Table 7.3: Definitions for the different categories of muons used in this analysis.

Muon Type	p_{T}[GeV]	$\lvert\eta\rvert$	$d_0/\sigma(d_0)$	$\lvert z_0 \cdot \sin\theta\rvert$ [mm]	Id. Criteria	Isolation
`VHLoose`	> 7	< 2.7	< 3	< 0.5	`Loose`	`LooseTrackOnly`
`WHSignal`	> 25	< 2.5	< 3	< 0.5	`Medium`	`FixedTrackTTTight`
`ZHSignal`	> 25	< 2.5	< 3	< 0.5	`Loose`	`LooseTrackOnly`

tracks are required to have hits in at least one MDT layer and no more than one MDT hole layer. For Extrapolated muons, hits are required in at least three MDT/CSC layers.

On top of these standard `Loose` and `Medium` ATLAS muon definitions, additional criteria are applied to muons in different regions of this analysis in order to have a tighter selection when a high muon purity is desired in Control Regions and a looser selection when muons are not desired and are vetoed in the Signal Region. A summary of the muon definitions used in this analysis is presented in Table 7.3.

7.5 Jets

Since quarks and gluons carry color charge, they will radiate gluons when they accelerate, causing a particle shower. Also, due to quark confinement, this shower of quarks and gluons will undergo hadronization, where quarks and gluons will combine to form color-neutral hadrons. These hadrons may also further decay. This process creates what is referred to as a jet - a cone-like shower of particles which originates from a single quark or gluon.

In order to reconstruct the original quark or gluon, the many final state particles of the hadronic shower, or the tracks or calorimeter clusters which reconstruct these final state particles, must be clustered together according to a jet algorithm. Many different jet clustering algorithms exist, but the algorithm employed for most of the jets considered in this research is the anti-k_{T} algorithm [83], which tends to cluster together high p_{T} inputs first before clustering together lower p_{T} inputs. Appendix E goes into some depth on the subject of jet clustering algorithms, including the anti-k_{T} algorithm. For now it suffices to state that jets are objects formed from the clustering of particles, tracks, or calorimeter

clusters in order to reconstruct the originating quark or gluon. The main parameter of the anti-k_{T} algorithm is the radius parameter, R. This parameter effecively sets the maximum size of the radius of the jet cone.

7.5.1 Small-R Jets

Small-R jets are defined in this analysis as jets reconstructed using the anti-k_{T} algorithm with $R = 0.4$, using calorimeter clusters as inputs. The calorimeter clusters are calibrated to the electromagnetic scale according to Reference [84], the jet energy scale calibration scale factors and uncertainties are determined according to Reference [85], and the jet energy resolution is calibrated according to Reference [86]. The small-R jets used in the analysis are separated into the following categories.

Central Jets

Central jets are used to reconstruct Higgs candidates when the Higgs has a low enough momentum that its b-hadron decay products can be resolved by $R = 0.4$ jets and are defined as small-R jets with $|\eta| < 2.5$ and $p_{\mathrm{T}} > 20$ GeV. Central jets with $|\eta| < 2.4$ and 20 GeV $< p_{\mathrm{T}} <$ 60 GeV are required to have a jet vertex tagger value of JVT > 0.59. The jet vertex tagger (JVT) observable is constructed from tracking information in order to discriminate against jets originating from pile-up vertices [87].

This set of jets, when ordered according to decreasing p_{T}, will be referred to as j_c, with $j_{c,1}$ and $j_{c,2}$ referring to the leading and sub-leading j_c jets, respectively.

Forward and Central+Forward Jets

Forward jets are small-R jets with $2.5 < |\eta| < 4.5$ and $p_{\mathrm{T}} > 30$ GeV. These jets are not used to reconstruct Higgs candidates, but can be used by event selections to reduce backgrounds.

The set of central jets, ordered according to decreasing p_{T}, combined with forward jets, also ordered according to decreasing p_{T}, will be referred to as j_{cf}, j_{cf2} when only two such jets are present in an event, or j_{cf3} when referring only to the leading three jets in a set containing three or more such jets.

7.5.2 b-Tagging

The origins of most jets are quarks or gluons (or particles which decay to quarks or gluons). However, given the 4-momentum information of a jet alone, it is very difficult to determine which type of quark or gluon created the jet. Luckily, an extensive set of techniques have been developed to identify whether or not a jet originated from a b-quark, and the mono-Higgs signal process results in a Higgs decaying to b-quarks. These techniques are referred to as b-tagging.

Performing b-tagging is possible because of the long lifetime of b-hadrons ($\mathcal{O}$(ps)), which is due to the large mass of b-hadrons, $\sim$ 5 GeV [7]. Thus, b-hadrons with several GeV of energy will then travel $\mathcal{O}$(mm) before decaying. Since the resolution of the ATLAS Pixel detector is $\mathcal{O}$(µm), it is essential in resolving the decay vertices of b-hadrons, sometimes referred to as "secondary vertices." Also, tracks originating from the b-hadron decay vertex tend to have large impact parameters (IPs) with respect to the primary vertex. Thus, variables can be constructed to take advantage of these unique IP and secondary vertex characteristics. A cartoon illustrating these traits of jets originating from b-quarks/hadrons is shown in Figure 7.1.

Since most jet algorithms employed by ATLAS use calorimeter clusters as inputs, yet these b-tagging variables require the use of tracks, a procedure to associate tracks with jets must be used. The track-to-jet association procedure was optimized on small-R jets, but works reasonably well on other jet types for which b-tagging is commonly used. The track-to-jet association will associate tracks within a given radius around the jet axis. The radius used depends on the p_{T} of the jet according to the following equation:

$$R_{\mathrm{assoc}} = 0.239 + e^{-1.22-1.64\cdot 10^{-5}\cdot p_{\mathrm{T}}} \tag{7.1}$$

where p_{T} is in units of MeV. Tracks which match this criterion with respect to more than one jet are associated to the jet whose axis they are closer to.

The final discriminating variable for b-tagging used by ATLAS is mv2c10 [89]: a variable constructed from feeding several IP, secondary vertex, and tertiary vertex variables into a

[7] t-quarks are the only quarks heavier than b-quarks, but since they decay almost exclusively to W bosons and b-quarks, t-quark reconstruction requires both W boson identification and b-hadron identification

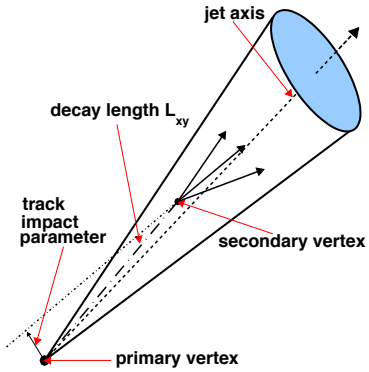

Figure 7.1: A cartoon showing the characteristics of a jet originating from a b-quark/hadron [88].

boosted decision tree (BDT). The "mv" stands for "multi-variate," in reference to the BDT, the "2" refers to "LHC Run 2" (a slightly different multi-variate-based discriminant was used during LHC Run 1), and the "c10" indicates that the BDT was trained with a sample of signal jets containing 10% of jets originating from c-quarks and 90% of jets originating from b-quarks.

The b-tagging efficiencies and mis-tag rates for jets originating from b-quarks [90], c-quarks [91], and light-quarks [92] are calibrated using high purity $t\bar{t}$ samples. The calibrations are binned in p_{T} and η and the calibration of b-tagging efficiency for jets originating from b-quarks is also extrapolated for high p_{T} jets for which not enough statistics are available for dedicated calibrations.

7.5.3 Large-R Jets

Not all physics objects can be reconstructed well with the same jet algorithm. In particular, jets that are the result of the collimated decay products of heavy particles, or jets from low p_{T} gluons, tend to require the use of a large cone size to contain all of the decay products for accurate reconstruction. Large-R jets are defined in ATLAS as jets reconstructed with the anti-k_{T} algorithm with $R = 1.0$ using calorimeter clusters calibrated using the local

calibration weighting scheme [84].

With such a large radius parameter, these jets tend to contain many constituents which originate from pile-up, as the larger the jet size, the more chance there is for particles from pile-up interactions to contaminate the jet. To reduce some of the contribution from pile-up, the jets are groomed using the "trimming" technique. This technique involves reclustering all of the jet's constituents using the k_{T} algorithm [93], which tends to cluster together low p_{T} constituents first, with $R = R_{\mathrm{sub}}$. This creates a set of subjets with radius parameter R_{sub}. Subjets whose fraction of the original large-R jet's energy is below f_{cut} are removed from the original large-R. The values for R_{sub} and f_{cut} used here are 0.2 and 0.05, respectively.

The resulting jet is referred to as a trimmed large-R jet, and is what will be used to reconstruct Higgs candidates when the b-quark decay products of the Higgs are too collimated to resolve using small-R jets.

7.5.4 $R = 0.2$ Track Jets

$R = 0.2$ track jets (sometimes referred to as FR, for "fixed radius," track jets) are used by a technique of boosted Higgs tagging which was employed by previous iterations of the mono-Higgs analysis. The iteration of the mono-Higgs analysis which is the focus of this thesis uses variable radius track jets instead. However, it is useful to discuss $R = 0.2$ track jets here as comparisons between the use of $R = 0.2$ track jets in Higgs tagging and the use of variable radius track jets in Higgs tagging are made extensively in Section 7.9.

$R = 0.2$ track jets are jets clustered from ID tracks using the anti-k_{T} algorithm with a radius parameter of $R = 0.2$. In order to reduce the number of fake tracks and tracks from pile-up vertices, the selection criteria shown in Table 7.4 are applied to tracks used as input to the track jet clustering.

The quality criteria applied to tracks used in track jet reconstruction are similar to the criteria applied to tracks used for primary vertex reconstruction, described in Section 7.2. The same p_{T} and η requirements ensure that each track is well contained within the fiducial volume of the ID and of a high enough momentum to reduce the chance that it is a fake track.

Table 7.4: Basic quality selections for tracks used to cluster track jets.

track jet track selection	
Selection	Purpose
$p_{\mathrm{T}} > 0.4$ GeV	reject soft fake tracks
$\lvert\eta\rvert < 2.5$	in ID fiducial volume
≥ 7 hits between the Pixel and SCT detectors	enough hits for track reconstruction
≤ 1 hit in the Pixel detector shared by multiple tracks	good hit quality
≤ 1 missing hit in the Pixel detector when a hit is expected	good hit quality
≤ 2 missing hits in the SCT detector when hits are expected	good hit quality
$\lvert z_0 \cdot \sin(\theta)\rvert < 3$ mm	reject tracks from pile-up

Requirements, looser than those applied to the tracks used for primary vertex reconstruction, on the number of non-shared, and non-missing hits in the ID sub-detectors ensure that there is enough good quality hit information to give confidence in the track reconstruction. The additional requirement that the longitudinal impact parameter of the tracks with respect to the primary vertex be small is particularly effective at rejecting tracks originating from pile-up vertices.

The b-tagging efficiency for $R = 0.2$ track jets originating from b-quarks is calibrated independently using the same technique applied to small-R jets. However, the b-tagging mis-tag rate for $R = 0.2$ track jets originating from c-quarks and light quarks, and the b-tagging efficiency extrapolation for high p_{T} $R = 0.2$ track jets originating from b-quarks, is not done independently, but rather is taken from the calibrations done on small-R jets.

The basic selection criteria for $R = 0.2$ track jets are $p_{\mathrm{T}} > 10$ GeV, $|\eta| < 2.5$, and $N_{\mathrm{constituents}} \geq 2$.

7.5.5 Variable Radius Track Jets

Variable radius (VR) track jets clustered with the anti-k_{T} algorithm were used in this analysis to reconstruct the b-hadrons resulting from the $h \to b\bar{b}$ decay when the Higgs boson is too boosted to reconstruct with two small-R jets, as described further in Section 7.9.1.

VR track jets are clustered from tracks with the same track quality selections as used for $R = 0.2$ track jets, as outlined in Section 7.5.4.

The details of the VR algorithm are elaborated in Appendix E. Here, it is sufficient to know that the algorithm clusters inputs where the effective radius parameter of the clustering, R_{eff}, is proportional to the inverse of the p_{T} of the jet as it is being formed (known as a pseudo-jet). The constant of proportionality, ρ, can be optimized for a particular application and can typically be related to the mass of the origin particle of a jet and the number of decay products of that particle. The algorithm can also impose maximum and minimum values for R_{eff}, referred to as R_{max} and R_{min}, respectively. These too can be optimized for the particular application.

The particular values of ρ, R_{max}, and R_{min} chosen for this analysis were 30 GeV, 0.4, and 0.02, respectively. The optimization studies which led to these choices will be discussed in Section 7.9.1.

As is the case with $R = 0.2$ track jets, the b-tagging efficiency for VR track jets originating from b-quarks is calibrated independently using the same technique applied to small-R jets. An additional requirement that the ΔR separation between VR track jets be greater than R_{min} is applied to ensure that the VR track jets used for calibration are not concentric as it was found that the b-tagging performance for VR track jets is unstable for concentric jets [2].

The b-tagging mis-tag rate for VR track jets originating from c-quarks and light quarks, and the b-tagging efficiency extrapolation for high p_{T} VR track jets originating from b-quarks, is taken from the calibrations done on small-R jets.

The basic selection criteria for VR track jets were $p_{\text{T}} > 10$ GeV, $|\eta| < 2.5$, and $N_{\text{constituents}} \geq 2$.

7.6 Tau

Tau particles are not expected in signal events, so a tau veto is implemented in this analysis. Hadronic tau decays are reconstructed as small-R jets and identified using Boosted Decision Trees trained on variables which can discriminate tau-jets from QCD jets. Conceptually, this approach is very similar to identifying b-jets. The key characteristic of tau decays

which can be used to differentiate them from QCD jets is that tau decays typically result in either one or three charged hadrons (typically pions and kaons) potentially accompanied by neutral hadrons [14]. The charged hadrons tend to be collimated along the axis of the tau-jet. Variables which exploit these features, such as the fraction of transverse energy of calorimeter clusters in a narrow cone around the jet axis or the fraction of transverse momentum of tracks associated to the jet in a narrow cone around the jet axis, are fed into two BDTs - one which constructs a discriminant between QCD jets and 1-prong tau decays, and one which constructs a discriminant between QCD jets and 3-prong tau decays [94].

For both 1-prong and 3-prong BDTs, `Loose`, `Medium`, and `Tight` working points are defined. This analysis defines taus using the `Loose` working point, on top of which a few extra requirements are placed. Tau-jets are required to have $p_{\mathrm{T}} > 20$ GeV and $|\eta| < 2.5$, excluding the region $1.37 < |\eta| < 1.52$ (there is a gap in the instrumentation of the calorimeters in this region). Also, either one or three charged tracks are required to be associated to the tau-jet.

An "extended" tau definition is also used by this analysis in an "extended tau veto" targeting leptonic decays of W bosons, primarily to suppress $t\bar{t}$ events. These "extended" taus are reconstructed as small-R jets with $[1:4]$ charged tracks and with the additional requirement $\Delta\phi(\mathrm{jet}_{\tau}^{\mathrm{extended}}, E_{\mathrm{T}}^{\mathrm{Miss}}) < 22.5°$.

7.7 Missing Transverse Energy / Momentum

Due to the cylindrical symmetry of the ATLAS detector and the head-on collisions which take place at its center, conservation of momentum requires that the sum of the transverse momenta of all particles produced in collisions be 0. If a particle cannot be detected (such as neutrinos or Dark Matter), then the sum of the transverse momenta of all detected particles will not be 0. From this transverse momentum imbalance, the existence of particles which are not directly detected can be inferred. The vector representing the transverse momentum imbalance in the detector is referred to as the "missing transverse energy," or "$\mathbf{E}_{\mathrm{T}}^{\mathrm{Miss}}$," with absolute value "$E_{\mathrm{T}}^{\mathrm{Miss}}$," or "MET."

Since the exact momenta of all particles produced is not available, the experiment must utilize the momenta of fully reconstructed and calibrated physics objects to reconstruct

$E_{\mathrm{T}}^{\mathrm{Miss}}$. Slightly different definitions for $E_{\mathrm{T}}^{\mathrm{Miss}}$ can be constructed by considering different sets of physics objects in the calculation of $E_{\mathrm{T}}^{\mathrm{Miss}}$. This analysis uses the definition of $E_{\mathrm{T}}^{\mathrm{Miss}}$ referred to as "$\mathrm{MET_{TST}}$" which considers the following physics objects in its calculation:

- electrons: fully calibrated `VHLoose` electrons
- muons: fully calibrated `VHLoose` muons
- jets: fully calibrated small-R jets selected according to Reference [95]
- unassoc. tracks: tracks not associated to any reconstructed object

$\mathrm{MET_{TST}}$ is then calculated to be:

$$\mathrm{MET_{TST}} \equiv -\left|\sum \mathbf{p}_{\mathrm{T}}^{\mathrm{electrons}} + \sum \mathbf{p}_{\mathrm{T}}^{\mathrm{muons}} + \sum \mathbf{p}_{\mathrm{T}}^{\mathrm{jets}} + \sum \mathbf{p}_{\mathrm{T}}^{\mathrm{unassoc.\ tracks}}\right| \tag{7.2}$$

where the "electrons," "muons," "jets," and "tracks" used are defined in the preceding list. The contribution of tracks in this definition of $E_{\mathrm{T}}^{\mathrm{Miss}}$ is referred to as the "track soft term" and is the origin of the "TST" in "$\mathrm{MET_{TST}}$."

A related variable, "missing transverse momentum" (or "$p_{\mathrm{T}}^{\mathrm{Miss}}$") is also employed by this analysis. It is defined as the negative vector sum of transverse momenta of all tracks associated with the primary vertex. This variable is useful in reducing beam-induced and non-collision background events [96].

7.8 Missing Transverse Energy Significance

Different definitions of "missing transverse energy significance" attempt to evaluate the degree to which the reconstructed $E_{\mathrm{T}}^{\mathrm{Miss}}$ is consistent with momentum resolution and particle identification efficiencies. Two definitions of missing transverse energy significance are used by this analysis. The first, referred to in this document by $E_{\mathrm{T}}^{\mathrm{Miss,Sig}}$, is defined as follows:

$$E_{\mathrm{T}}^{\mathrm{Miss,Sig}} \equiv \frac{E_{\mathrm{T}}^{\mathrm{Miss}}}{\sqrt{\sum E_{\mathrm{T}}}} \tag{7.3}$$

where $\sum E_{\mathrm{T}}$ is defined as the scalar sum of the components that make up $E_{\mathrm{T}}^{\mathrm{Miss}}$, with the exclusion of the unassoc. track term, as follows:

$$\sum E_{\mathrm{T}} \equiv \sum p_{\mathrm{T}}^{\mathrm{electrons}} + \sum p_{\mathrm{T}}^{\mathrm{muons}} + \sum p_{\mathrm{T}}^{\mathrm{jets}} \tag{7.4}$$

A high value of $E_{\mathrm{T}}^{\mathrm{Miss,Sig}}$ indicates an event in which $E_{\mathrm{T}}^{\mathrm{Miss}}$ cannot be explained by momentum resolution effects, but rather must come from real invisible particles which have left the detector, however a low value indicates an event in which $E_{\mathrm{T}}^{\mathrm{Miss}}$ may be due entirely to momentum resolution effects, such as may occur in multi-jet events.

However, the observable $E_{\mathrm{T}}^{\mathrm{Miss,Sig}}$ does not take into account the different resolutions of the different objects which make up $E_{\mathrm{T}}^{\mathrm{Miss}}$. A more sophisticated observable, referred to here as the object-based $E_{\mathrm{T}}^{\mathrm{Miss}}$ significance, or $\mathcal{S}$, is also employed by this analysis, and is defined as follows:

$$\mathcal{S}^2 \equiv \left(\mathbf{E}_{\mathrm{T}}^{\mathrm{Miss}}\right)^T \left(\sum_i \mathbf{V}^i\right)^{-1} \left(\mathbf{E}_{\mathrm{T}}^{\mathrm{Miss}}\right) \tag{7.5}$$

where the sub-index i indicates each reconstructed object that enters the $E_{\mathrm{T}}^{\mathrm{Miss}}$ calculation and $\mathbf{V}^i$ is the corresponding covariance matrix.

Studies and comparisons of these two missing transverse energy significance definitions can be found in Reference [97].

7.9 Higgs Tagging

When a Higgs particle of sufficiently low p_{T} decays to two b-quarks, the b-quarks can be reconstructed individually as $R = 0.4$ calorimeter jets. However, if the Higgs particle has sufficiently high p_{T}, the two b-quarks will be too collimated to reconstruct as jets using a radius parameter of $R = 0.4$.

In ATLAS, "Higgs tagging" refers to the techniques used to reconstruct and identify boosted Higgs decays to b-quarks. The "nominal" Higgs tagging method used in ATLAS up until this analysis is illustrated in Figure 7.2. It involves reconstructing the Higgs particle as a trimmed large-R jet with two associated b-tagged $R = 0.2$ track jets, reconstructing the b-hadrons which form from the b-quarks of the Higgs decay.

This technique works well when the b-hadrons resulting from the Higgs decay are too collimated to reconstruct as individual b-tagged $R = 0.4$ calorimeter jets. Simply using

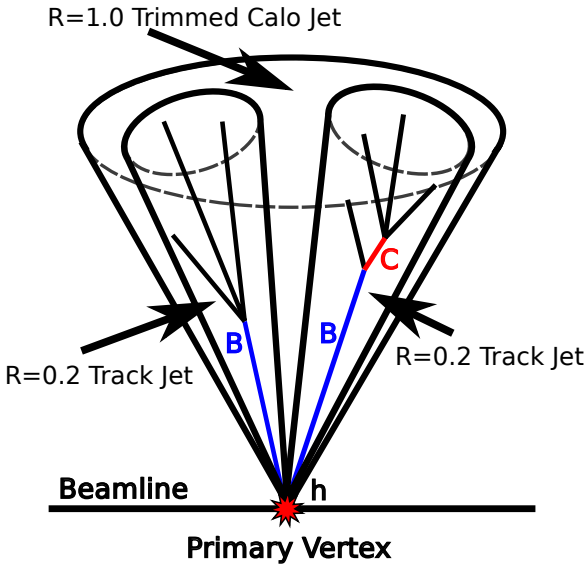

Figure 7.2: A cartoon depicting the nominal boosted Higgs tagging technique employed by ATLAS [5].

b-tagged $R = 0.2$ calorimeter jets has the downside that not all of the decay products of the b-hadrons tend to be captured, so the kinematics of the final reconstructed Higgs particle would suffer. For this reason, trimmed large-R jets are used to reconstruct the Higgs particle itself, while $R = 0.2$ track jets are used to apply b-tagging, which helps, not in reconstructing the Higgs particle's kinematics, but rather in identifying the Higgs particle.

Track jets, being formed from the tracks of charged particles, are not very useful in reconstructing the accurate kinematics of particles, as they will not take into account any decays to neutral particles. However, they are very useful for b-tagging Higgs decays for three main reasons:

- they are more robust against pile-up than calorimeter jets, since it is possible to accurately associate tracks with the primary vertex

- they can reconstruct low p_{T} b-quarks produced in the opposite direction of the boost of the Higgs particle better than calorimeter jets

- they have a better angular resolution with respect to b-quarks than calorimeters jets

However, this method of Higgs tagging has a natural limitation - in a sense, the same limitation that Higgs reconstruction from two $R = 0.4$ calorimeter jets faced. When the Higgs particle becomes boosted enough, its b-hadron decay products will become too collimated to resolve even with $R = 0.2$ track jets. This can be seen in Figure 7.7. In such a case, it may be possible to apply a Higgs tagging technique utilizing $R = 0.1$ track jets, but this too will eventually hit the same limitation, and separating analyses into more and more kinematic regions to apply different Higgs tagging techniques would be difficult to maintain.

Successfully creating a Higgs tagger which can be applied at arbitrarily high boosts will require fundamentally different techniques than the technique described so far. Such techniques are the topic of Reference [5], an ATLAS public note led by the author of this thesis. Section 7.9.1 outlines the findings of the note and describes the variable radius track jet Higgs tagging technique developed for the note. Exclusive-k_{T} (ExKt) and Center-of-Mass (CoM) Higgs tagging techniques were also developed for the note. However, since an existing framework to calibrate track jets was readily available in ATLAS, the variable radius track jet technique was chosen for use in the mono-Higgs analysis. Further information on the ExKt and CoM Higgs tagging techniques can be found in Appendix F.

7.9.1 VR Track Jet Higgs Tagging

As a general and well-understood kinematic trend, the higher the boost of a particle, the more collimated its decay products. This is precisely the origin of the limitations of both $R = 0.4$ calorimeter jet Higgs reconstruction and $R = 0.2$ track jet Higgs tagging. However, this kinematic trend is also the motivation of the variable radius jet clustering algorithm introduced in Section 7.5.5.

Applying the variable radius jet clustering algorithm to Higgs tagging is straightforward - replace the $R = 0.2$ track jets of the nominal technique with VR track jets. This is illustrated pictorially in Figure 7.3, where b-hadrons which are reconstructed by two merging $R = 0.2$ track jets are fully resolved by VR track jets.

In order to study and optimize Higgs tagging with VR track jets, dedicated Higgs jet

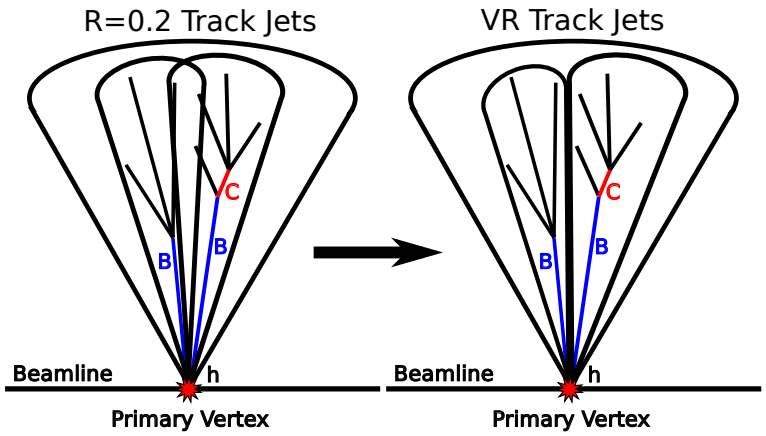

Figure 7.3: A cartoon depicting how using VR track jets instead of $R = 0.2$ track jets can help resolve collimated b-hadrons [5].

Monte Carlo samples were generated. These samples were used to optimize the parameters ρ, R_{max}, and R_{min} by plotting the Higgs jet double subjet b-labelling efficiency as a function of Higgs jet p_{T} with two parameters held constant and the other one varied. Given a Higgs jet, the term "double subjet b-labelling efficiency" refers to the efficiency with which two subjets, each of which is matched to truth b-hadrons, are associated to the Higgs jet. These double subjet b-labelling efficiency plots are shown in Figures 7.4, 7.5, and 7.6 for scans on ρ, R_{min}, and R_{max}, respectively. Values of 30 GeV, 0.02, and 0.4 were chosen for ρ, R_{min}, and R_{max}, respectively.

The double subjet b-labelling performance for the final VR configuration is shown in Figure 7.7, along with the performance for the $R = 0.2$ track jet technique and ExKt and CoM techniques. The plot clearly shows a dramatic decrease in performance for the $R = 0.2$ track jet technique as the Higgs jet p_{T} becomes larger than ~ 1.2 TeV. From kinematic considerations, this is precisely the region where the $R = 0.2$ track jets are expected to merge, and so the loss in double subjet b-labelling performance is directly caused by the inability to reconstruct more than one $R = 0.2$ track jet. However, using the VR algorithm, two resolved track jets can be reconstructed even for 3 TeV Higgs jets.

While double subjet b-labelling performance offers an insightful way to compare the

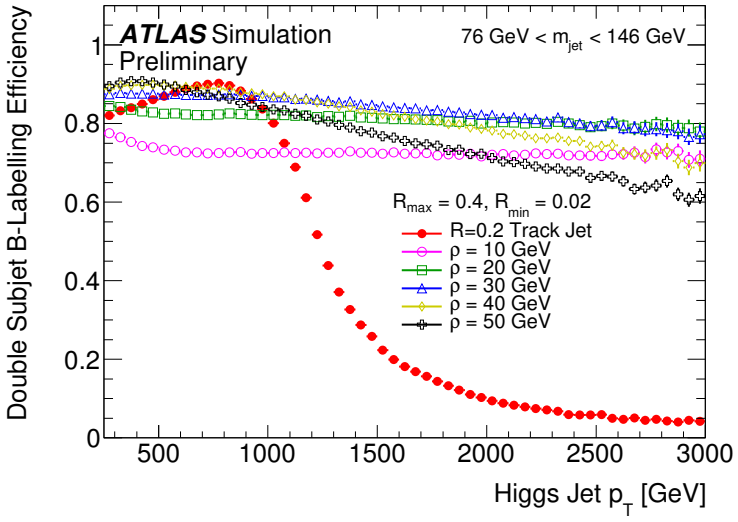

Figure 7.4: A plot showing the efficiency to reconstruct two VR track jets ghost-associated to a Higgs jets and cone-associated to truth b-hadrons as a function of Higgs jet p_{T} and parameter ρ. $\rho = 30$ GeV was chosen as optimal [5].

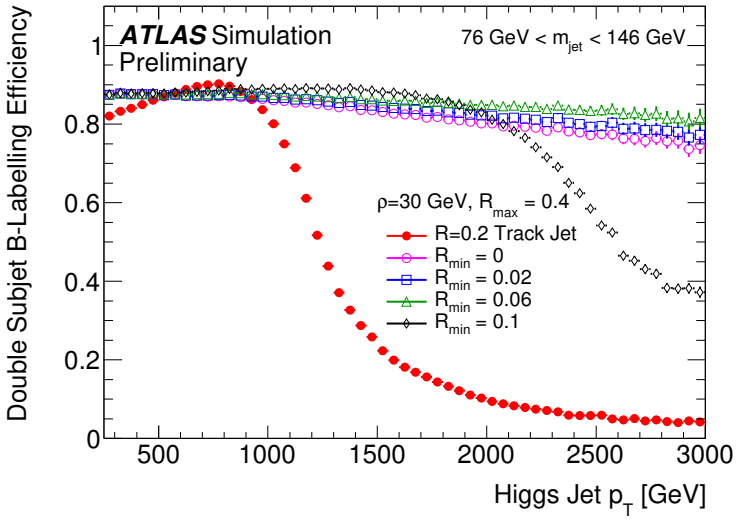

Figure 7.5: A plot showing the efficiency to reconstruct two VR track jets ghost-associated to a Higgs jets and cone-associated to truth b-hadrons as a function of Higgs jet p_{T} and parameter R_{min}. $R_{\mathrm{min}} = 0.02$ was chosen as it is the smallest non-zero value studied [5].

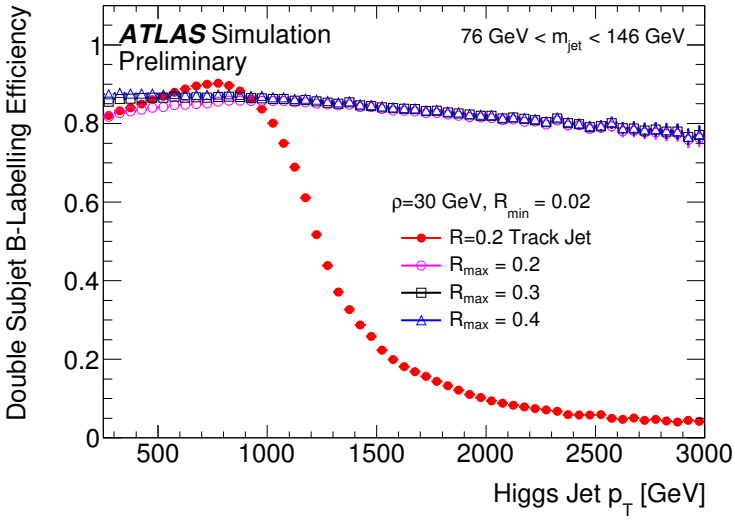

Figure 7.6: A plot showing the efficiency to reconstruct two VR track jets ghost-associated to a Higgs jets and cone-associated to truth b-hadrons as a function of parameter R_{max}. $R_{\text{max}} = 0.4$ was chosen as it provides for the highest performance at low p_{T} [5].

$R = 0.2$ and VR Higgs tagging algorithms, it offers an incomplete picture as it only takes into account the performance of signal jets (Higgs jets). A common way to measure the performance of a tagging algorithm on both signal and background objects simultaneously is to plot a receiver operating characteristic (ROC) curve, which shows some measure of signal efficiency on the x-axis versus some measure of background rejection on the y-axis for different values of a discriminating variable. ROC curves showing the Higgs jet tagging performance versus QCD jet rejection are shown in Figures 7.8 and 7.9, and ROC curves showing the Higgs jet tagging performance vs top jet rejection are shown in Figure 7.10 and 7.11. Both the QCD jets and top jets are taken from Monte Carlo samples, and both of these sets of plots indicate that for Higgs jets with $p_{\text{T}} > 1.5$ TeV, the VR track jet Higgs tagging approach is much more powerful than the $R = 0.2$ track jet approach.

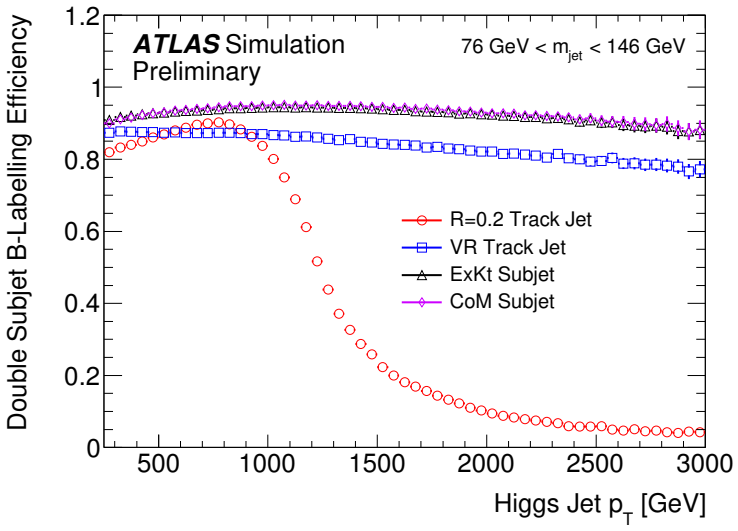

Figure 7.7: A plot of the efficiency of reconstructing two subjets ghost-associated to a Higgs jets and cone-associated to truth b-hadrons using four different subjet techniques: $R = 0.2$ track jets, VR track jets, ExKt calorimeter jets, and CoM calorimeter jets. The plot shows the latter three subjet techniques greatly outperform the $R = 0.2$ track jet technique for high Higgs jet p_{T} [5].

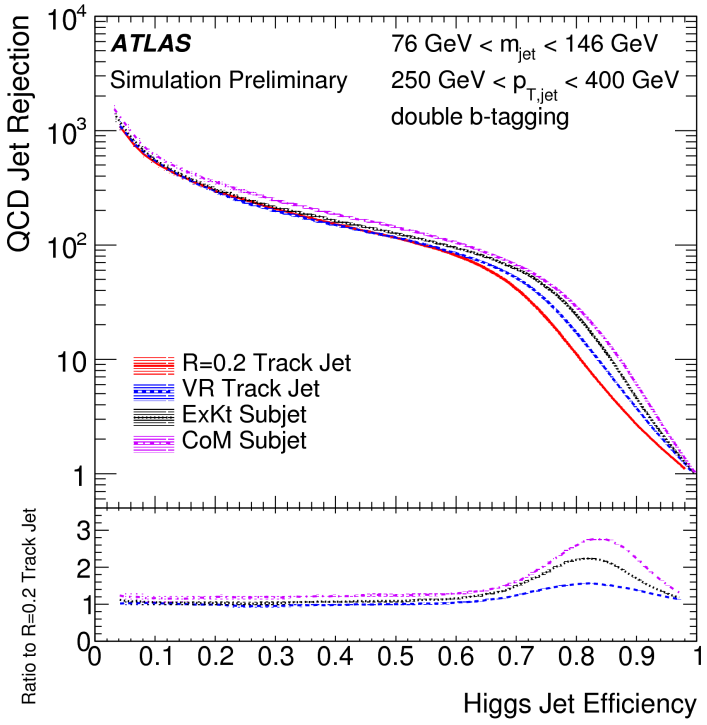

Figure 7.8: ROC curves showing the performance of the VR, $R = 0.2$, and other Higgs tagging techniques when comparing Higgs jets to QCD jet backgrounds for trimmed large-R jets with transverse momenta in the range 250 GeV $< p_{\mathrm{T}} <$ 400 GeV [5].

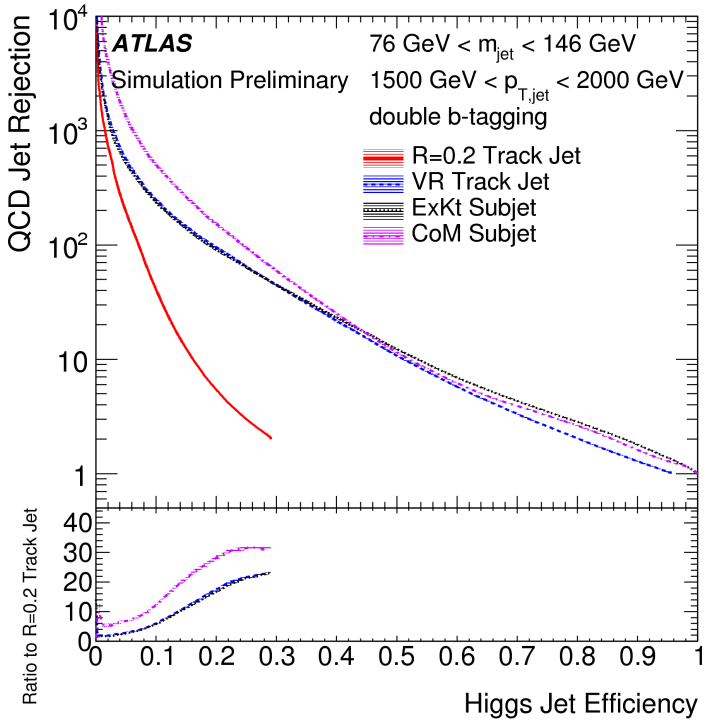

Figure 7.9: ROC curves showing the performance of the VR, $R = 0.2$, and other Higgs tagging techniques when comparing Higgs jets to QCD jet backgrounds for trimmed large-R jets with transverse momenta in the range 1500 GeV $< p_{\mathrm{T}} <$ 2000 GeV [5].

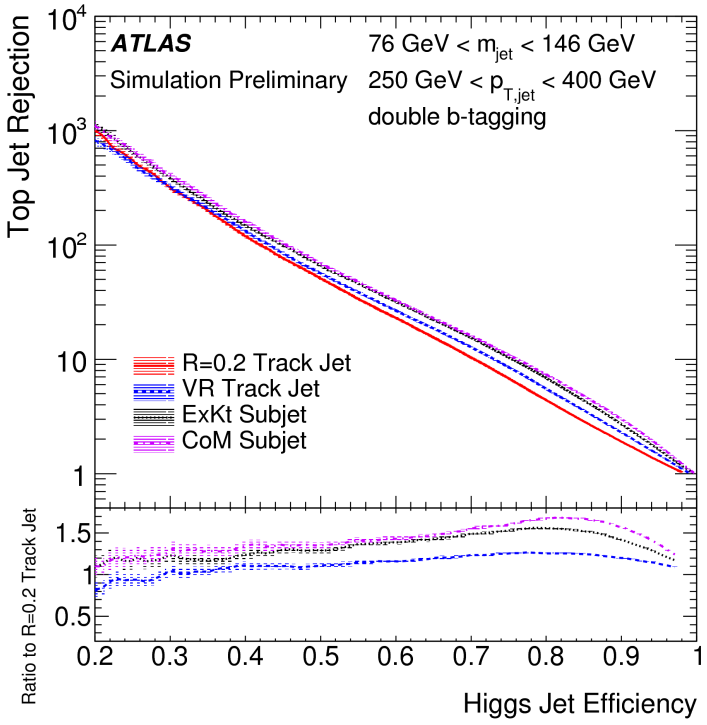

Figure 7.10: ROC curves showing the performance of the VR, $R = 0.2$, and other Higgs tagging techniques when comparing to top jet backgrounds for Higgs jets with transverse momenta in the range 250 GeV $< p_{\mathrm{T}} <$ 400 GeV [5].

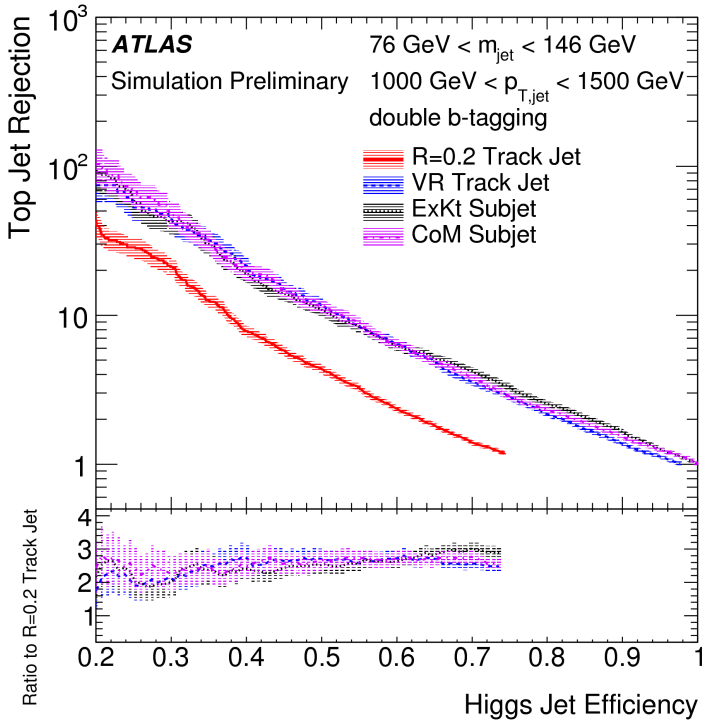

Figure 7.11: ROC curves showing the performance of the VR, $R = 0.2$, and other Higgs tagging techniques when comparing to top jet backgrounds for Higgs jets with transverse momenta in the range 1500 GeV $< p_{\mathrm{T}} <$ 2000 GeV [5].

Chapter 8

EVENT SELECTION

This analysis implements an event selection which vetoes leptons and tries to reconstruct a Higgs boson candidate with a mass near the experimentally measured value of 125 GeV back-to-back with $E_{\mathrm{T}}^{\mathrm{Miss}}$ to search for the Dark Matter signal process. The region created by this event selection is referred to as the 0-lepton Signal Region.

In addition, a 1-lepton Control Region (consisting of a μ^+ Control Region and a μ^- Control Region), and a 2-lepton Control Region (consisting of a 2-electron Control Region and a 2-muon Control Region) are defined to aid in the Standard Model background estimation, described in more detail in Chapter 9. The event selections of the control regions are chosen to be as similar as possible to the signal region. Along these lines, the 1-lepton Control Regions use $E_{\mathrm{T}}^{\mathrm{Miss,\ no\ }\mu}$ (defined as $E_{\mathrm{T}}^{\mathrm{Miss}}$ calculated without taking into account muons), and the 2-lepton Control Regions use $p_{\mathrm{T}}^{l\bar{l}}$ as proxies of $E_{\mathrm{T}}^{\mathrm{Miss}}$ in the 0-lepton Signal Region.

All analysis regions are binned in $E_{\mathrm{T}}^{\mathrm{Miss}}$, $E_{\mathrm{T}}^{\mathrm{Miss,\ no\ }\mu}$, or $p_{\mathrm{T}}^{l\bar{l}}$ and all analysis regions are binned in the number of b-tagged small-R jets for the Resolved Channel or b-tagged VR track jets for the Merged Channel. All analysis regions are defined by orthogonal event selections, and all regions are used to perform a final binned maximum likelihood fit of background and signal Monte Carlo simulation to data, with the exception that the 2-electron and 2-muon Control Regions are combined before being used in the fit. This fit is described in more detail in Section 11.1.

This chapter is organized as follows. Section 8.1 describes the triggers used. Section 8.2 describes the base event selection applied to all regions that ensures that only quality proton-proton collision events are considered. Sections 8.3.1 and 8.3.2 then present the details of the 0-lepton Signal Region event selections in the Resolved Channel and Merged Channel, respectively, and finally Section 8.4 presents the details of the 1-lepton and 2-lepton Control

Region event selections.

8.1 Trigger

The Signal Region and 1-lepton Control Region utilizes $E_{\mathrm{T}}^{\mathrm{Miss}}$ triggers while the 2-lepton Control Region utilizes single lepton triggers. The threshold for the $E_{\mathrm{T}}^{\mathrm{Miss}}$ triggers ranges from 70 GeV to 110 GeV, depending on the data collection period. The online $E_{\mathrm{T}}^{\mathrm{Miss}}$ value is calculated using only calorimeter information, and thus differs from the full offline $E_{\mathrm{T}}^{\mathrm{Miss}}$ calculation. In order to maximize sensitivity of low-boost signal samples in the lowest $E_{\mathrm{T}}^{\mathrm{Miss}}$ bin of the analysis, the offline $E_{\mathrm{T}}^{\mathrm{Miss}}$ cut value is chosen to be in a region where the $E_{\mathrm{T}}^{\mathrm{Miss}}$ trigger is not fully efficient. For this reason, it was necessary to derive a $E_{\mathrm{T}}^{\mathrm{Miss}}$ trigger calibration to handle mis-modelling of the $E_{\mathrm{T}}^{\mathrm{Miss}}$ trigger response in MC simulation. This was done using the 1-lepton Control Region by measuring the trigger efficiencies in both MC simulation and data and deriving scale factors to correct the trigger response in MC simulation in the 0-lepton Signal Region. The efficiency of the $E_{\mathrm{T}}^{\mathrm{Miss}}$ trigger for an offline $E_{\mathrm{T}}^{\mathrm{Miss}}$ value of 150 GeV ranges from 75% to 90%, depending on the specific $E_{\mathrm{T}}^{\mathrm{Miss}}$ trigger and the data taking period. All $E_{\mathrm{T}}^{\mathrm{Miss}}$ triggers are fully efficient for offline $E_{\mathrm{T}}^{\mathrm{Miss}}$ values above 200 GeV. A full list of the triggers used in each region is shown Appendix G.

8.2 Pre-selection

The event selections which are common to all analysis regions are summarized in Table 8.1.

Events from data are required to be from runs in the Good Run List, described in Section 5.1, to ensure that quality data is used in the analysis. The number of primary vertices, as defined in Section 7.2, is required to be ≥ 1, ensuring a basic requirement that a hard-scatter event has occurred and has been identified. A veto on poorly reconstructed jets, as defined in Reference [98], is made. This selection is implemented because events with poorly reconstructed jets tend to have poorly reconstructed $E_{\mathrm{T}}^{\mathrm{Miss}}$ as a result, and good $E_{\mathrm{T}}^{\mathrm{Miss}}$ measurements are crucial to this analysis. In particular, if jets in the multi-jet background are poorly reconstructed, leading to a large $E_{\mathrm{T}}^{\mathrm{Miss}}$, these events could contaminate the Signal Region. The $E_{\mathrm{T}}^{\mathrm{Miss}}$ of each event is required to be larger than 150 GeV, since the Dark Matter particles in our signal will result in a large $E_{\mathrm{T}}^{\mathrm{Miss}}$.

Table 8.1: The pre-selection criteria for events in all analysis channels and regions.

Pre-selection	
Event Selection	Purpose
data $\in$ GRL	good event quality
$N_{PV} \geq 1$	good event quality
LooseBadJet veto	reject multi-jet, mis-measured $E_{\mathrm{T}}^{\mathrm{Miss}}$
$E_{\mathrm{T}}^{\mathrm{Miss}} > 150$ GeV	signal-like events
$\Delta\phi(E_{\mathrm{T}}^{\mathrm{Miss}}, j_{cf3}) > 20°$	reject multi-jet
$\Delta\phi(E_{\mathrm{T}}^{\mathrm{Miss}}, p_{\mathrm{T}}^{\mathrm{Miss}}) < 90°$	reject multi-jet

The last two selections in Table 8.1 are collectively referred to as "anti-QCD" cuts. Multi-jet events with poorly reconstructed jets tend to obtain a $E_{\mathrm{T}}^{\mathrm{Miss}}$ close to the axis of the poorly reconstructed jet. For this reason, a cut requiring the leading three jets in the central-forward jet collection to be well separated from the $E_{\mathrm{T}}^{\mathrm{Miss}}$ in an event is made: $\Delta\phi(E_{\mathrm{T}}^{\mathrm{Miss}}, j_{cf3}) > 20°$. Multi-jet events with poor $E_{\mathrm{T}}^{\mathrm{Miss}}$ reconstruction are further suppressed by requiring the $\Delta\phi$ separation between $E_{\mathrm{T}}^{\mathrm{Miss}}$ and $p_{\mathrm{T}}^{\mathrm{Miss}}$ to be $< 90°$.

8.3 0-Lepton Signal Region

The 0-lepton Signal Region event selections are described in Sections 8.3.1 and 8.3.2 for the Resolved and Merged Channels, respectively. Events with $E_{\mathrm{T}}^{\mathrm{Miss}} < 500$ GeV are considered for the Resolved Channel, and such events employ the resolved Higgs reconstruction approach. Events with $E_{\mathrm{T}}^{\mathrm{Miss}} > 500$ GeV are considered for the Merged Channel, where the VR track jet boosted Higgs tagging technique is employed for Higgs reconstruction. The cut-off value of 500 GeV was determined by a previous analysis iteration where it was found that the signal sensitivity of the Resolved and Merged channel converged at 500 GeV [7].

In terms of the $Z'-$2HDM model, this conceptually means $Z'-$2HDM signals with higher $m_{Z'}$, which produce more boosted back-to-back Higgs bosons and DM particles, are dominantly selected by the Merged Channel, while low $m_{Z'}$ signals are dominantly selected by

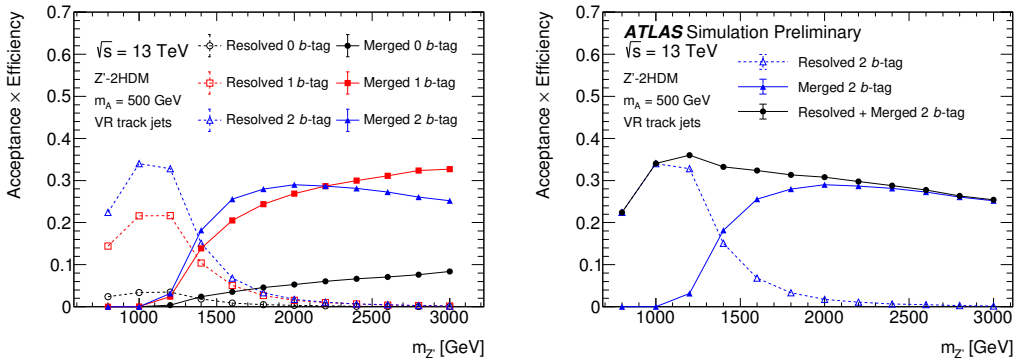

Figure 8.1: Signal acceptance × efficiency as a function of $m_{Z'}$ for a fixed value of m_A = 500 GeV [2].

the Resolved Channel. This is confirmed by Figure 8.1 which plots the signal acceptance times efficiency in the 0-lepton Signal Region after all Resolved or Merged channel cuts are applied, as a function of $m_{Z'}$ for a fixed m_A of 500 GeV.

8.3.1 Resolved 0-Lepton Signal Region

The Resolved Channel 0-lepton Signal Region event selection used for the combined fit is shown in Table 8.2.

After the trigger selection and the pre-selection, vetoes on `VHLoose` electrons and `VHLoose` muons remove events which produce electrons and muons, effectively making negligible many basic SM processes, such as Drell-Yan and $Z(l\bar{l})+$jets, but also reducing backgrounds such as leptonic $W+$jets, single top, and leptonic and semi-leptonic $t\bar{t}$, which are not negligible even after all selections are made.

The object-based $E_{\mathrm{T}}^{\mathrm{Miss}}$ significance, $\mathcal{S}$, is required to be > 16, reducing the multi-jet background. The $E_{\mathrm{T}}^{\mathrm{Miss}}$ is required to be below 500 GeV to ensure that signal events have low enough $E_{\mathrm{T}}^{\mathrm{Miss}}$ and Higgs boosts that the Higgs boson can be reconstructed using the resolved Higgs reconstruction technique. The number of central small-R jets is required to be ≥ 2 to ensure a Higgs candidate can be reconstructed.

Selections on the leading central jet p_{T} and on the sum of the first two or three jets in

Table 8.2: The event selection for the Resolved Channel in the 0-lepton Signal Region used for the combined fit.

Resolved 0L SR (Fit) Event Selections	
Event Selection	Purpose
Trigger	select large $E_{\mathrm{T}}^{\mathrm{Miss}}$
Pre-selection	good event quality, reject multi-jet
`VHLoose` electron veto	reject $Z+\mathrm{jets}$, $W+\mathrm{jets}$, $t\bar{t}$ etc
`VHLoose` muon veto	reject $Z+\mathrm{jets}$, $W+\mathrm{jets}$, $t\bar{t}$ etc
$\mathcal{S} > 16$	reject multi-jet
$E_{\mathrm{T}}^{\mathrm{Miss}} < 500$ GeV	allow resolved Higgs reconstructed
$p_{\mathrm{T}}^{\mathrm{Miss}} > 30$ GeV if < 2 b-tagged small-R jets	remove non-collision background
$N_{j_c} \geq 2$	allow resolved Higgs reconstructed
$p_T^{j_{c,1}} > 45$ GeV	remove mis-modelling
$\sum_{j_{cf2}} p_{\mathrm{T}} \geq 120$ GeV or $\sum_{j_{cf3}} p_{\mathrm{T}} \geq 150$ GeV	remove mis-modelling
$\Delta\phi(j_{c,1}, j_{c,2}) < 140^\circ$	reject multi-jet
$\Delta R(j_{c,1}, j_{c,2}) < 1.8$	reject multi-jet
$\Delta\phi(E_{\mathrm{T}}^{\mathrm{Miss}}, h_{\mathrm{cand}}) > 120^\circ$	multi-jet
b-tagged small-R jet veto	reject $t\bar{t}$
τ veto	reject $W+\mathrm{jets}$, $t\bar{t}$
extended τ veto	reject $W+\mathrm{jets}$, $t\bar{t}$
$H_{\mathrm{T}}^{\mathrm{Resolved}} \leq 0.37$	reject $t\bar{t}$, high jet multiplicity
50 GeV $< m_{h_{\mathrm{cand}}} <$ 280 GeV	loose mass window around Higgs mass

the central-forward jet collection are designed to remove a region which is mis-modelled in simulation due to a non-trivial dependence of the trigger efficiency on the jet activity, and is inherited from the LHC Run 1 SM $Vh(b\bar{b})$ analysis [99].

The $\Delta\phi$ and ΔR of the two leading central jets are required to be $< 140°$ and < 1.8, respectively. These selections aim to remove multi-jet events, as jets from multi-jet events are often back-to-back, while the jets resulting from the Higgs decay in signal events tend to be close-by. The $\Delta\phi$ between the Higgs candidate and $E_{\mathrm{T}}^{\mathrm{Miss}}$ is required to be $> 120°$, a selection which also aims to remove multi-jet events as the $E_{\mathrm{T}}^{\mathrm{Miss}}$ in multi-jet events is not expected to be back-to-back with di-jet systems.

A veto is made on b-tagged small-R jets which are not the leading two b-tagged small-R jets. This selection aims to remove $t\bar{t}$, particularly hadronic $t\bar{t}$, events which may contain more than two b-tagged jets due to the high jet multiplicity and the potential to mis-tag one of the jets not originating from a b-quark.

Events with tau and extended tau particles are vetoed, removing leptonic $t\bar{t}$ events, semi-leptonic $t\bar{t}$ events, and W + jets events where the W bosons decay to tau leptons.

The $H_{\mathrm{T}}^{\mathrm{Resolved}}$ selection removes events where a significant portion of jet activity is contained in small-R jets beyond the leading three small-R jets. $H_{\mathrm{T}}^{\mathrm{Resolved}}$ is defined as follows:

$$H_{\mathrm{T}}^{\mathrm{Resolved}} = \frac{\sum_{i=4}^{N_j} p_{\mathrm{T}}^{j_i}}{\sum_{i=1}^{N_j} p_{\mathrm{T}}^{j_i}} \tag{8.1}$$

and is required to be ≤ 0.37. This selection targets $t\bar{t}$ events which have large jet multiplicities.

Finally, a Higgs mass window cut of 50 GeV $< m_{h_{\mathrm{cand}}} <$ 280 GeV is applied to reject backgrounds which do not create Higgs bosons. After this selection, the remaining selected events are binned according to their $E_{\mathrm{T}}^{\mathrm{Miss}}$ and according to the number of b-tagged jets in the j_{cf3} set. The $E_{\mathrm{T}}^{\mathrm{Miss}}$ bins are 150 GeV $< E_{\mathrm{T}}^{\mathrm{Miss}} <$ 200 GeV, 200 GeV $< E_{\mathrm{T}}^{\mathrm{Miss}} <$ 350 GeV, and 350 GeV $< E_{\mathrm{T}}^{\mathrm{Miss}} <$ 500 GeV. The b-tag bins are 0, 1, and 2. The Higgs candidate mass spectra in the 2 b-tag bin and all $E_{\mathrm{T}}^{\mathrm{Miss}}$ bins then make up the final inputs for the combined fit, with mass bins either 5 or 10 GeV wide, giving either 46 or 23 total mass bins

Table 8.3: The event selection for the Resolved Channel in the 0-lepton Signal Region used to measure the final event yield.

Resolved 0L SR (Final) Event Selections	
Event Selection	Purpose
Trigger	select large $E_{\mathrm{T}}^{\mathrm{Miss}}$
Pre-selection	good event quality, reject multi-jet
Resolved 0L SR (Fit) Event Selections	
70 GeV $< m_{h_{\mathrm{cand}}} <$ 140 GeV	tight Higgs mass window to reject backgrounds

between 50 and 280 GeV, depending on the $E_{\mathrm{T}}^{\mathrm{Miss}}$ bin.

After the fit is performed, a final, tight, Higgs candidate mass window cut of 70 GeV $< m_{h_{\mathrm{cand}}} <$ 140 GeV is applied. The final yield after this cut is applied is used to determine the signal strength of the $Z'-$2HDM model and to set limits on the model parameter space. The full event selection for the Resolved Channel, 0-lepton Signal Region, after this "final" cut is summarized in Table 8.3.

8.3.2 Merged 0-Lepton Signal Region

The Merged Channel 0-lepton Signal Region event selection used for the combined fit is shown in Table 8.2.

After the trigger selection and pre-selection, the same electron and muon vetoes applied in the Resolved Channel are applied here to reduce the same backgrounds. $E_{\mathrm{T}}^{\mathrm{Miss}}$ is required to be above 500 GeV to ensure that signal events contain Higgs bosons which are boosted enough to warrant the use of the dedicated boosted Higgs tagging using VR track jets described in Section 7.9.1. Similarly, at least 1 trimmed large-R jet is required in order to apply the Higgs tagging technique, and the leading trimmed large-R jet is required to have at least two ghost associated VR track jets. The two leading VR track jets ghost associated to the leading trimmed large-R jet (VR_1 and VR_2) are required to have a ΔR separation greater than the R_{min} value used for the VR clustering, to ensure that the jets are not

Table 8.4: The event selection for the Merged Channel in the 0-lepton Signal Region used for the combined fit.

Merged 0L SR (Fit) Event Selections	
Event Selection	Purpose
Trigger	select large $E_{\mathrm{T}}^{\mathrm{Miss}}$
Pre-selection	good event quality, reject multi-jet
`VHLoose` electron veto	reject $Z+\mathrm{jets}$, $W+\mathrm{jets}$, $t\bar{t}$ etc
`VHLoose` muon veto	reject $Z+\mathrm{jets}$, $W+\mathrm{jets}$, $t\bar{t}$ etc
$E_{\mathrm{T}}^{\mathrm{Miss}} > 500$ GeV	allow merged Higgs reconstruction
$p_{\mathrm{T}}^{\mathrm{Miss}} > 30$ GeV if < 2 b-tagged VR track jets	remove non-collision background
$N_{J_c} \geq 1$	allow merged Higgs reconstruction
$N_{\text{GA VR track jets}}^{\text{leading } J} \geq 2$	allow merged Higgs reconstruction
$\frac{\Delta R(\mathrm{VR}_1,\mathrm{VR}_2)}{R_{\mathrm{min}}} > 1$	remove concentric VR track jets
non-associated b-tagged VR track jet veto	reject $t\bar{t}$
non-associated τ veto	reject $W+\mathrm{jets}$, $t\bar{t}$
non-associated extended τ veto	reject $W+\mathrm{jets}$, $t\bar{t}$
$H_{\mathrm{T}}^{\mathrm{Merged}} \leq 0.57$	reject $t\bar{t}$, high jet multiplicity
50 GeV $< m_{h_{\mathrm{cand}}} <$ 270 GeV	loose mass window around Higgs mass

concentric to be consistent with the what was done for the VR b-tagging calibration.

To reject $t\bar{t}$ events and W + jets events, taus, extended taus, and b-tagged VR track jets which are not associated with the leading trimmed large-R jet are vetoed. In order to reduce $t\bar{t}$ further, an $H_{\mathrm{T}}^{\mathrm{Merged}}$ selection is implemented along the lines of the $H_{\mathrm{T}}^{\mathrm{Resolved}}$ selection. $H_{\mathrm{T}}^{\mathrm{Merged}}$ is defined as follows:

$$H_{\mathrm{T}}^{\mathrm{Merged}} = \frac{\sum_{i=1}^{N_j} p_{\mathrm{T}}^{j_i \text{ outside } J_1}}{\sum_{i=1}^{N_j} p_{\mathrm{T}}^{j_i \text{ outside } J_1} + p_{\mathrm{T}}^{J_1}} \tag{8.2}$$

and is required to be ≤ 0.57. The selection essentially rejects events where a significant portion of jet activity is contained in small-R jets outside the $R = 1.0$ cone of the leading trimmed large-R jet.

Finally, as was the case for the Resolved Channel event selection, a loose Higgs mass window cut is performed. In the Merged Channel, this selection requires Higgs candidates to have a mass of 50 GeV $< m_{h_{\mathrm{cand}}} <$ 270 GeV. The choice to go up to 270 GeV in the Merged Channel, but 280 GeV in the Resolved Channel, was just to allow the mass bin widths for the final fit in the Merged Channel to be 20 GeV, giving each bin higher statistics than if 10 GeV or 5 GeV were chosen, as they were for the Resolved Channel. After this loose Higgs mass window cut, remaining events are binned according to the number of b-tagged VR track jets ghost associated to the leading trimmed large-R jet. The b-tag bins are 0, 1, and 2. The Higgs candidate mass spectra in the 2 b-tag bin then make up the final inputs for the combined fit, with mass bins 20 GeV wide giving 12 total mass bins between 50 and 270 GeV.

As in the Resolved Channel case, after the fit is performed, a final, tight, Higgs candidate mass window cut of 70 GeV $< m_{h_{\mathrm{cand}}} <$ 140 GeV is applied. The final yield after this cut is applied is used to determine the signal strength of the $Z'-$2HDM model and to set limits on the model parameter space. The full event selection for the Merged Channel, 0-lepton Signal Region, after this "final" cut is summarized in Table 8.5.

Table 8.5: The event selection for the Merged Channel in the 0-lepton Signal Region used for the combined fit.

Merged 0L SR (Final) Event Selections	
Event Selection	Purpose
Trigger	select large $E_{\mathrm{T}}^{\mathrm{Miss}}$
Pre-selection	good event quality, reject multi-jet
Merged 0L SR (Fit) Event Selections	
70 GeV $< m_{h_{\mathrm{cand}}} <$ 140 GeV	tight Higgs mass window to reject backgrounds

8.4 1-Lepton and 2-Lepton Control Regions

The 1-lepton Control Region event selections for the Resolved and Merged Channels are shown in Tables 8.6 and 8.7, respectively, while the 2-lepton Control Region event selections for the Resolved and Merged Channels are shown in Tables 8.8 and 8.9, respectively. The 1-lepton Control Region requires exactly 1 `WHSignal` muon, but vetoes additional `VHLoose` muons, while the 2-lepton Control Region selects either exactly two `ZHSignal` electrons or exactly two opposite sign `ZHSignal` muons. The 2-lepton Control Region further requires that the selected di-lepton system have a mass in the range 83 GeV $< m_{e\bar{e}} <$ 99 GeV for electrons or 71 GeV $< m_{\mu\bar{\mu}} <$ 106 GeV for muons. In the 1-lepton Control Region, events are binned in $E_{\mathrm{T}}^{\mathrm{Miss,\ no\ }\mu}$ instead of $E_{\mathrm{T}}^{\mathrm{Miss}}$, and in the 2-lepton Control Region, events are binned in $p_{\mathrm{T}}^{l\bar{l}}$ instead of $E_{\mathrm{T}}^{\mathrm{Miss}}$. The object-based $E_{\mathrm{T}}^{\mathrm{Miss}}$ significance ($\mathcal{S}$) cut is not applied in the Control Regions, however a cut on the $E_{\mathrm{T}}^{\mathrm{Miss}}$ significance of $< 3.5\sqrt{\mathrm{GeV}}$ is applied in the 2-lepton Control Region for the Resolved Channel.

Events selected after the 1-lepton Control Region Resolved Channel event selection described here are binned in three bins of $E_{\mathrm{T}}^{\mathrm{Miss,\ no\ }\mu}$, are binned according to the number of b-tagged small-R jets present, and are binned by the charge of the selected muon. The $E_{\mathrm{T}}^{\mathrm{Miss,\ no\ }\mu}$ bins are 150 GeV $< E_{\mathrm{T}}^{\mathrm{Miss,\ no\ }\mu} <$ 200 GeV, 200 GeV $< E_{\mathrm{T}}^{\mathrm{Miss,\ no\ }\mu} <$ 350 GeV, and 350 GeV $< E_{\mathrm{T}}^{\mathrm{Miss,\ no\ }\mu} <$ 500 GeV. The b-tag bins are 0, 1, and 2. Only the 2 b-tag

Table 8.6: The event selection for the Resolved Channel in the 1-lepton Control Region used for the combined fit.

Resolved 1L SR (Fit) Event Selections	
Event Selection	Purpose
Trigger	select events with muons
Pre-selection	good event quality, reject multi-jet
exactly one `WHSignal` muon	select W + jets and $t\bar{t}$ events
`VHLoose` electron veto	want only one lepton
veto on additional `VHLoose` muons	want only one lepton
$E_{\mathrm{T}}^{\mathrm{Miss,\ no\ }\mu} < 500$ GeV	allow resolved Higgs reconstructed
$p_{\mathrm{T}}^{\mathrm{Miss}} > 30$ GeV if < 2 b-tagged small-R jets	remove non-collision background
$N_{j_c} \geq 2$	allow resolved Higgs reconstructed
$p_T^{j_{c,1}} > 45$ GeV	remove mis-modelling
$\sum_{j_{cf2}} p_{\mathrm{T}} \geq 120$ GeV or $\sum_{j_{cf3}} p_{\mathrm{T}} \geq 150$ GeV	remove mis-modelling
$\Delta\phi(j_{c,1}, j_{c,2}) < 140°$	reject multi-jet
$\Delta R(j_{c,1}, j_{c,2}) < 1.8$	reject multi-jet
$\Delta\phi(E_{\mathrm{T}}^{\mathrm{Miss}}, h_{\mathrm{cand}}) > 120°$	multi-jet
b-tagged small-R jet veto	reject $t\bar{t}$
τ veto	reject W + jets, $t\bar{t}$
extended τ veto	reject W + jets, $t\bar{t}$
$H_{\mathrm{T}}^{\mathrm{Resolved}} \leq 0.37$	reject $t\bar{t}$, high jet multiplicity
50 GeV $< m_{h_{\mathrm{cand}}} <$ 280 GeV	loose mass window around Higgs mass

Table 8.7: The event selection for the Merged Channel in the 1-lepton Control Region used for the combined fit.

Merged 1L SR (Fit) Event Selections	
Event Selection	Purpose
Trigger	select events with muons
Pre-selection	good event quality, reject multi-jet
exactly one `WHSignal` muon	select W + jets and $t\bar{t}$ events
`VHLoose` electron veto	want only one lepton
veto on additional `VHLoose` muons	want only one lepton
$E_{\mathrm{T}}^{\mathrm{Miss,\ no\ }\mu} > 500$ GeV	allow merged Higgs reconstruction
$p_{\mathrm{T}}^{\mathrm{Miss}} > 30$ GeV if < 2 b-tagged VR track jets	remove non-collision background
$N_{J_c} \geq 1$	allow merged Higgs reconstruction
$N_{\mathrm{GA\ VR\ track\ jets}}^{\mathrm{leading}\ J} \geq 2$	allow merged Higgs reconstruction
$\frac{\Delta R(\text{leading VR track jet,sub-leading VR track jet})}{R_{\mathrm{min}}} > 1$	remove concentric VR track jets
non-associated b-tagged VR track jet veto	reject $t\bar{t}$
non-associated τ veto	reject W + jets, $t\bar{t}$
non-associated extended τ veto	reject W + jets, $t\bar{t}$
$H_{\mathrm{T}}^{\mathrm{Merged}} \leq 0.57$	reject $t\bar{t}$, high jet multiplicity
50 GeV $< m_{h_{\mathrm{cand}}} <$ 270 GeV	loose mass window around Higgs mass

Table 8.8: The event selection for the Resolved Channel in the 2-lepton Control Region used for the combined fit.

Resolved 2L SR (Fit) Event Selections	
Event Selection	Purpose
Trigger	select events with muons
Pre-selection	good event quality, reject multi-jet
exactly two `ZHSignal` electrons OR opposite sign `ZHSignal` muons	select $Z+$ jets events
83 GeV $< m_{e\bar{e}} <$ 99 GeV OR 71 GeV $< m_{\mu\bar{\mu}} <$ 106 GeV	reject $t\bar{t}$, multi-jet, etc
veto on additional `VHLoose` electrons	want only two leptons
veto on additional `VHLoose` muons	want only two leptons
$E_{\mathrm{T}}^{\mathrm{Miss,\ Sig}} < 3.5\sqrt{\mathrm{GeV}}$	reject $t\bar{t}$, single top
$p_{\mathrm{T}}^{l\bar{l}} < 500$ GeV	allow resolved Higgs reconstructed
$p_{\mathrm{T}}^{\mathrm{Miss}} > 30$ GeV if < 2 b-tagged small-R jets	remove non-collision background
$N_{j_c} \geq 2$	allow resolved Higgs reconstructed
$p_T^{j_{c,1}} > 45$ GeV	remove mis-modelling
$\sum_{j_c f2} p_{\mathrm{T}} \geq 120$ GeV or $\sum_{j_c f3} p_{\mathrm{T}} \geq 150$ GeV	remove mis-modelling
$\Delta\phi(j_{c,1}, j_{c,2}) < 140°$	reject multi-jet
$\Delta R(j_{c,1}, j_{c,2}) < 1.8$	reject multi-jet
$\Delta\phi(E_{\mathrm{T}}^{\mathrm{Miss}}, h_{\mathrm{cand}}) > 120°$	multi-jet
b-tagged small-R jet veto	reject $t\bar{t}$
τ veto	reject $W+$ jets, $t\bar{t}$
extended τ veto	reject $W+$ jets, $t\bar{t}$
$H_{\mathrm{T}}^{\mathrm{Resolved}} \leq 0.37$	reject $t\bar{t}$, high jet multiplicity
50 GeV $< m_{h_{\mathrm{cand}}} <$ 280 GeV	loose mass window around Higgs mass

Table 8.9: The event selection for the Merged Channel in the 2-lepton Control Region used for the combined fit.

Merged 2L SR (Fit) Event Selections	
Event Selection	Purpose
Trigger	select events with muons
Pre-selection	good event quality, reject multi-jet
exactly two `ZHSignal` electrons OR opposite sign `ZHSignal` muons	select $Z+$ jets events
83 GeV $< m_{e\bar{e}} <$ 99 GeV OR 71 GeV $< m_{\mu\bar{\mu}} <$ 106 GeV	reject $t\bar{t}$, multi-jet, etc
veto on additional `VHLoose` electrons	want only two leptons
veto on additional `VHLoose` muons	want only two leptons
$E_{\mathrm{T}}^{\mathrm{Miss,\ Sig}} < 3.5\sqrt{\mathrm{GeV}}$	reject $t\bar{t}$, single top
$p_{\mathrm{T}}^{l\bar{l}} > 500$ GeV	allow merged Higgs reconstruction
$p_{\mathrm{T}}^{\mathrm{Miss}} > 30$ GeV if < 2 b-tagged VR track jets	remove non-collision background
$N_{J_c} \geq 1$	allow merged Higgs reconstruction
$N_{\mathrm{GA\ VR\ track\ jets}}^{\mathrm{leading}\ J} \geq 2$	allow merged Higgs reconstruction
$\frac{\Delta R(\text{leading VR track jet,sub-leading VR track jet})}{R_{\mathrm{min}}} > 1$	remove concentric VR track jets
non-associated b-tagged VR track jet veto	reject $t\bar{t}$
non-associated τ veto	reject $W+$ jets, $t\bar{t}$
non-associated extended τ veto	reject $W+$ jets, $t\bar{t}$
$H_{\mathrm{T}}^{\mathrm{Merged}} \leq 0.57$	reject $t\bar{t}$, high jet multiplicity
50 GeV $< m_{h_{\mathrm{cand}}} <$ 270 GeV	loose mass window around Higgs mass

bin was used for the fit, while the 0 and 1 b-tag bins were used for internal consistency and cross-check studies. The Events selected after the 1-lepton Control Region Merged Channel event selection described here are binned in three bins of b-tagged VR track jets ghost associated to the leading large-R jet and are binned by the charge of the selected muon. As is the case with the binning in the Resolved Channel, the b-tag bins are 0, 1, and 2, and only the 2 b-tag bin was used for the fit, while the 0 and 1 b-tag bins were used for internal consistency and cross-check studies.

Events selected after the 2-lepton Control Region Resolved Channel event selection described here are binned in three bins of $p_{\mathrm{T}}^{l\bar{l}}$ and are binned according to the number of b-tagged small-R jets present. The $p_{\mathrm{T}}^{l\bar{l}}$ bins are 150 GeV $< p_{\mathrm{T}}^{l\bar{l}} <$ 200 GeV, 200 GeV $< p_{\mathrm{T}}^{l\bar{l}} <$ 350 GeV, and 350 GeV $< p_{\mathrm{T}}^{l\bar{l}} <$ 500 GeV. The b-tag bins are 0, 1, and 2, and only the 2 b-tag bin was used for the fit, while the 0 and 1 b-tag bins were used for internal consistency and cross-check studies. Events passing the Merged Channel 2-lepton Control Region event selection are binned in the number of b-tagged VR track jets ghost associated to the leading large-R jet. As is the case with the binning in the Resolved Channel, the b-tag bins are 0, 1, and 2, and only the 2 b-tag bin was used for the fit, while the 0 and 1 b-tag bins were used for internal consistency and cross-check studies. A summary of the bins used to perform the full fit is presented in Table 8.10.

Table 8.10: Event categories used in the fit.

	0 lepton	**1 muon**	**2 leptons**
Region	SR	$t\bar{t}$ and W + jets CR	Z + jets CR
$E_{\mathrm{T}}^{\mathrm{Miss}}$ or $E_{\mathrm{T}}^{\mathrm{Miss}}$ proxy	$E_{\mathrm{T}}^{\mathrm{Miss}}$	$E_{\mathrm{T}}^{\mathrm{miss,\,no}\,\mu}$	$p_{\mathrm{T}}^{\ell\ell}$
	Resolved: [150,200), [200,350) and [350,500) GeV		
	Merged: Larger than 500 GeV		
Fit variable in each $E_{\mathrm{T}}^{\mathrm{Miss}}$ bin	$m_{h_{\mathrm{cand}}}$	muon charge	Event yield

Chapter 9

BACKGROUND ESTIMATION

General purpose collider experiments, such as ATLAS, are not zero-background experiments. This is for two main reasons. First, the number of data events recorded is so large that even very strict event selections can select many events in the tails of background processes. This can occur either because such background processes occasionally do produce events in the region of phase space being selected, or because there are mis-measurements or mis-identifications which incorrectly place a background event into the region of phase space being selected. Second, the number of combinations and permutations of valid Standard Model processes makes it difficult for a signal process to not correspond to an irreducible (or almost irreducible) background. In other words, it is likely that there exist Standard Model processes which look signal-like for most conceivable signal processes. This certainly is the case in this analysis, and as such the dominant backgrounds after the signal region event selections are applied must be modeled very well in order to have a chance to observe a signal on top of them.

This chapter is organized as follows. Section 9.1 discusses which Standard Model processes are the dominant backgrounds for this analysis. Section 9.2 discusses how the $W+$jets and $t\bar{t}$ backgrounds are modeled using the 1-lepton Control Regions. And Section 9.3 discusses how the $Z+$jets background is modeled using the 2-lepton Control Region.

9.1 Dominant Backgrounds

After all SR event selections are applied, the remaining dominant backgrounds in this analysis are $Z+$jets, $W+$jets, and $t\bar{t}$. These processes are shown in Figures 9.1, 9.2, and 9.3. It can been seen from Figure 9.1 that $Z+$jets can fake the mono-Higgs signal process if the Z decays to neutrinos, faking the Dark Matter $E_{\mathrm{T}}^{\mathrm{Miss}}$, and the jets originate from a pair of b-quarks, faking the Higgs boson. A similar $W+$jets process, such as the one shown in

Figure 9.2, can also fake the mono-Higgs signal if the charged lepton from a leptonic W decay fails to be reconstructed. A semi or fully leptonic $t\bar{t}$ process can fake the mono-Higgs signal when the resulting charged lepton(s) fail to be reconstructed.

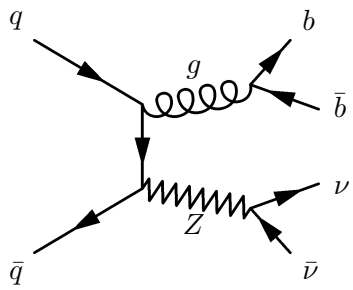

Figure 9.1: An example of a Z + jets hard scatter process where the Z boson decays to neutrinos. The process contaminates the Dark Matter signal if the jets fake a Higgs candidate.

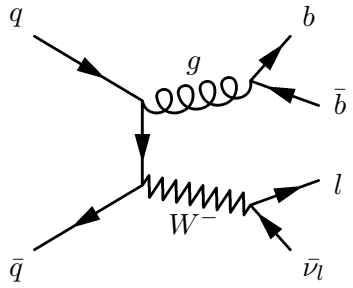

Figure 9.2: An example of a W + jets hard scatter process where the W boson decays to a lepton and a neutrino. The process contaminates the Dark Matter signal if the jets fake a Higgs candidate and if the lepton fails to be reconstructed.

The yields of these three dominant background processes after all event selections are applied are estimated using MC simulation, and their modelling is constrained using the 1- and 2-lepton Control Regions. The multi-jet, diboson, single top, and Vh backgrounds are also all estimated using MC simulation. A data-driven multi-jet background estimation was explored and was found to decrease the uncertainty on the final multi-jet yield - however,

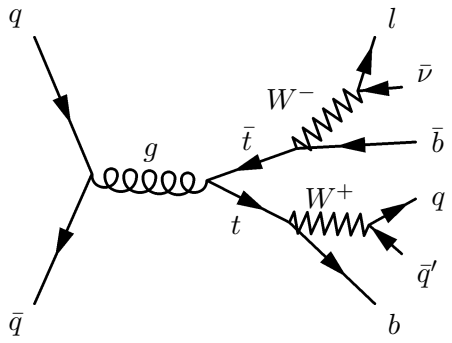

Figure 9.3: An example of a $t\bar{t}$ hard scatter process where one W boson decays to leptons and neutrinos and the other decays to quarks which produce jets. The process contaminates the Dark Matter signal if the jets fake a Higgs candidate and the lepton fails to be reconstructed. Some cuts, such as the H_{T} cut, help to reduce some of this background, by targeting the high jet multiplicity.

the final multi-jet yield was found to be substantially smaller than the statistical uncertainty of the data, and so the multi-jet process was not included in the final fit. The multi-jet yield predictions in the Signal Region are shown in Table 9.1. The breakdown of backgrounds in the Control Regions is shown in the following sections.

Table 9.1: Yield predictions for the multi-jet background in the 0-lepton Signal Region as determined in MC [2].

SR $E_{\mathrm{T}}^{\mathrm{Miss}} bin$	multi-jet yield prediction
150 GeV $< E_{\mathrm{T}}^{\mathrm{Miss}} <$ 200 GeV	38 ± 17
200 GeV $< E_{\mathrm{T}}^{\mathrm{Miss}} <$ 350 GeV	14 ± 22
350 GeV $< E_{\mathrm{T}}^{\mathrm{Miss}} <$ 500 GeV	0.1 ± 81
$E_{\mathrm{T}}^{\mathrm{Miss}} >$ 500 GeV	—

9.2 Controlling $\mathbf{W}$ + jets *and* $\mathbf{t\bar{t}}$

Figure 9.4 shows the pre- and post-fit distributions of the Higgs candidate mass in the four $E_{\mathrm{T}}^{\mathrm{Miss,\ no\ }\mu}$ bins of the 1-lepton Control Region. The purity of the W + jets and $t\bar{t}$ background is high, so performing the combined fit using these channels will help constrain the normalization of these backgrounds.

It can also be seen in these plots that $t\bar{t}$ tends to dominate in the lower $E_{\mathrm{T}}^{\mathrm{Miss}}$ bins, while the fraction of W + jets events increases in the higher $E_{\mathrm{T}}^{\mathrm{Miss}}$ bins.

There is a larger fraction of W + jets events that result in anti-muons than W + jets events that result in muons. This is because positive W bosons are produced in LHC proton-proton collisions more often than negative W bosons due to the PDF of the protons. Valence u-quarks interacting with sea $\bar{d}$-quarks produce the majority of W^+ bosons in W + jets processes, whereas valence d-quarks interacting with sea $\bar{u}$-quarks produce the majority of W^- bosons in W + jets processes. Since there are two valence u-quarks, but only one valence d-quark, in protons, more W^+ than W^- are produced in W + jets events. The ratio of the production cross sections of W^+ + jets to W^- + jets must take into account the full PDFs of the colliding protons, not just the relative abundance of valence u- and d-quarks, and is approximately 1.4 for $\sqrt{s} = 7$ TeV proton-proton collisions at the LHC [100]. This asymmetric $W^{\pm}$ + jets production motivated the use of separate μ^+ and μ^- bins in the 1-lepton Control Region in order to obtain regions with relatively higher purities of $W^{\pm}$ + jets or $t\bar{t}$.

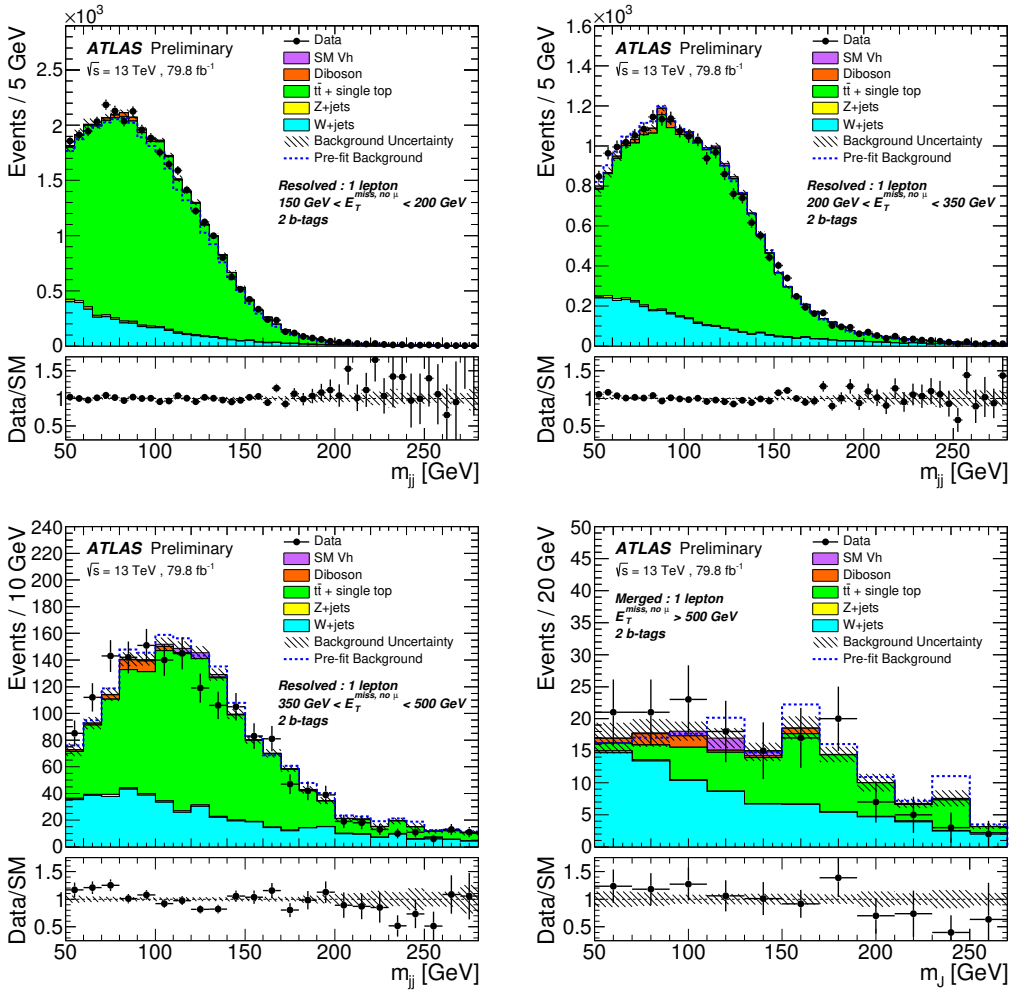

Figure 9.4: Higgs candidate mass distributions in the four $E_{\mathrm{T}}^{\mathrm{Miss,\ no\ }\mu}$ bins of the 1-lepton Control Region [2].

The final 1-lepton Control Region bins considered for the combined fit are then the four $E_{\mathrm{T}}^{\mathrm{Miss,\ no\ }\mu}$ bins times the two muon charge bins, for a total of eight bins.

9.3 Controlling **Z** + jets

Figure 9.5 shows the pre- and post-fit distributions of the dilepton mass in the four $p_{\mathrm{T}}^{l\bar{l}}$ bins in the 2-lepton Control Region, broken down into a 2-electron region and a 2-muon region. Breaking down the 2-lepton Control Region into electron and muon regions proved useful for the development of the analysis, but the final fit combined these two regions into a single 2-lepton region with four $p_{\mathrm{T}}^{l\bar{l}}$ bins, for a total of four bins.

Figure 9.6 shows the pre- and post-fit distributions of the Higgs mass candidate in the four $p_{\mathrm{T}}^{l\bar{l}}$ bins in the 2-lepton Control Region, with the 2-electron and 2-muon regions combined. In both Figure 9.5 and Figure 9.6 the Z + jets background is very high when Z decays to leptons. Though this is not the dominant Z + jets background of the analysis, where the Z decays to neutrinos, the overall normalization factor between $Z(l\bar{l})$ + jets and $Z(\nu\bar{\nu})$ + jets is assumed to be the same.

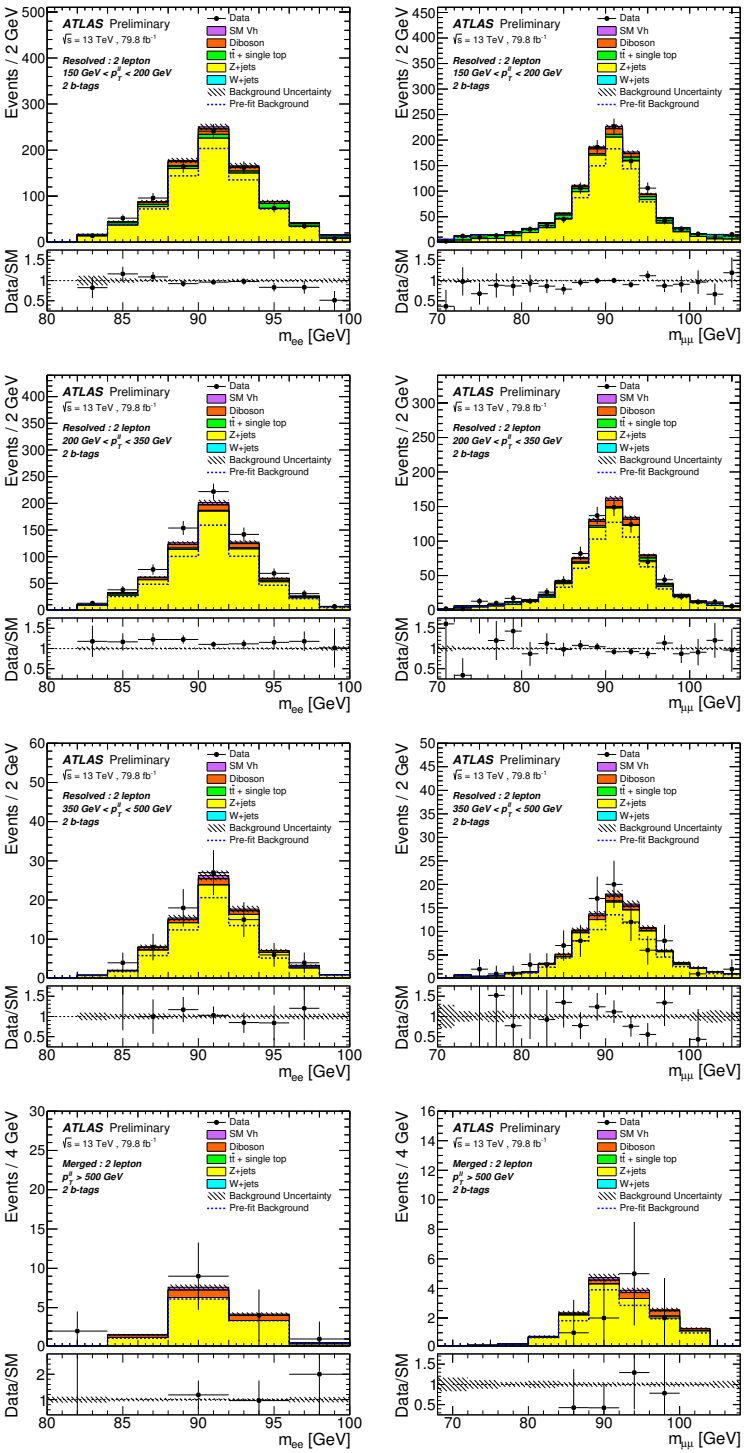

Figure 9.5: Dilepton mass distributions in the four $p_{\mathrm{T}}^{l\bar{l}}$ bins of the 2-lepton Control Region [2].

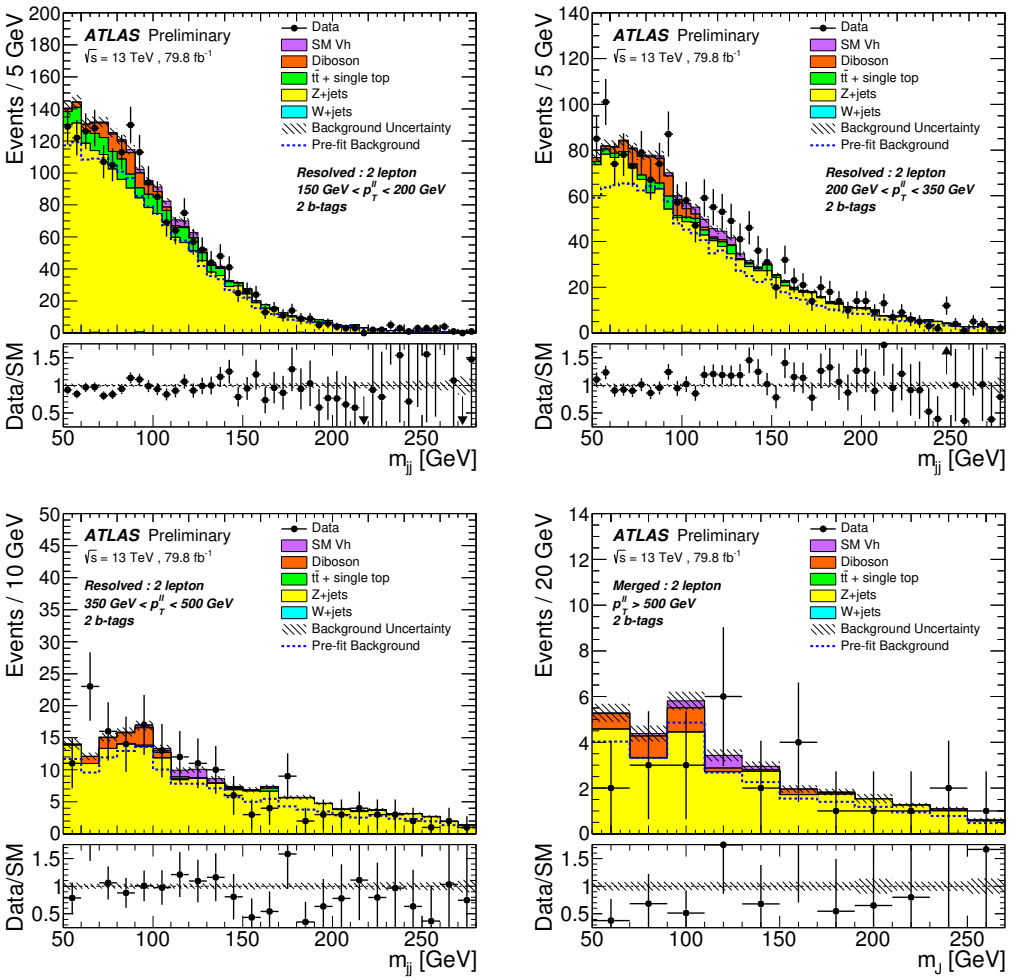

Figure 9.6: Higgs candidate mass distributions in the four $p_{\mathrm{T}}^{l\bar{l}}$ bins of the 2-lepton Control Region [2].

Chapter 10

SYSTEMATIC UNCERTAINTIES

Several systematic uncertainties, such as those related to calibrations of objects and normalizations of SM backgrounds, are considered by this analysis. Most systematic uncertainties considered are parameterized by nuisance parameters (NPs) that are constrained in the combined fit used to derive final yields and limits. An overview of all uncertainties considered by this analysis is presented in this chapter, with experimental uncertainties introduced in Section 10.1, background modelling uncertainties introduced in Section 10.2, and signal modelling uncertainties introduced in Section 10.3.

10.1 Experimental Uncertainties

A list of the experimental systematic uncertainties for jets considered by this analysis is tabulated in Table 10.1, accompanied by a brief description of the uncertainty. All other experimental systematic uncertainties with brief descriptions are tabulated in Table 10.2.

10.1.1 Event Uncertainties

The total integrated luminosity of the dataset used corresponds to 79.8 fb^{-1} with an uncertainty of 2.0%.

10.1.2 Electron Uncertainties

The scale factors and their uncertainties for correcting the mis-modelling of electron reconstruction, identification, isolation, and trigger were determined using $Z \to e\bar{e}$, $W \to e\nu$ and $J/\Psi \to e\bar{e}$ simulated samples. The scale factors and their uncertainties were binned in p_{T} and η. The trigger scale factors were only used in the 2-lepton Control Region, where electron triggers are applied, while the reconstruction, identification, and isolation scale factors

Table 10.1: Table of the experimental systematic uncertainties for jets considered by the analysis.

Systematic Uncertainty	Short Description
	Small-R Jets
JET_GroupedNP	energy scale uncertainty parameterized in three components
JET_SR1_JET_EtaIntercalibration_NonClosure	non-closure in the jet response at $2.4 < \|\eta\| < 2.5$
JET_SR1_JER_SINGLE_NP	energy resolution uncertainty
JvtEfficiency	JVT efficiency uncertainty
FT_EFF_EIGEN_B	b-tagging efficiency uncertainty for b-jets
FT_EFF_EIGEN_C	b-tagging efficiency uncertainty for c-jets
FT_EFF_EIGEN_L	b-tagging efficiency uncertainty for light-jets
FT_EFF_EIGEN_extrapolation	b-tagging efficiency uncertainty on the extrapolation on high p_{T} jets
FT_EFF_EIGEN_extrapolation_from_charm	b-tagging efficiency uncertainty on τ-jets
	Large-R Jets
FATJET_JMR	mass resolution uncertainty
FATJET_JER	energy resolution uncertainty
JET_Comb_Baseline_Kin	energy scale uncertainties
JET_Comb_Modelling_Kin	energy scale uncertainties
JET_Comb_TotalStat_Kin	energy scale uncertainties
JET_Comb_Tracking_Kin	energy scale uncertainties
	VR Track Jets
FT_EFF_EIGEN_B	b-tagging efficiency uncertainty for b-jets
FT_EFF_EIGEN_C	b-tagging efficiency uncertainty for c-jets
FT_EFF_EIGEN_L	b-tagging efficiency uncertainty for light-jets
FT_EFF_EIGEN_extrapolation	b-tagging efficiency uncertainty on the extrapolation on high p_{T} jets
FT_EFF_EIGEN_extrapolation_from_charm	b-tagging efficiency uncertainty on τ-jets

Table 10.2: Table of non-jet experimental systematic uncertainties considered by the analysis.

Systematic Uncertainty	Short Description
	Event
Luminosity	uncertainty on the total integrated luminosity
PRW_DATASF	uncertainty on data scale factor used for computation pile-up re-weighting
	Electrons
EL_EFF_Trigger_TOTAL_1NPCOR_PLUS_UNCOR	trigger efficiency uncertainty
EL_EFF_Reco_TOTAL_1NPCOR_PLUS_UNCOR	reconstruction efficiency uncertainty
EL_EFF_ID_TOTAL_1NPCOR_PLUS_UNCOR	identification efficiency uncertainty
EL_EFF_Iso_TOTAL_1NPCOR_PLUS_UNCOR	isolation efficiency uncertainty
EG_SCALE_ALL	energy scale uncertainty
EG_RESOLUTION_ALL	energy resolution uncertainty
	Muons
mu20_iloose_L1MU15_OR_HLT_mu40_MUON_EFF_Trig	trigger efficiency uncertainties
mu24_ivarmed_OR_HLT_mu40_MU_EFF_TrigStat	trigger efficiency uncertainties
mu24_ivarmed_OR_HLT_mu50_MU_EFF_TrigStat	trigger efficiency uncertainties
mu26_ivarmed_OR_HLT_mu50_MU_EFF_TrigStat	trigger efficiency uncertainties
MUON_EFF_RECO_STAT	statistical reconstruction uncertainty for $p_{\mathrm{T}} > 15$ GeV
MUON_EFF_RECO_SYS	systematic reconstruction uncertainty for $p_{\mathrm{T}} > 15$ GeV
MUON_EFF_RECO_STAT_LOWPT	statistical reconstruction uncertainty for $p_{\mathrm{T}} < 15$ GeV
MUON_EFF_RECO_SYS_LOWPT	systematic reconstruction uncertainty for $p_{\mathrm{T}} < 15$ GeV
MUON_ISO_STAT	statistical isolation efficiency uncertainty
MUON_ISO_SYS	systematic isolation efficiency uncertainty
MUON_TTVA_STAT	statistical track-to-vertex association efficiency uncertainty
MUON_TTVA_SYS	systematic track-to-vertex association efficiency uncertainty
MUONS_SCALE	energy scale uncertainty
MUONS_SAGITTA_RHO	variations in the scale of the momentum (charge dependent)
MUONS_SAGITTA_RESBIAS	variations in the scale of the momentum (charge dependent)
MUONS_ID	energy resolution uncertainty from inner detector
MUONS_MS	energy resolution uncertainty from muon spectrometer
	Taus
TAUS_TRUEHADTAU_SME_TES_DETECTOR	tau energy scale uncertainty from detector effects
TAUS_TRUEHADTAU_SME_TES_INSITU	tau energy scale uncertainty from in-situ calibration
TAUS_TRUEHADTAU_SME_TES_MODEL	tau energy scale uncertainty from modelling
TRK_EFF_LOOSE_TIDE	track efficiency reconstruction uncertainty
TRK_FAKE_RATE_LOOSE	fake track reconstruction uncertainty
	$\mathbf{E}_{\mathrm{T}}^{\mathrm{Miss}}$
METTrigStat	$E_{\mathrm{T}}^{\mathrm{Miss}}$ trigger efficiency statistical uncertainty
METTrigSyst	$E_{\mathrm{T}}^{\mathrm{Miss}}$ trigger efficiency systematic uncertainty
MET_SoftTrk_ResoPerp	track-based soft term related to transversal resolution uncertainty
MET_SoftTrk_ResoPara	track-based soft term related to longitudinal resolution uncertainty
MET_SoftTrk_Scale	track-based soft term related to longitudinal scale uncertainty
MET_JetTrk_Scale	track $E_{\mathrm{T}}^{\mathrm{Miss}}$ scale uncertainty due to tracks in jets

were applied in all regions. Uncertainties on the electron energy scale and resolution were determined according to References [80] [101].

10.1.3 Muon Uncertainties

The scale factors and their uncertainties for correcting the mis-modelling of muon reconstruction plus identification, isolation, trigger, and track-to-vertex assocation efficiencies were determined using $Z \to \mu\bar{\mu}$ and $J/\Psi \to \mu\bar{\mu}$ simulated samples. The trigger scale factors were only used in the 2-lepton Control Region, where muon triggers are applied, while the remaining scale factors were applied in all regions. Uncertainties on the muon energy scale and resolution were determined according to Reference [82].

10.1.4 Tau Uncertainties

Uncertainties on the tau energy scale (TES) are considered for taus reconstructed via the standard ATLAS tau reconstruction and identification algorithms, discussed previously in Section 7.6, including the TES uncertainties from detector effects, in-situ calibration, and modelling. Uncertainties considered for taus reconstructed via the looser "extended tau" definition, also discussed previously in Section 7.6, include uncertainties on track and fake track reconstruction efficiencies.

10.1.5 $E_{\mathrm{T}}^{\mathrm{Miss}}$ Uncertainties

The uncertainties on the hard $E_{\mathrm{T}}^{\mathrm{Miss}}$ terms, namely on the electrons, muons, and jets used to calculate $E_{\mathrm{T}}^{\mathrm{Miss}}$ as described in Section 7.7, were considered as described in Sections 10.1.2, 10.1.3, and 10.1.6, respectively. Uncertainties related to the resolution of the transverse projection of the $E_{\mathrm{T}}^{\mathrm{Miss}}$ soft term onto the $E_{\mathrm{T}}^{\mathrm{Miss}}$ hard term and uncertainties related to the resolution and scale of the longitudinal projection of the $E_{\mathrm{T}}^{\mathrm{Miss}}$ soft term onto the $E_{\mathrm{T}}^{\mathrm{Miss}}$ hard term are additionally considered [95]. Track-in-jet uncertainties are considered for $p_{\mathrm{T}}^{\mathrm{Miss}}$ [95].

Statistical and systematic uncertainties of the $E_{\mathrm{T}}^{\mathrm{Miss}}$ trigger are also considered.

10.1.6 Small-R Jet Uncertainties

Three calibration methods provide jet energy calibrations for small-R jets: an in-situ calibration, an η inter-calibration, and a high p_{T} and high pile-up calibration [85]. These calibration methods provide a total set of 88 nominal nuisance parameters which constrain the jet energy scale. This analysis employs a largely reduced set consisting of a non-closure uncertainty on the η inter-calibration and three additional nuisance parameters which combine the other 87 nominal nuisance parameters. A single nuisance parameter is used to constrain the jet energy resolution. Scale factors and uncertainties for the JVT efficiency are also considered.

In addition to jet energy scale, jet energy resolution, and JVT calibrations, calibrations providing scale factors and their uncertainties for the flavor-tagging efficiencies of small-R jets are considered in this analysis. This includes the b-tagging efficiency and mis-tag rates for jets originating from b-quarks, c-quarks, and light quarks, as well as efficiencies and uncertainties on the extrapolation of b-tagging for high p_{T} jets and τ-jets.

10.1.7 Large-R Jet Uncertainties

Four nuisance parameters constrain the jet energy and jet mass scale of large-R jets. These parameters are derived from differences between data and MC simulation and are related to the fragmentation modelling of the jets, the tracking reconstruction efficiency of the tracks associated to the jets, the fake rate and q/p_{T} bias of the tracks associated to the jets, and the statistical uncertainty on the jet energy and mass scale measurement. The jet energy and jet mass scale uncertainties are treated as being fully correlated. A single nuisance parameter constrains the jet energy resolution, and a single nuisance parameter constrains the jet mass resolution [102].

10.1.8 VR Track Jet Uncertainties

Only flavor tagging calibration scale factors and their uncertainties are considered for VR track jets. The b-tagging efficiency and its uncertainty was derived independently for VR track jets, using the same technique as for small-R jet b-tagging. However, the scale factors

and their uncertainties for the b-tagging mis-tag rates for jets originating from c-quarks and light-quarks, as well as efficiencies and uncertainties on the extrapolation of b-tagging for high p_{T} jets and τ-jets, derived for small-R jets were directly used for VR track jets.

10.2 Background Modelling Uncertainties

The background modelling uncertainties considered by this analysis for the three dominant backgrounds, $t\bar{t}$, $Z+$jets, and $W+$jets, are shown in Table 10.3. All other background modelling uncertainties considered by this analysis are listed in Table 10.4. In general, there are three main types of modelling uncertainties considered: normalization uncertainties, uncertainties in the relative acceptances in the different analysis regions, and uncertainties in the shapes of kinematic distributions. Normalizations and their uncertainties for the SM backgrounds are taken from calculations by the event generators of their cross sections. Systematic uncertainties on the acceptance differences and shapes are derived either from particle-level comparisons between nominal and alternative samples, or from comparisons to data in control regions.

The normalization of $t\bar{t}$, $Z+bb$, and $W+bb$ are referred to in plots and tables as `norm_ttbar`, `norm_Zbb`, and `norm_Wbb`, respectively, and are treated as free parameters. However, uncertainties on the shapes of the m_{jj} and p_{T}^{V} spectra for $t\bar{t}$, $Z+$jets, and $W+$jets are constrained using the same methods described in Reference [103].

The normalizations on $Z+bc$, $Z+bl$, and $Z+cc$ are constrained by nuisance parameters describing their relative abundance with respect to $Z+bb$, and are referred to in plots and tables as `ZbcZbbRatio`, `ZblZbbRatio`, and `ZccZbbRatio`, respectively. However, since the normalization of $Z+bb$ is a free parameter, this effectively allows the overall normalization of $Z+$HF to behave as a free parameter, where only the flavor breakdown of the heavy flavor jets is constrained. Similarly, the normalizations of $W+bc$, $W+bl$, and $W+cc$ are constrained by nuisance parameters describing their relative abundance with respect to $W+bb$, and are referred to in plots and tables as `WbcWbbRatio`, `WblWbbRatio`, and `WccWbbRatio`, respectively. The normalizations of $Z+cl$ and $W+cl$ are treated as nuisance parameters and are referred to in plots and tables as `ZclNorm` and `WclNorm`, respectively.

Acceptance uncertainties are estimated for the relative normalizations of the different

Table 10.3: Table of the background modelling systematic uncertainties considered by the analysis for the three dominant backgrounds, $t\bar{t}$, $Z+$jets, and $W+$jets.

Systematic Uncertainty	Short Description
	$t\bar{t}$
`norm_ttbar`	free parameter
`ttbarMbb`	uncertainty on m_{jj} spectrum shape
`SysttbarPTVshapeOnly`	uncertainty on p_{T}^{V} spectrum shape
	$Z+$jets
`norm_Zbb`	free parameter
`ZMbb`	uncertainty on m_{jj} spectrum shape
`ZPTVshapeOnly`	uncertainty on p_{T}^{V} spectrum shape
`ZbbNorm_L0`	de-correlation of 0 lepton from 1 lepton regions
`ZbcZbbRatio`	de-correlation of $Z+bc$ from $Z+bb$
`ZbcZbbRatio_L0`	additional de-correlation of 0 lepton from 1 lepton regions
`ZbcZbbRatio_L2`	additional de-correlation of 0 lepton from 2 lepton regions
`ZblZbbRatio`	de-correlation of $Z+bl$ from $Z+bb$
`ZblZbbRatio_L0`	additional de-correlation of 0 lepton from 1 lepton regions
`ZblZbbRatio_L2`	additional de-correlation of 0 lepton from 2 lepton regions
`ZccZbbRatio`	de-correlation of $Z+cc$ from $Z+bb$
`ZccZbbRatio_L0`	additional de-correlation of 0 lepton from 1 lepton regions
`ZccZbbRatio_L2`	additional de-correlation of 0 lepton from 2 lepton regions
`ZclNorm`	normalization uncertainty for $Z+cl$
	$W+$jets
`norm_Wbb`	free parameter
`WMbb`	uncertainty on m_{jj} spectrum shape
`WPTVshapeOnly`	uncertainty on p_{T}^{V} spectrum shape
`WbbNorm_L0`	de-correlation of 0 lepton from 1 lepton regions
`WbcWbbRatio`	de-correlation of $W+bc$ from $W+bb$
`WblWbbRatio`	de-correlation of $W+bl$ from $W+bb$
`WccWbbRatio`	de-correlation of $W+cc$ from $W+bb$
`WclNorm`	normalization uncertainty for $W+cl$

regions that share a common floating normalization parameter. For W + HF, there is an uncertainty in the ratio of the event yield in the 0-lepton Signal Region to that in the 1-lepton Control Region, and is referred to as `WbbNorm_L0` in plots and tables. For Z + HF, there are uncertainties in the ratios of the event yield in the 0-lepton Signal Region to that in the 1-lepton Control Region (`ZbbNorm_L0`, `ZbcZbbRatio_L0`, `ZblZbbRatio_L0`, and `ZccZbbRatio_L0` in plots and tables) and in the ratio of the event yield in the 0-lepton Signal Region to that in the 2-lepton Control Region (`ZbcZbbRatio_L2`, `ZblZbbRatio_L2`, and `ZccZbbRatio_L2` in plots and tables).

Normalization uncertainties, m_{jj} spectrum shape uncertainties, p_{T}^{V} spectrum shape uncertainties, and shape variations of the m_{jj} and p_{T}^{V} spectra due to uncertainties in particle shower and underlying event simulation are considered for single top and diboson backgrounds. Only normalization uncertainties are considered for the SM Vh background. Uncertainties due do the PDFs, renormalization scale, and particle shower tunes are also considered.

Table 10.4: Table of the background modelling systematic uncertainties considered by the analysis.

Systematic Uncertainty	Short Description
	Single Top
`stopWtNorm`	normalization uncertainty for Wt
`stopWtMbb`	uncertainty on m_{jj} spectrum shape
`stopWtPTVshapeOnly`	uncertainty on p_{T}^{V} spectrum shape
`stopsNorm`	normalization uncertainty for s-channel single top
`stoptNorm`	normalization uncertainty for t-channel single top
`stoptMbb`	uncertainty on m_{jj} spectrum shape
`stoptPTVshapeOnly`	uncertainty on p_{T}^{V} spectrum shape
	Diboson
`ZZNorm`	normalization uncertainty for ZZ
`ZZMbb`	uncertainty on m_{jj} spectrum shape
`ZZMbbpsue`	uncertainty on m_{jj} spectrum shape due to particle showers and underlying event
`ZZPTVshapeOnly`	uncertainty on p_{T}^{V} spectrum shape
`ZZPTVpsueshapeOnly`	uncertainty on p_{T}^{V} spectrum shape due to particle showers and underlying event
`WZNorm`	normalization uncertainty for WZ
`WZMbb`	uncertainty on m_{jj} spectrum shape
`WZMbbpsue`	uncertainty on m_{jj} spectrum shape due to particle showers and underlying event
`WZPTVshapeOnly`	uncertainty on p_{T}^{V} spectrum shape
`WZPTVpsueshapeOnly`	uncertainty on p_{T}^{V} spectrum shape due to particle showers and underlying event
`WWNorm`	normalization uncertainty for WW
`WWMbb`	uncertainty on m_{jj} spectrum shape
`WWMbbpsue`	uncertainty on m_{jj} spectrum shape due to particle showers and underlying event
`WWPTVshapeOnly`	uncertainty on p_{T}^{V} spectrum shape
	Vh
`HiggsNorm`	normalization uncertainty for Vh

10.3 Signal Modelling Uncertainties

Uncertainties on the acceptance of the $Z'-$2HDM signal samples are included in the statistical fit. These uncertainties originate from modelling uncertainties and are evaluated by considering variations of the modelling parameters used by the MadGraph5_aMC@NLO 2.2.3+Pythia 8 signal model simulation. These uncertainties were taken from estimates by a previous analysis iteration [8]. While the event selection of the previous analysis iteration differs somewhat from the event selection of this iteration, it was assumed that the uncertainties on the signal acceptance were comparable enough to not warrant reproducing these uncertainty estimations. A brief summary of the signal modelling uncertainties considered is shown in Table 10.5.

The uncertainty in the signal modelling due to the PDF was estimated by replacing the nominal NNPDF2.3 PDF set with the MSTW2008lo68cl PDF set [104] and CTEQ6L1 PDF set [105] and taking the largest deviation from the nominal PDF in signal acceptance. This uncertainty is referred to as `PDFSig` in tables and plots.

The uncertainty in the renormalization and factorization scales of simulated signal processes is estimated by varying the default scales by a factor of 2 and 1/2. The default renormalization and factorization scales used in MadGraph when generating signal events are dynamically set to $M_{\mathrm{T}}^2 + P_{\mathrm{T}}^2$, where M_{T} and P_{T} stand for the transverse mass and transverse momentum of the four-momentum sum of the final state particles. This uncertainty is referred to as `ScaleSig` in tables and plots.

Uncertainty sources on the final state radiation, initial state radiation, and multi-parton

Table 10.5: Table of the signal modelling systematic uncertainties considered by the analysis.

Systematic Uncertainty	Short Description
	Signal
`PDFSig`	PDF uncertainty for signal samples
`ScaleSig`	renormalization scale uncertainty for signal samples
`TunesSig`	shower model uncertainty for signal samples

interactions were parameterized as a subset of tune variations providing maximal variation coverage for underlying event effects, jet structure effects, and additional jet production. This uncertainty is referred to as `TunesSig` in tables and plots.

Chapter 11

RESULTS

This Chapter presents the final results of this mono-Higgs search. Section 11.1 describes the statistical methods used to determine signal strength, Section 11.2 then presents the final event yields, Section 11.3 presents the impact of uncertainties to signal yield predictions, Section 11.4 presents the final observed exclusion limits on the $Z'-2$HDM model, and finally Section 11.5 presents studies comparing the use of $R = 0.2$ track jets and VR track jets in the analysis.

11.1 Statistical Interpretation

The MC simulation of signal and background processes are fit to the data using a maximum likelihood approach, where the maximum likelihood function is defined as follows:

$$\begin{aligned} L(\mu, \boldsymbol{\theta}) = &\left[\prod_{i}^{N_{\text{SR bins}}} \text{Poisson}(n_i | \mu S_i(\boldsymbol{\theta}) + B_i(\boldsymbol{\theta})) \right] \\ &\cdot \left[\prod_{j}^{N_{\text{CR bins}}} \text{Poisson}(n_j | B_j(\boldsymbol{\theta})) \right] \\ &\cdot \left[\prod_{k}^{N_{\text{NPs}}} \text{Gauss}(\theta_k | \bar{\theta}_k, \sigma_k^2) \right] \end{aligned} \tag{11.1}$$

where the n_i are the yields of data in the bins of the Signal Region, the n_j are the yields of data in the bins of the Control Regions, and S and B are the predicted signal and background yields from the MC simulations. B is broken down into $Z + \text{HF}$, $W + \text{HF}$, $t\bar{t}$, and other backgrounds in the following way:

$$B(\boldsymbol{\theta}) = \mu_{Z+\text{HF}} B_{Z+\text{HF}}(\boldsymbol{\theta}) + \mu_{W+\text{HF}} B_{W+\text{HF}}(\boldsymbol{\theta}) + \mu_{t\bar{t}} B_{t\bar{t}}(\boldsymbol{\theta}) + B_{\text{other}}(\boldsymbol{\theta}) \tag{11.2}$$

where $\mu_{Z+\text{HF}}$, $\mu_{W+\text{HF}}$, and $\mu_{t\bar{t}}$ are treated as free parameters that allow for independent normalization of these three dominant backgrounds. μ is the signal strength, also a free

parameter. $\boldsymbol{\theta} = (\theta_1, \theta_2, \ldots, \theta k, \ldots, \theta_{N_{\text{NPs}}})$ is a vector of nuisance parameters which are the variables which control the systematic uncerties, such as the Jet Energy Scale or b-tagging calibration scale factors. These nuisance parameters are Gaussian weighted.

To be explicit, the functions of Equation 11.1 are written out as follows:

$$\text{Poisson}(n_i|\mu S_i(\boldsymbol{\theta}) + B_i(\boldsymbol{\theta})) = \frac{(\mu S_i(\boldsymbol{\theta}) + B_i(\boldsymbol{\theta}))^{n_i} e^{-(\mu S_i(\boldsymbol{\theta}) + B_i(\boldsymbol{\theta}))}}{n_i!} \tag{11.3}$$

$$\text{Poisson}(n_j|B_j(\boldsymbol{\theta})) = \frac{(B_j(\boldsymbol{\theta}))^{n_j} e^{-(B_j(\boldsymbol{\theta}))}}{n_j!} \tag{11.4}$$

$$\text{Gauss}(\theta_k|\bar{\theta}_k, \sigma_k^2) = \frac{1}{\sqrt{2\pi\sigma_k^2}} e^{-\frac{(\theta_k - \bar{\theta}_k)^2}{2\sigma_k^2}} \tag{11.5}$$

Computationally, maximizing this likelihood boils down to iterating over possible values of the free and nuisance parameters. This is much more easily done by first taking the natural logarithm of the likelihood function, which turns the products into sums. This creates the log-likelihood function defined as follows:

$$\begin{aligned} F(\mu, \boldsymbol{\theta}) = & \sum_{i}^{N_{\text{SR bins}}} \ln\left[\text{Poisson}(n_i|\mu S_i(\boldsymbol{\theta}) + B_i(\boldsymbol{\theta}))\right] \\ & + \sum_{j}^{N_{\text{CR bins}}} \ln\left[\text{Poisson}(n_j|B_j(\boldsymbol{\theta}))\right] \\ & + \sum_{k}^{N_{\text{NPs}}} \ln\left[\text{Gauss}(\theta_k|\bar{\theta}_k, \sigma_k^2)\right] \end{aligned} \tag{11.6}$$

The numerical maximization of this function was performed, determining the best values for the free and nuisance parameters. The free-floating normalizations for $t\bar{t}$, $W + \text{HF}$, and $Z + \text{HF}$ were determined to be 1.10 ± 0.08, 1.51 ± 0.22, and 1.42 ± 0.10, respectively.

11.2 Post-Fit Distributions and Yields

Post-fit yields in the eight 1-lepton Control Region bins and four 2-lepton Control Region bins are shown graphically in Figures 11.1 and 11.2, respectively.

Post-fit yields, before the final tight Higgs window mass cut is applied, in the four $E_{\text{T}}^{\text{Miss}}$ bins of the 0-lepton Signal Region are shown graphically in Figure 11.3, and tabulated in Table 11.1. Figure 11.4 shows the post-fit Higgs candidate mass spectra, before the final

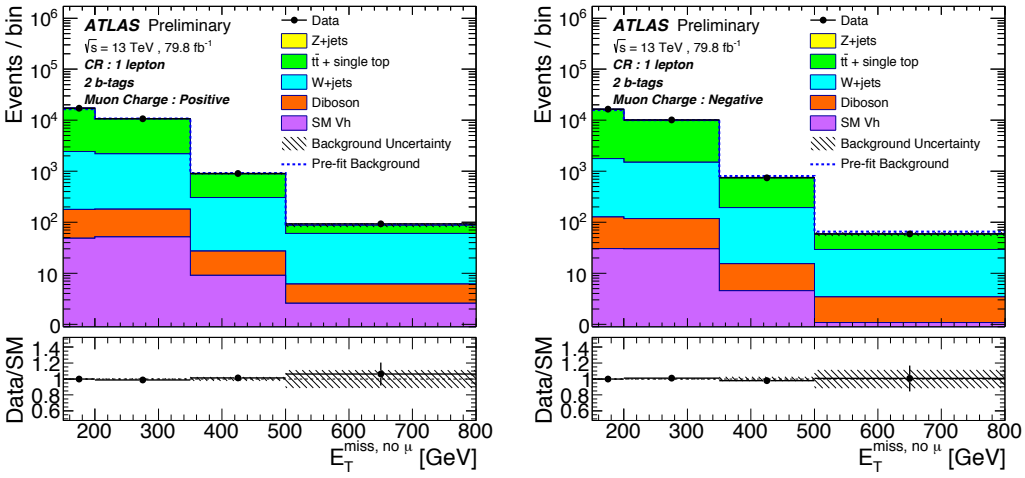

Figure 11.1: Final post-fit $E_{\mathrm{T}}^{\mathrm{Miss,\ no\ }\mu}$ spectra in the 1-lepton μ^+ and μ^- Control Regions [2].

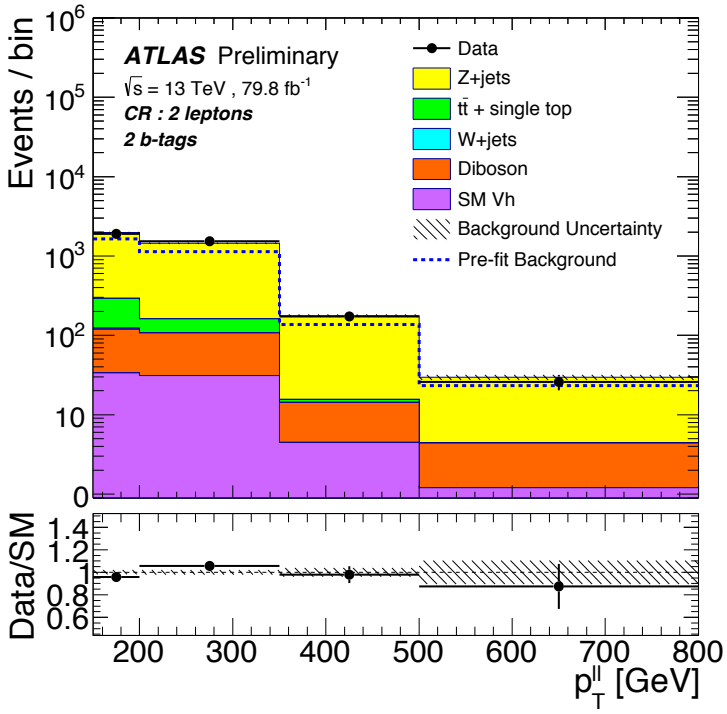

Figure 11.2: Final post-fit $p_{\mathrm{T}}^{l\bar{l}}$ spectra in the 2-lepton Control Region [2].

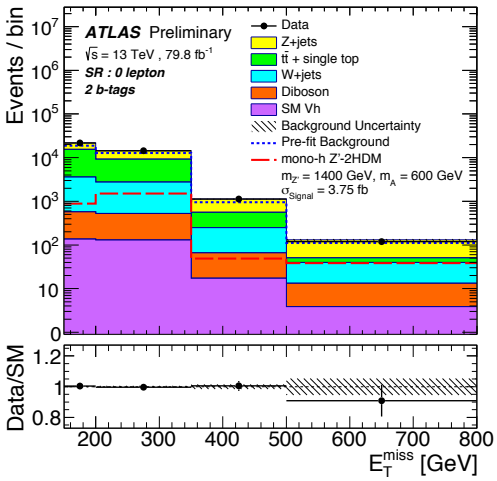

Figure 11.3: Final post-fit yields in the Signal Region each of the four $E_{\mathrm{T}}^{\mathrm{Miss}}$ bins used by the analysis [2].

tight Higgs window mass cut is applied, in the four $E_{\mathrm{T}}^{\mathrm{Miss}}$ bins. In these Figures, a red dashed line indicates the shape of a typical $Z'-$2HDM distribution. The data is well-modelled by the MC simulation, and no excess that would indicate a $Z'-$2HDM is observed.

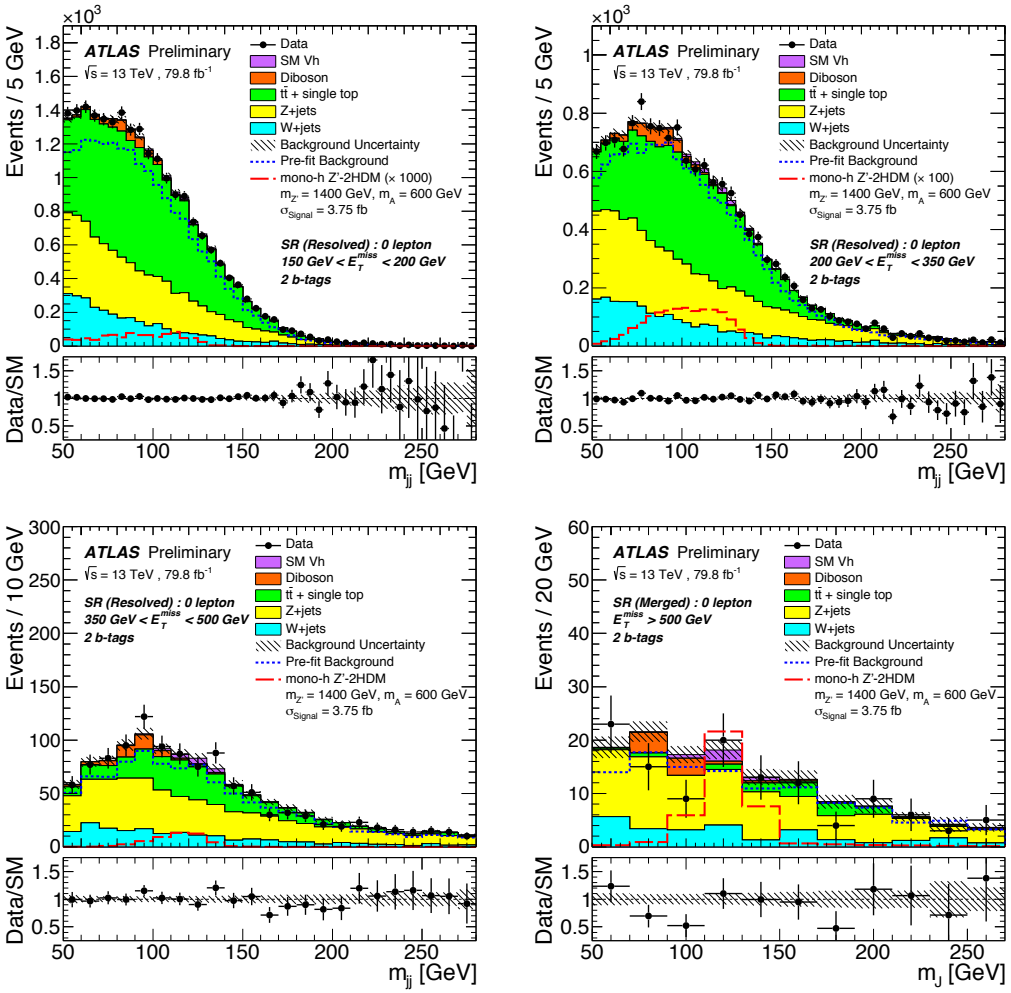

Figure 11.4: Final post-fit Higgs candidate mass spectra in the Signal Region in each of the four $E_{\mathrm{T}}^{\mathrm{Miss}}$ bins used by the analysis [2].

Table 11.1: Event yields for SM MC background after the background-only profile likelihood fit and event yields for observed data in the 0-lepton Signal Region, divided into bins of $E_{\mathrm{T}}^{\mathrm{Miss}}$, with the lower three bins corresponding to the Resolved Channel and the highest bin corresponding to the Merged Channel. Statistical and systematic uncertainties are combined. The uncertainties in the total background take into account the correlation of systematic uncertainties among different background processes. The uncertainties on the total background can be smaller than those on individual components due to anti-correlations between nuisance parameters [2].

Category	Range in $E_{\mathrm{T}}^{\mathrm{Miss}}$ [GeV]			
	$[150, 200)$	$[200, 350)$	$[350, 500)$	$[500, \infty)$
W+jets	3020 $\pm$ 530	2240 $\pm$ 360	184 $\pm$ 32	26.4 $\pm$ 5.7
Z+jets	6330 $\pm$ 450	5180 $\pm$ 340	565 $\pm$ 37	80.5 $\pm$ 6.3
$t\bar{t}$ + single top quark	11 800 $\pm$ 350	6450 $\pm$ 200	308 $\pm$ 25	10.8 $\pm$ 2.5
Diboson	438 $\pm$ 67	400 $\pm$ 59	49.0 $\pm$ 11	9.37 $\pm$ 1.7
Vh	136 $\pm$ 39	129 $\pm$ 37	17.3 $\pm$ 5.0	3.86 $\pm$ 1.1
Background	21 700 $\pm$ 140	14 400 $\pm$ 110	1120 $\pm$ 25	131 $\pm$ 7.2
Data	21818.0	14350.0	1128.0	119.0

11.3 The Impact of Systematic Uncertainties

The final pulls on the nuisance parameters after the combined fit are shown in Figure 11.5. The normalizations of $t\bar{t}$, $Z + bb$, and $W + bb$, which are treated as free parameters in the fit, have the largest pulls. The pull for the normalization of $t\bar{t}$ was $1.10^{+0.08}_{-0.08}$, $1.42^{+0.10}_{-0.10}$ for $Z + bb$, and $1.51^{+0.24}_{-0.24}$ for $W + bb$. The largest pulls for nuisance parameters are as follows:

- `METTrigSyst` ($1.19^{+0.85}_{-0.85}$): the nuisance parameter attributed to the $E_{\mathrm{T}}^{\mathrm{Miss}}$ trigger scale factor systematic uncertainty

- `JET_GroupedNP_1` ($-1.06^{+0.57}_{-0.57}$): the leading nuisance parameter attributed to the jet energy scale calibration

- `FR_EFF_EIGEN_B_1` ($1.02^{+0.78}_{-0.78}$): the leading nuisance parameter attributed to the flavor tagging uncertainty for b-tagged small-R jets

- `WbbNorm_L0` ($0.975^{+0.90}_{-0.90}$): nuisance parameter introduced to partially de-correlate the Signal Region and the 1-lepton Control Region for $W + bb$ processes

The impact of uncertainties on the final signal yield for three representative mass points of the $Z'-$2HDM model is shown in Table 11.2. The total systematic uncertainty is calculated using all sources of systematic uncertainties, though the Table only shows the breakdown of the dominant systematic uncertainty sources. The mass points shown in the Table are (a) $(m_A, m_{Z'}) = (300\ \mathrm{GeV}, 600\ \mathrm{GeV})$, (b) $(m_A, m_{Z'}) = (600\ \mathrm{GeV}, 1400\ \mathrm{GeV})$, and (c) $(m_A, m_{Z'}) = (300\ \mathrm{GeV}, 2600\ \mathrm{GeV})$, with (a) providing a Resolved Channel dominated low-boost signal signature, (c) providing a Merged Channel dominated high-boost signal signature, and (b) providing a medium-boost signal signature. The impact of the sources of uncertainties is evaluated by fixing a set of nuisance parameters (for examples those related to "V + jets modelling") at their nominal post-fit values, and then re-doing the combined fit with other nuisance parameters allowed to vary according to their constraints. The total systematic uncertainty with all nuisance parameters allowed to vary is then compared to the total systematic uncertainty with all nuisance parameters allowed to vary according to

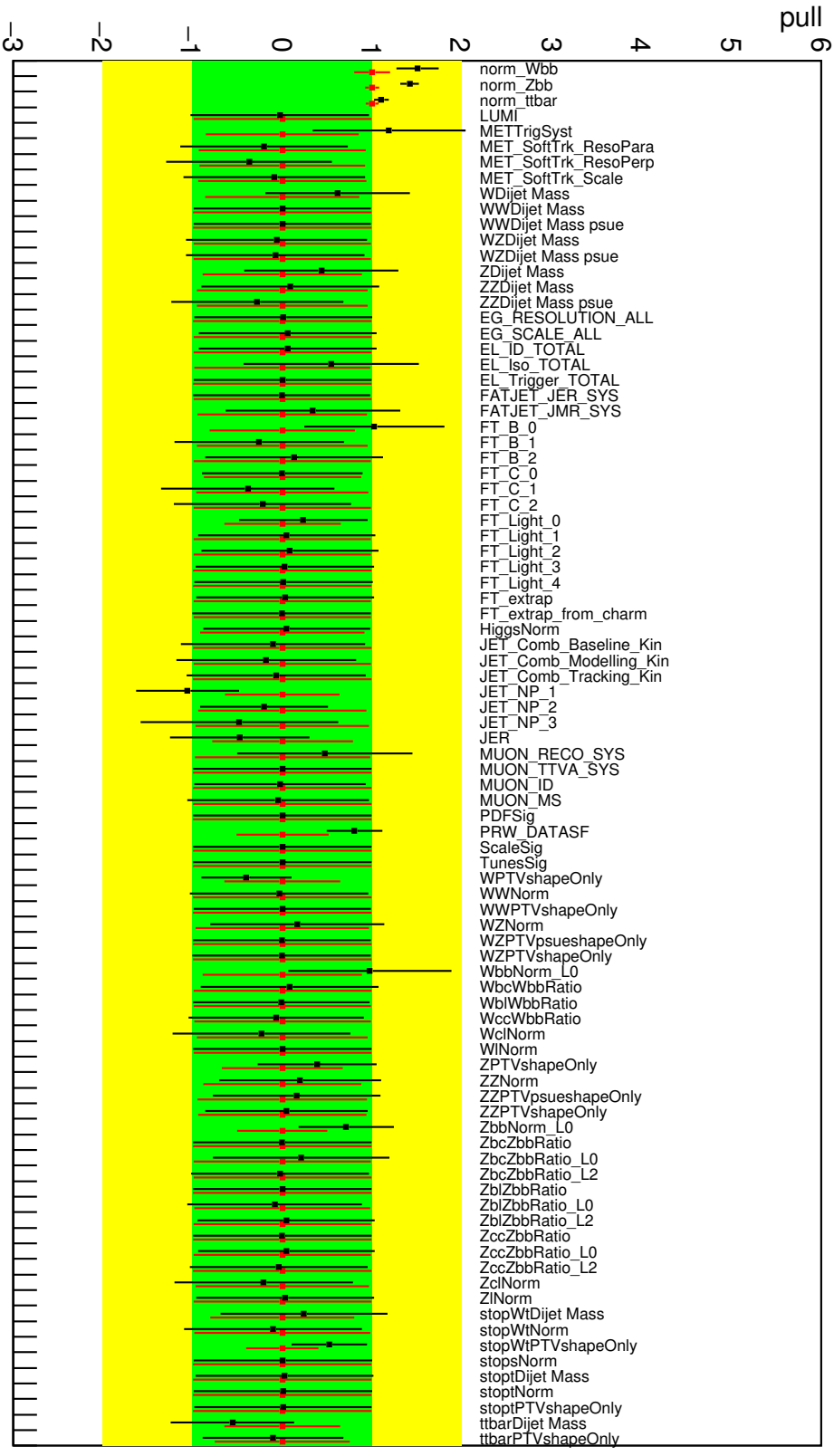

Figure 11.5: The free and nuisance parameter pulls on the background-only profile likelihood fit.

Table 11.2: Impact of dominant uncertainties on the $Z'-$2HDM signal yield for three representative $(m_A, m_{Z'})$ mass points [2].

Uncertainty Source	Impact [%]		
	(a)	(b)	(c)
b-tagging	4	8	10
$V+$jets modelling	3.5	6	5
top modelling	3.7	4.8	4.5
MC statistics	1.8	5.4	4.9
SM $Vh(b\bar{b})$ modelling	0.8	3.2	2.1
signal modelling	3	2.5	1.5
luminosity	2.0	2.5	2.5
small-R jets	1.4	3	2
large-R jets	0.2	1	2
$E_{\mathrm{T}}^{\mathrm{Miss}}$	1.2	1.7	1.1
leptons	0.2	0.8	0.7
total systematic uncertainty	6.5	13	13
total statistical uncertainty	2.3	20	22
total uncertainty	7	24	25

their constraints except for the one set of nuisance parameters fixed to their nominal values. From this comparison, the impact of that set of nuisance parameters can be evaluated.

In all cases, the b-tagging uncertainty has the largest impact, with the impact increasing with an increasing boosted signature. Other large sources of uncertainty include the modelling uncertainties of the dominant backgrounds, $V+$jets and top processes, as well as uncertainties due to limited MC statistics.

For mass points (b) and (c), the total statistical uncertainties become larger than the total systematic uncertainties, suggesting that the analysis is statistically limited in the Merged Channel.

11.4 Exclusion Limits

Since no excess in the data over the SM background predictions was observed, as can be seen from Table 11.1, 95% confidence level (CL) exclusion limits were set on the $h + \text{DM}$ events $\sigma_{h+\text{DM}}$ times the branching ratio $\mathcal{B}(h \to b\bar{b})$. These limits were set using the CL_s method [106] using a profile likelihood ratio test statistic for each signal model mass point independently.

The observed exclusion limits as a function of m_A and $m_{Z'}$ are shown in Figure 11.6 as the solid black line. The dashed black line shows the expected limits and the dashed-dotted grey line shows the exclusion limits of the previous analysis iteration [8]. Mass points of the $Z'-$2HDM model below the limit curves are excluded. The current analysis iteration, based on 79.8 fb^{-1} and VR track jet Higgs tagging, provides much more powerful limits than the previous analysis iteration, based on 36.1 fb^{-1} and $R = 0.2$ track jet Higgs tagging. For $m_A = 300$ GeV, the previous analysis pushed the limits in $m_{Z'}$ up to 2500 GeV, whereas the current analysis iteration pushes the limits in $m_{Z'}$ up to more than 2800 GeV.

In order to achieve an even larger parameter space reach for the mono-Higgs search, further optimizations and improvements could be made to the VR track jet Higgs tagging technique. For example, a dedicated training and optimization of b-tagging algorithms for VR track jets could be pursued.

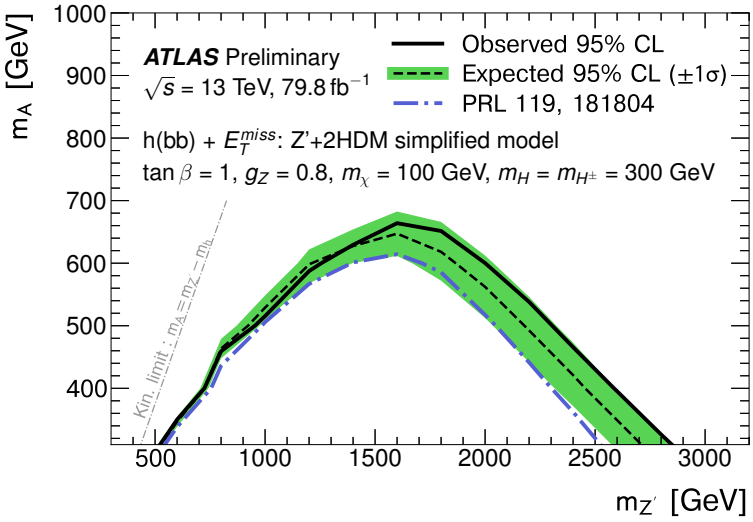

Figure 11.6: Final observed 95% confidence level upper-limits on the $Z'-$2HDM model [2].

11.5 Variable Radius and $\mathbf{R = 0.2}$ *Track Jet Comparisons*

While Figure 11.6 offers a comparison of the exclusion limits obtained from the previous and current analysis iterations, the improvement due to the larger data set of the current analysis and the improvement due to the new Higgs tagging technique used by the current analysis are convoluted. Also, the previous analysis iteration considered both the 1 b-tag and 2 b-tag categories, while the current analysis iteration only considers the 2 b-tag category. In an attempt to make a fairer comparison, expected limits for the current analysis iteration were plotted together with expected limits of the previous analysis iteration, considering only the 2 b-tag category, and scaled to match the current dataset size. This comparison is shown in Figure 11.7.

Figure 11.7a shows the upper limit on the signal strength, μ, as a function of $m_{Z'}$ for a fixed value of $m_A = 500$ GeV. The signal strength is extrapolated linearly between simulated mass points, and any mass point whose signal strength is below one is excluded. Figure 11.7b then shows the final exclusion limits for the $(m_A, m_{Z'})$ parameter space using this technique. It can be seen from both Figure 11.7a and Figure 11.7b that the new analysis iteration can provide much more powerful limits for large $m_{Z'}$ due to the increased efficiency

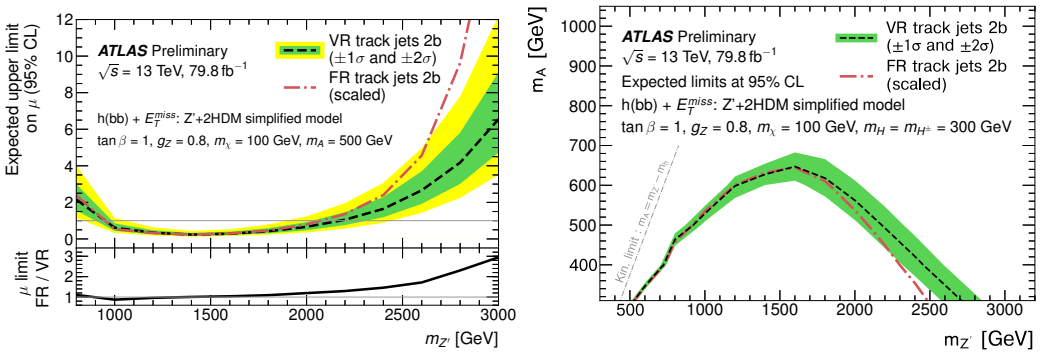

(a) (b)

Figure 11.7: Comparisons of the expected limits on the $Z'-$2HDM model using FR and VR track jets. The limits for FR are taken from the previous analysis iteration using 36 fb^{-1} of data, scaled to match the current analysis iteration's 80 fb^{-1} of data [2].

of VR track jet Higgs tagging.

Another performance comparison between VR track jet Higgs tagging and $R = 0.2$ track jet Higgs tagging was made by plotting the signal acceptance times efficiency as a function of $m_{Z'}$ for a fixed value of $m_A = 500$ GeV. This is shown in Figure 11.8. For large values of $m_{Z'}$, the VR track jet Higgs tagging technique out-performs the $R = 0.2$ track jet Higgs tagging technique in every b-tag category. However, for $m_{Z'}$ values between 1500 GeV and 2400 GeV, the $R = 0.2$ track jet technique out-performs the VR track jet technique in the 2 b-tag category. This was also observed in the pilot study of new Higgs taggers of Reference [5], and the studies concluded that this was due to one of the b-hadrons from the Higgs decay being reconstructed by the sub-sub-leading VR track jet - if two out of the three leading track jets are considered, the VR track jet technique out-performs the $R = 0.2$ track jet technique over all Higgs jet p_{T}.

The VR track jet technique out-performs the $R = 0.2$ track jet technique in the inclusive b-tag category, which suggests that the main performance improvement of the VR track jet technique is in the ability to reconstruct subjets.

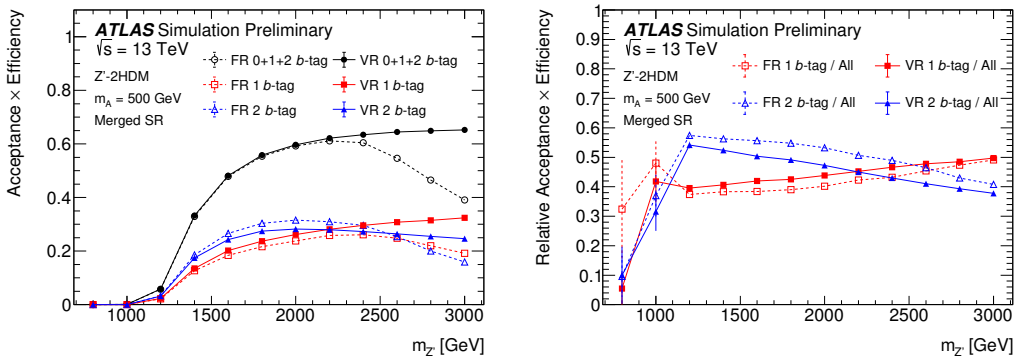

Figure 11.8: Comparison of FR and VR signal acceptance × efficiency and the relative signal acceptance × efficiency as a function of $m_{Z'}$ for a fixed $m_A = 500$ GeV [2].

Chapter 12

CONCLUSION

A search for Dark Matter using the ATLAS detector has been presented. No excess over Standard Model backgrounds was observed. The results were interpreted using a $Z'-$2HDM model, and a set of exclusion limits as a function of $m_{Z'}$ and m_A were derived. The $Z'-$2HDM limits (Figure 11.6) indicate that the search is sensitive up to an $m_{Z'}$ value of 2.8 TeV, corresponding to a Higgs boson p_{T} of roughly 1.4 TeV. Much of the sensitivity to such highly boosted Higgs bosons has been made possible by the development of new Higgs tagging techniques employing variable radius track jets as subjets with which to apply b-tagging. This is the first time this technique was used in a physics search, and it improves the expected upper limit on μ for $m_{Z'} = 3000$ GeV by a factor of three with respect to previous techniques. This new technique could also be used by other searches which predict boosted Higgs bosons.

In addition to the broader impact of the novel Higgs tagging techniques described in this thesis, including those in Appendix F, the ability to run variable radius jet clustering at non-prohibitive computational speeds has also been a goal during the course of the research presented here and is the topic of Appendix E. Variable radius clustering has applications outside of b-tagging and track jets. For example, it is a logical choice for reconstructing the decays of boosted heavy particles such as Higgs or vector bosons.

If new physics is to be found at the LHC or future colliders, it will certainly be in an elusive region of phase space where advanced reconstruction techniques will be essential. Hopefully the ideas and techniques described in this thesis can aid towards the discovery of new physics.

Finally, the ability to continue to carry out successful physics measurements and searches in the future High-Luminosity LHC environment will rely on new detector technologies. Work carried out in parallel to the Dark Matter search and Higgs tagging performance

studies to develop data acquisition for next generation pixel readout chips, including the development of software emulators of readout chips and cutting-edge techniques in data acquisition continuous integration, are presented in Appendix B. Many of the concepts and techniques described there are not only important for the future pixel data acquisition in ATLAS, but can also be applied to other detector systems and experiments.

BIBLIOGRAPHY

[1] Tony Rothman and Stephen Boughn. Can gravitons be detected? *Found. Phys.*, 36:1801–1825, 2006.

[2] ATLAS Collaboration. Search for Dark Matter Produced in Association with a Higgs Boson decaying to $b\bar{b}$ at $\sqrt{s} = 13\,\text{TeV}$ with the ATLAS Detector using $79.8\,\text{fb}^{-1}$ of proton-proton collision data. Technical Report ATLAS-CONF-2018-039, CERN, Geneva, Jul 2018.

[3] Daniel Abercrombie et al. Dark Matter Benchmark Models for Early LHC Run-2 Searches: Report of the ATLAS/CMS Dark Matter Forum. 2015.

[4] ATLAS Collaboration. Boosted Higgs ($\to b\bar{b}$) Boson Identification with the ATLAS Detector at $\sqrt{s} = 13$ TeV. Technical Report ATLAS-CONF-2016-039, CERN, Geneva, Aug 2016.

[5] ATLAS Collaboration. Variable Radius, Exclusive-k$_T$, and Center-of-Mass Subjet Reconstruction for Higgs($\to b\bar{b}$) Tagging in ATLAS. Technical Report ATL-PHYS-PUB-2017-010, CERN, Geneva, Jun 2017.

[6] Georges Aad et al. Search for dark matter produced in association with a Higgs boson decaying to two bottom quarks in pp collisions at $\sqrt{s} = 8$ TeV with the ATLAS detector. *Phys. Rev.*, D93(7):072007, 2016.

[7] Morad Aaboud et al. Search for dark matter in association with a Higgs boson decaying to b-quarks in pp collisions at $\sqrt{s} = 13$ TeV with the ATLAS detector. *Phys. Lett.*, B765:11–31, 2017.

[8] Morad Aaboud et al. Search for Dark Matter Produced in Association with a Higgs Boson Decaying to $b\bar{b}$ using 36 fb^{-1} of pp collisions at $\sqrt{s} = 13$ TeV with the ATLAS Detector. *Phys. Rev. Lett.*, 119(18):181804, 2017.

[9] Nikola Lazar Whallon, Timon Heim, Maurice Garcia-Sciveres, Arnaud Sautaux, Hideyuki Oide, Karolos Potamianos, and Shih-Chieh Hsu. Upgrade of the YARR DAQ system for the ATLAS Phase-II pixel detector readout chip. *PoS*, TWEPP-17:076, 2018.

[10] Georges Aad et al. Observation of a new particle in the search for the Standard Model Higgs boson with the ATLAS detector at the LHC. *Phys. Lett.*, B716:1–29, 2012.

[11] Serguei Chatrchyan et al. Observation of a new boson at a mass of 125 GeV with the CMS experiment at the LHC. *Phys. Lett.*, B716:30–61, 2012.

[12] C. Patrignani et al. Review of Particle Physics. *Chin. Phys.*, C40(10):100001, 2016.

[13] Richard Nisius. Measurements of the top quark mass with the ATLAS detector. *PoS*, EPS-HEP2017:453, 2017.

[14] K. A. Olive et al. Review of Particle Physics. *Chin. Phys.*, C38:090001, 2014.

[15] J. C. Kapteyn. First Attempt at a Theory of the Arrangement and Motion of the Sidereal System. *Astrophysical Journal*, 55:302, May 1922.

[16] J. H. Oort. The force exerted by the stellar system in the direction perpendicular to the galactic plane and some related problems. *Bulletin of the Astronomical Institutes of the Netherlands*, 6:249, August 1932.

[17] F. Zwicky. Die Rotverschiebung von extragalaktischen Nebeln. *Helvetica Physica Acta*, 6:110–127, 1933.

[18] V. C. Rubin and W. K. Ford, Jr. Rotation of the Andromeda Nebula from a Spectroscopic Survey of Emission Regions. *Astrophysical Journal*, 159:379, February 1970.

[19] T. S. van Albada, J. N. Bahcall, K. Begeman, and R. Sancisi. Distribution of dark matter in the spiral galaxy NGC 3198. *Astrophysical Journal*, 295:305–313, August 1985.

[20] Timothy Clifton, Pedro G. Ferreira, Antonio Padilla, and Constantinos Skordis. Modified gravity and cosmology. *Physics Reports*, 513(1):1 – 189, 2012. Modified Gravity and Cosmology.

[21] NASA et al. 1e 0657-56 with scale bar. `http://chandra.harvard.edu/photo/2006/1e0657/more.html`. Accessed: 2018-08-05.

[22] G. Hinshaw et al. Five-Year Wilkinson Microwave Anisotropy Probe (WMAP) Observations: Data Processing, Sky Maps, and Basic Results. *Astrophys. J. Suppl.*, 180:225–245, 2009.

[23] P. A. R. Ade et al. Planck 2015 results. XIII. Cosmological parameters. *Astron. Astrophys.*, 594:A13, 2016.

[24] NASA / WMAP Science Team. Universe content - wmap 9yr pie chart. `https://map.gsfc.nasa.gov/media/121236/index.html`. Accessed: 2018-08-05.

[25] Howard Baer, Ki-Young Choi, Jihn E. Kim, and Leszek Roszkowski. Dark matter production in the early universe: Beyond the thermal wimp paradigm. *Physics Reports*, 555:1 – 60, 2015. Dark matter production in the early Universe: Beyond the thermal WIMP paradigm.

[26] Jennifer M. Gaskins. A review of indirect searches for particle dark matter. *Contemp. Phys.*, 57(4):496–525, 2016.

[27] Teresa Marrodn Undagoitia and Ludwig Rauch. Dark matter direct-detection experiments. *J. Phys.*, G43(1):013001, 2016.

[28] Giorgio Busoni, Andrea De Simone, Enrico Morgante, and Antonio Riotto. On the Validity of the Effective Field Theory for Dark Matter Searches at the LHC. *Phys. Lett.*, B728:412–421, 2014.

[29] Morad Aaboud et al. Search for new phenomena in dijet events using 37 fb^{-1} of pp collision data collected at $\sqrt{s}$ =13 TeV with the ATLAS detector. *Phys. Rev.*, D96(5):052004, 2017.

[30] ATLAS Collaboration. Summary plots from the atlas exotic physics group. https://atlas.web.cern.ch/Atlas/GROUPS/PHYSICS/CombinedSummaryPlots/EXOTICS/. Accessed: 2018-08-05.

[31] E. Aprile et al. Dark Matter Search Results from a One Tonne×Year Exposure of XENON1T. 2018.

[32] Oliver Sim Brning, Paul Collier, P Lebrun, Stephen Myers, Ranko Ostojic, John Poole, and Paul Proudlock. *LHC Design Report*. CERN Yellow Reports: Monographs. CERN, Geneva, 2004.

[33] Lyndon Evans and Philip Bryant. LHC Machine. *JINST*, 3:S08001, 2008.

[34] G. Aad et al. The ATLAS Experiment at the CERN Large Hadron Collider. *JINST*, 3:S08003, 2008.

[35] The CMS Collaboration. The cms experiment at the cern lhc. *Journal of Instrumentation*, 3(08):S08004, 2008.

[36] The ALICE Collaboration. The alice experiment at the cern lhc. *Journal of Instrumentation*, 3(08):S08002, 2008.

[37] The LHCb Collaboration. The lhcb detector at the lhc. *Journal of Instrumentation*, 3(08):S08005, 2008.

[38] The TOTEM Collaboration. The totem experiment at the cern large hadron collider. *Journal of Instrumentation*, 3(08):S08007, 2008.

[39] The LHCf Collaboration. The lhcf detector at the cern large hadron collider. *Journal of Instrumentation*, 3(08):S08006, 2008.

[40] J L Pinfold. The moedal experiment at the lhc a new light on the terascale frontier. *Journal of Physics: Conference Series*, 631(1):012014, 2015.

[41] AC Team. The four main LHC experiments. Jun 1999.

[42] Ramon Cid Manzano and Xabier CidVidal. Proton source: Taking a closer look at lhc. https://www.lhc-closer.es/taking_a_closer_look_at_lhc/0.proton_source. Accessed: 2018-08-05.

[43] Georges Aad et al. Improved luminosity determination in pp collisions at sqrt(s) = 7 TeV using the ATLAS detector at the LHC. *Eur. Phys. J.*, C73(8):2518, 2013.

[44] ATLAS Collaboration. Number of interactions per crossing. https://twiki.cern.ch/twiki/bin/view/AtlasPublic/LuminosityPublicResultsRun2. Accessed: 2018-08-05.

[45] Elementary Particle Experiment Group. Epe: Atlas experiment. https://phys.washington.edu/epe-atlas-experiment.

[46] Joao Pequenao. Computer generated image of the whole ATLAS detector. Mar 2008.

[47] M. S. Alam et al. ATLAS pixel detector: Technical design report. 1998.

[48] M. Capeans, G. Darbo, K. Einsweiler, M. Elsing, T. Flick, M. Garcia-Sciveres, C. Gemme, H. Pernegger, O. Rohne, and R. Vuillermet. ATLAS Insertable B-Layer Technical Design Report. 2010.

[49] Georges Aad et al. Operation and performance of the ATLAS semiconductor tracker. *JINST*, 9:P08009, 2014.

[50] The ATLAS TRT collaboration. The atlas transition radiation tracker (trt) proportional drift tube: design and performance. *Journal of Instrumentation*, 3(02):P02013, 2008.

[51] Joao Pequenao. Computer generated image of the ATLAS inner detector. Mar 2008.

[52] Claudia Marcelloni De Oliveira. IBL installation into the inner detector of the ATLAS Experiment side C. General Photo, May 2014.

[53] ATLAS Collaboration. *ATLAS liquid-argon calorimeter: Technical Design Report*. Technical Design Report ATLAS. CERN, Geneva, 1996.

[54] ATLAS Collaboration. *ATLAS tile calorimeter: Technical Design Report*. Technical Design Report ATLAS. CERN, Geneva, 1996.

[55] Joao Pequenao. Computer Generated image of the ATLAS calorimeter. Mar 2008.

[56] ATLAS Collaboration. ATLAS muon spectrometer: Technical design report. 1997.

[57] G. Aielli et al. The RPC first level muon trigger in the barrel of the ATLAS experiment. *Nucl. Phys. Proc. Suppl.*, 158:11–15, 2006. [,11(2006)].

[58] F. Bauer et al. Construction and Test of MDT Chambers for the ATLAS Muon Spectrometer. *Nucl. Instrum. Meth.*, A461:17–20, 2001.

[59] S. Majewski, Georges Charpak, A. Breskin, and G. Mikenberg. A THIN MULTIWIRE CHAMBER OPERATING IN THE HIGH MULTIPLICATION MODE. *Nucl. Instrum. Meth.*, 217:265–271, 1983.

[60] Theodoros Argyropoulos et al. Cathode strip chambers in ATLAS: Installation, commissioning and in situ performance. *IEEE Trans. Nucl. Sci.*, 56:1568–1574, 2009.

[61] Joao Pequenao. Computer generated image of the ATLAS Muons subsystem. Mar 2008.

[62] ATLAS Collaboration. Total integrated luminosity and data quality in 2015-2017. https://twiki.cern.ch/twiki/bin/view/AtlasPublic/LuminosityPublicResultsRun2#Luminosity_Plots_for_the_2017_An. Accessed: 2018-08-05.

[63] T. Gleisberg, Stefan. Hoeche, F. Krauss, M. Schonherr, S. Schumann, F. Siegert, and J. Winter. Event generation with SHERPA 1.1. *JHEP*, 02:007, 2009.

[64] Richard D. Ball et al. Parton distributions for the LHC Run II. *JHEP*, 04:040, 2015.

[65] Simone Alioli, Paolo Nason, Carlo Oleari, and Emanuele Re. A general framework for implementing NLO calculations in shower Monte Carlo programs: the POWHEG BOX. *JHEP*, 06:043, 2010.

[66] Torbjrn Sjstrand, Stefan Ask, Jesper R. Christiansen, Richard Corke, Nishita Desai, Philip Ilten, Stephen Mrenna, Stefan Prestel, Christine O. Rasmussen, and Peter Z. Skands. An Introduction to PYTHIA 8.2. *Comput. Phys. Commun.*, 191:159–177, 2015.

[67] ATLAS Collaboration. ATLAS Run 1 Pythia8 tunes. Technical Report ATL-PHYS-PUB-2014-021, CERN, Geneva, Nov 2014.

[68] Gavin Cullen, Nicolas Greiner, Gudrun Heinrich, Gionata Luisoni, Pierpaolo Mastrolia, Giovanni Ossola, Thomas Reiter, and Francesco Tramontano. Automated One-Loop Calculations with GoSam. *Eur. Phys. J.*, C72:1889, 2012.

[69] Keith Hamilton, Paolo Nason, and Giulia Zanderighi. MINLO: Multi-Scale Improved NLO. *JHEP*, 10:155, 2012.

[70] Georges Aad et al. Measurement of the Z/γ^* boson transverse momentum distribution in pp collisions at $\sqrt{s} = 7$ TeV with the ATLAS detector. *JHEP*, 09:145, 2014.

[71] Lukas Altenkamp, Stefan Dittmaier, Robert V. Harlander, Heidi Rzehak, and Tom J. E. Zirke. Gluon-induced Higgs-strahlung at next-to-leading order QCD. *JHEP*, 02:078, 2013.

[72] B. Hespel, F. Maltoni, and E. Vryonidou. Higgs and Z boson associated production via gluon fusion in the SM and the 2HDM. *JHEP*, 06:065, 2015.

[73] Robert V. Harlander, Anna Kulesza, Vincent Theeuwes, and Tom Zirke. Soft gluon resummation for gluon-induced Higgs Strahlung. *JHEP*, 11:082, 2014.

[74] Robert V. Harlander, Stefan Liebler, and Tom Zirke. Higgs Strahlung at the Large Hadron Collider in the 2-Higgs-Doublet Model. *JHEP*, 02:023, 2014.

[75] Oliver Brein, Robert V. Harlander, and Tom J. E. Zirke. vh@nnlo - Higgs Strahlung at hadron colliders. *Comput. Phys. Commun.*, 184:998–1003, 2013.

[76] S. Agostinelli et al. Geant4a simulation toolkit. *Nuclear Instruments and Methods in Physics Research Section A: Accelerators, Spectrometers, Detectors and Associated Equipment*, 506(3):250 – 303, 2003.

[77] J. Alwall, R. Frederix, S. Frixione, V. Hirschi, F. Maltoni, O. Mattelaer, H. S. Shao, T. Stelzer, P. Torrielli, and M. Zaro. The automated computation of tree-level and next-to-leading order differential cross sections, and their matching to parton shower simulations. *JHEP*, 07:079, 2014.

[78] ATLAS Collaboration. Vertex Reconstruction Performance of the ATLAS Detector at $\sqrt{s} = 13$ TeV. Technical Report ATL-PHYS-PUB-2015-026, CERN, Geneva, Jul 2015.

[79] M Delmastro, S Gleyzer, C Hengler, M Jimenez, T Koffas, M Kuna, K Liu, Y Liu, G Marchiori, E Petit, M Pitt, E Soldatov, and K Tackmann. Photon identification efficiency measurements with the ATLAS detector using LHC Run 1 data. Technical Report ATL-COM-PHYS-2014-949, CERN, Geneva, Aug 2014.

[80] ATLAS Collaboration. Improved electron reconstruction in ATLAS using the Gaussian Sum Filter-based model for bremsstrahlung. Technical Report ATLAS-CONF-2012-047, CERN, Geneva, May 2012.

[81] ATLAS Collaboration. Electron efficiency measurements with the ATLAS detector using the 2012 LHC proton-proton collision data. Technical Report ATLAS-CONF-2014-032, CERN, Geneva, Jun 2014.

[82] Georges Aad et al. Muon reconstruction performance of the ATLAS detector in protonproton collision data at $\sqrt{s}$ =13 TeV. *Eur. Phys. J.*, C76(5):292, 2016.

[83] Matteo Cacciari, Gavin P. Salam, and Gregory Soyez. The Anti-k(t) jet clustering algorithm. *JHEP*, 04:063, 2008.

[84] Georges Aad et al. Topological cell clustering in the ATLAS calorimeters and its performance in LHC Run 1. *Eur. Phys. J.*, C77:490, 2017.

[85] M. Aaboud et al. Jet energy scale measurements and their systematic uncertainties in proton-proton collisions at $\sqrt{s}$ = 13 TeV with the ATLAS detector. *Phys. Rev.*, D96(7):072002, 2017.

[86] Georges Aad et al. Jet energy resolution in proton-proton collisions at $\sqrt{s}$ = 7 TeV recorded in 2010 with the ATLAS detector. *Eur. Phys. J.*, C73(3):2306, 2013.

[87] Georges Aad et al. Performance of pile-up mitigation techniques for jets in *pp* collisions at $\sqrt{s}$ = 8 TeV using the ATLAS detector. *Eur. Phys. J.*, C76(11):581, 2016.

[88] ATLAS Collaboration. b-tagging in dense environments. Technical Report ATL-PHYS-PUB-2014-014, CERN, Geneva, Aug 2014.

[89] ATLAS Collaboration. Optimisation and performance studies of the ATLAS *b*-tagging algorithms for the 2017-18 LHC run. Technical Report ATL-PHYS-PUB-2017-013, CERN, Geneva, Jul 2017.

[90] Morad Aaboud et al. Measurements of *b*-jet tagging efficiency with the ATLAS detector using $t\bar{t}$ events at $\sqrt{s}$ = 13 TeV. 2018.

[91] ATLAS Collaboration. Measurement of *b*-tagging Efficiency of *c*-jets in $t\bar{t}$ Events Using a Likelihood Approach with the ATLAS Detector. Technical Report ATLAS-CONF-2018-001, CERN, Geneva, Mar 2018.

[92] ATLAS Collaboration. Calibration of light-flavour jet b-tagging rates on ATLAS proton-proton collision data at $\sqrt{s} = 13$ TeV. Technical Report ATLAS-CONF-2018-006, CERN, Geneva, Apr 2018.

[93] Stephen D. Ellis and Davison E. Soper. Successive combination jet algorithm for hadron collisions. *Phys. Rev.*, D48:3160–3166, 1993.

[94] ATLAS Collaboration. Measurement of the tau lepton reconstruction and identification performance in the ATLAS experiment using pp collisions at $\sqrt{s} = 13$ TeV. Technical Report ATLAS-CONF-2017-029, CERN, Geneva, May 2017.

[95] Morad Aaboud et al. Performance of missing transverse momentum reconstruction with the ATLAS detector using proton-proton collisions at $\sqrt{s} = 13$ TeV. 2018.

[96] C Wang, S Wang, and L Zhang. Search for a high mass Higgs boson in the $H \to ZZ \to \nu\nu qq$ decay channel with the ATLAS Detector. Technical Report ATL-COM-PHYS-2014-262, CERN, Geneva, Apr 2014.

[97] ATLAS Collaboration. Object-based missing transverse momentum significance in the ATLAS detector. Technical Report ATLAS-CONF-2018-038, CERN, Geneva, Jul 2018.

[98] ATLAS Collaboration. Selection of jets produced in 13TeV proton-proton collisions with the ATLAS detector. Technical Report ATLAS-CONF-2015-029, CERN, Geneva, Jul 2015.

[99] Georges Aad et al. Search for the $b\bar{b}$ decay of the Standard Model Higgs boson in associated $(W/Z)H$ production with the ATLAS detector. *JHEP*, 01:069, 2015.

[100] Georges Aad et al. Measurement of the W charge asymmetry in the $W \to \mu\nu$ decay mode in pp collisions at $\sqrt{s} = 7$ TeV with the ATLAS detector. *Phys. Lett.*, B701:31–49, 2011.

[101] ATLAS Collaboration. Electron efficiency measurements with the ATLAS detector using the 2015 LHC proton-proton collision data. Technical Report ATLAS-CONF-2016-024, CERN, Geneva, Jun 2016.

[102] ATLAS Collaboration. Jet mass reconstruction with the ATLAS Detector in early Run 2 data. Technical Report ATLAS-CONF-2016-035, CERN, Geneva, Jul 2016.

[103] ATLAS Collaboration. Observation of $H \to b\bar{b}$ decays and VH production with the ATLAS detector. Technical Report ATLAS-CONF-2018-036, CERN, Geneva, Jul 2018.

[104] A. D. Martin, W. J. Stirling, R. S. Thorne, and G. Watt. Parton distributions for the LHC. *Eur. Phys. J.*, C63:189–285, 2009.

[105] J. Pumplin, D. R. Stump, J. Huston, H. L. Lai, Pavel M. Nadolsky, and W. K. Tung. New generation of parton distributions with uncertainties from global QCD analysis. *JHEP*, 07:012, 2002.

[106] A L Read. Presentation of search results: the cl s technique. *Journal of Physics G: Nuclear and Particle Physics*, 28(10):2693, 2002.

[107] ATLAS Collaboration. ATLAS Phase-II Upgrade Scoping Document. Technical Report CERN-LHCC-2015-020. LHCC-G-166, CERN, Geneva, Sep 2015.

[108] ATLAS Collaboration. Technical Design Report for the ATLAS Inner Tracker Strip Detector. Technical Report CERN-LHCC-2017-005. ATLAS-TDR-025, CERN, Geneva, Apr 2017.

[109] G Apollinari, I Bjar Alonso, O Brning, M Lamont, and L Rossi. *High-Luminosity Large Hadron Collider (HL-LHC): Preliminary Design Report*. CERN Yellow Reports: Monographs. CERN, Geneva, 2015.

[110] David Krohn, Jesse Thaler, and Lian-Tao Wang. Jets with Variable R. *JHEP*, 06:059, 2009.

[111] Yuri L. Dokshitzer, G. D. Leder, S. Moretti, and B. R. Webber. Better jet clustering algorithms. *JHEP*, 08:001, 1997.

[112] Martin Bauer, Ulrich Haisch, and Felix Kahlhoefer. Simplified dark matter models with two Higgs doublets: I. Pseudoscalar mediators. *JHEP*, 05:138, 2017.

[113] Daniel Guest, Julian Collado, Pierre Baldi, Shih-Chieh Hsu, Gregor Urban, and Daniel Whiteson. Jet Flavor Classification in High-Energy Physics with Deep Neural Networks. *Phys. Rev.*, D94(11):112002, 2016.

Appendix A

OUTLOOK ON DARK MATTER MODELS FOR COLLIDER SEARCHES

The mono-Higgs model and other mono-X models described in this thesis have been distinct. However, it would be desirable if a single model could be used to describe all mono-X processes. One such model is the 2HDM$-a$ model [112]. This model is being considered by the LHC DM Forum as the standard DM model for interpretations at colliders in the future.

The 2HDM$-a$ model introduces a new pseudo-scalar, a, to the two-Higgs-doublet model. As an extension to the two-Higgs-doublet model, it shares many similarities with the $Z'-$2HDM model - for example, all of the constraints on 2HDM parameters described previously apply to the 2HDM$-a$ model as well. Thus, the parameters m_H, $m_{H^\pm}$, g_χ, m_χ, and $\sin(\beta-\alpha)$ can be fixed according to the prescriptions described in Section 3.3.3.

A key difference between the two models is that a, being a pseudo-scalar, can mix with A via a mixing angle θ, and both a and A can couple to Dark Matter. The free parameters thus end up being $\tan(\beta)$, $\sin(\theta)$, m_A, and m_a.

Figures A.1, A.2, A.3, and A.4 show possible Feynman diagrams for mono-jet, mono-Z, mono-Higgs, and mono-W processes, respectively, using the 2HDM$-a$ model. Which channel would provide the best sensitivity depends strongly on the values chosen for the parameters $\tan(\beta)$, $\sin(\theta)$, m_A, and m_a.

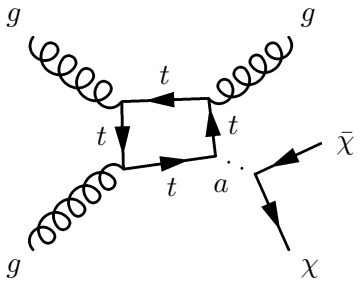

Figure A.1: A mono-jet process using a 2HDM$-a$ simplified model.

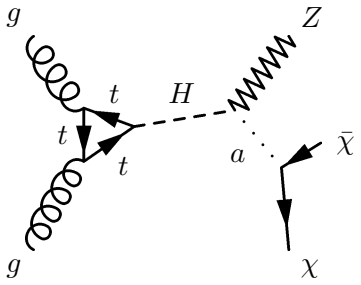

Figure A.2: A mono-Z process using a 2HDM$-a$ simplified model.

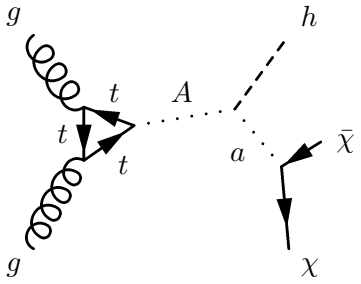

Figure A.3: A mono-Higgs process using a 2HDM$-a$ simplified model.

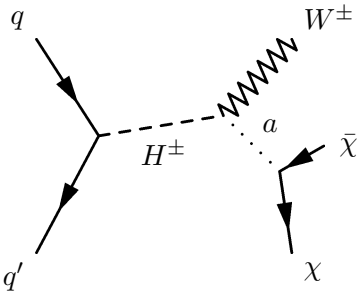

Figure A.4: A mono-W process using a 2HDM$-a$ simplified model.

Appendix B

RD53A SOFTWARE EMULATORS FOR ITK R&D

This Chapter discusses R&D work targeting next-generation Pixel detectors. Section B.1 discusses the High-Luminosity LHC upgrade, ATLAS Phase-II Upgrade, and the new Inner Tracker (ITk) planned for the upgraded ATLAS detector. Then, Section B.2 goes into depth on the development of software emulators for pixel readout chips, including pixel readout chips targeting ITk, and how such emulators can greatly aid in the development and maintenance of quality data acquisition software for future or current experiments.

B.1 The Inner Tracker Upgrade (ITk)

A major upgrade is planned for the LHC to increase its luminosity to provide 3 ab^{-1} of data[8] between 2025 and 2035 [109]. The environment of this High-Luminosity LHC (HL-LHC) will require major upgrades to the ATLAS detector in order for it to operate successfully to record and take advantage of the enormous potential dataset. Therefore, ATLAS is planning a "Phase-II Upgrade" to take place between LHC Run 3 and the first HL-LHC Run [107].

Table B.1 summarizes some of the differences in the LHC Run 2 and HL-LHC environments which motivate the need for a much improved ATLAS inner tracker. In order to meet the physics and technical challenges of the HL-LHC, the new ATLAS inner tracker, referred to as "ITk," is designed to be an all-silicon detector, consisting of five pixel detector layers and four silicon strip detector layers, both utilizing upgraded readout chip hardware and data acquisition software.

More details on the design of ITk can be found in Reference [107], and details specifically on the ITk silicon strip detector can be found in Reference [108]. Focus here will be given to developments of pixel readout chips targeting ITk and their data acquisition.

The current prototype readout chip for the future pixel detector which meets the radi-

[8] 1 $ab^{-1} = 1000$ fb^{-1}

Table B.1: A table comparing the LHC Run 2 and HL-LHC values for various metrics motivating the need for a significantly upgraded inner tracker for the ATLAS experiment.

Measure	LHC Run 2 Value	HL-LHC Value
$\langle\mu\rangle$	50	200
TID	2.5 MGy	10 MGy
L1 Trigger Rate	100 kHz	1 MHz
Innermost Layer Pixel Sensor Pitch	50 µm×250 µm	50 µm×50 µm
Readout Channel Number	$> 90 \cdot 10^6$	$> 600 \cdot 10^6$
Innermost Layer Bandwidth	160 Mb/s	5 Gb/s

ation tolerance and bandwidth demands of the HL-LHC environment is the RD53A chip. This chip contains three different flavors of analog front-end, one of which will be chosen for use in the final ATLAS pixel readout chip. These three flavors are referred to as the differential analog front-end, the linear analog front-end, and the synchronous analog front-end.

Prior to the production of RD53A, data acquisition for the chip was prepared with the use of a software emulator. Software emulators of readout chips have many uses in research and development beyond such preparatory work, and are the topic of Section B.2.

B.2 Software Emulators for Pixel Readout Chips

An important piece of technical work carried out in parallel with the Dark Matter search that is the focus of this thesis was the development of software emulators of pixel readout chips [9]. Software emulators of detector readout chips can be used in a several key ways to improve the research and development for future detectors. A major motivation for developing pixel readout chip emulators was the ability to utilize the emulators to develop data acquisition (DAQ) software for the RD53A chip, which had not yet been produced at the time the emulators were developed. By quickly mocking up the behavior of the RD53A chip, as detailed in the chip's specifications, DAQ software for the chip could be prepared

and tested before physical chips were available.

However, the usefulness of software emulators does not end with the ability to mock up future chips. Software emulators can enable laboratories without access to physical chips to develop DAQ software, greatly expanding the potential developer base for critical detector work. Software emulators also offer a method to implement continuous integration for DAQ software packages - a feature which would be very difficult to implement with hardware interfaces.

B.2.1 Yet Another Rapid Readout

The software emulators interface with the Yet Another Rapid Readout (YARR) DAQ system. YARR is used as a research and development DAQ system targeting next generation pixel readout chips, such as RD53A. It is also capable of interfacing with current generation pixel readout chips, such as FE-I4. The software component of the YARR system runs on a host computer which communicates with pixel readout chips via an intermediary PCI-e based FPGA card. The firmware for this FPGA card is simple and minimalistic, implementing only a basic i/o data buffer and communication blocks. The YARR software is responsible for performing all scan loops and data analysis. It sends commands to pixel chips to configure them, then runs scan loops, sending trigger and configuration commands to the pixel chips, and finally processes the data returned by the pixel chips to analyze the behavior and performance of the chips.

The basic design of YARR is illustrated in Figure B.1. Since the YARR software performs all data analysis, it is possible to replace the readout chip and FPGA chip portions of the YARR DAQ chain with software which can correctly interpret the commands sent by the YARR software and send data back to the YARR software.

B.2.2 Software Emulator Design and Performance

Software Emulator Design

Software emulators of the FE-I4 and RD53A pixel readout chips were developed to interface with YARR. The emulators share sending and receiving communication lines with YARR

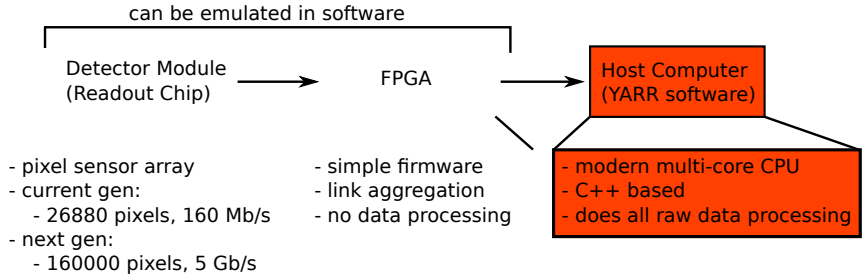

Figure B.1: The basic design of the YARR DAQ system.

via either intra-process ring buffers or inter-process ring buffers implemented in shared memory.

The emulators are capable of receiving and decoding chip configuration commands from YARR and accordingly configuring virtual global registers (GRs) of the chip and virtual pixel registers (PRs) of the chip. GRs control global settings of the readout chip, such as global threshold voltages, while PRs control local settings of each individual pixel sensor, such as local threshold voltage offsets.

To give a concrete example of the utility of PRs, consider that each pixel sensor might produce a slightly different signal for the same amount of input charge - it is then useful to have the ability to change the threshold for signal detection on a per-pixel basis so that all pixel sensors have the same response for the same input. This is the basis of a per-pixel threshold tune, such as the one shown in Figure B.7 which will be discussed below.

The emulators are also capable of receiving and decoding trigger commands from YARR. When a trigger is received, the emulators loop over an array of virtual pixel sensors and simulate hit data to send back to YARR for further processing.

The basic design of the emulators is laid out in Figure B.2, and the details of the YARR command decoding used by the FE-I4 and RD53A software emulators are laid out in Figures B.4 and B.3, respectively.

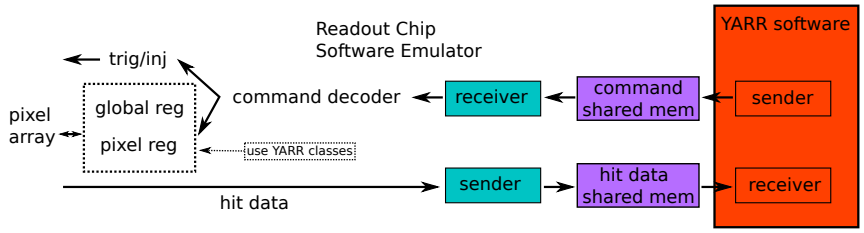

Figure B.2: The basic design of pixel readout chip software emulators.

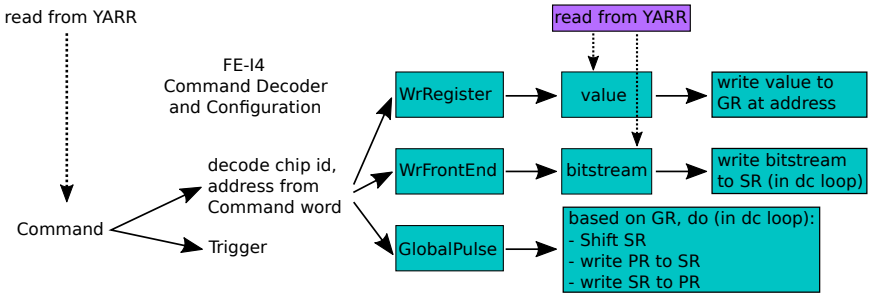

Figure B.3: The FE-I4 software emulator command decoder.

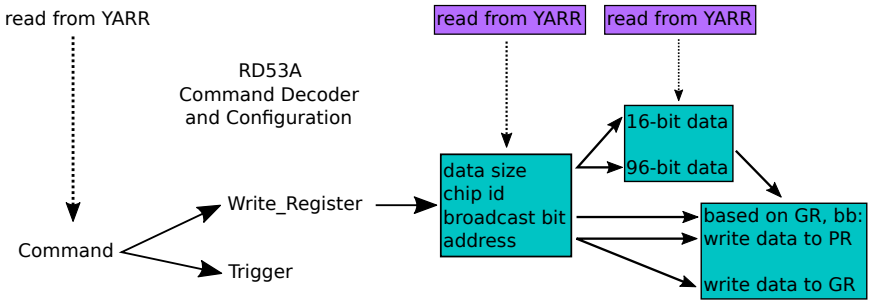

Figure B.4: The RD53A software emulator command decoder.

Hit Modeling and Results

Modeling hit data when triggers are receiving is the main simulation component of the software emulators, and this modeling is done slightly differently between the FE-I4 and the RD53A emulators as their analog front-ends are designed slightly differently.

The basics of the FE-I4 hit modelling are shown in Figure B.5. The simplified schematic shown in Figure B.5a shows that local and global threshold values are read from pixel and global registers, respectively, and are then added and compared to an input signal. The comparator counts set intervals of time that the input signal is above the total threshold voltage. This time-over-threshold, or ToT, calculation is shown graphically in Figure B.5b.

Since RD53A contains three regions of different analog front-ends, the RD53A emulator requires three different hit modeling schemes. The scheme for the differential analog front-end is shown in Figure B.6. The schematic for the differential analog front-end, shown in Figure B.6a, is not too different from that of the FE-I4 analog front-end, except that it contains two sets of global and local threshold values which when added are referred to here as V_1 (for the larger voltage) and V_2 (for the smaller voltage). The input signal is split into two routes. On one route, it is shifted up by an amount V_2, and on the other it is reversed and shifted up by an amount V_1. These two modified signals are then compared against each other by a comparator which calculates their overlap time as the ToT, shown graphically in Figure B.6b. This scheme was designed to reduce the impact of noise in the circuit as both signals will have noise contributions in the same direction post-split.

Simulating the ToT given an input charge injection and given the values stored in virtual global and pixel registers can be done by simple comparison functions. Variations in the pixel sensor responses are simulated via a gaussian smearing of local threshold values, and noise is simulated via a gaussian function which is called for each pixel at the time of each trigger. The characteristic noise of each pixel can also be configured. The result of this modeling can be illustrated in a threshold scan and global and local threshold tunes, as demonstrated in Figure B.7 which uses an FE-I4 software emulator. The initial threshold distribution is centered around $\sim 2800e$ with a large width. A global threshold tune re-centers the distribution around $\sim 2500e$, and a local threshold tune greatly improves the

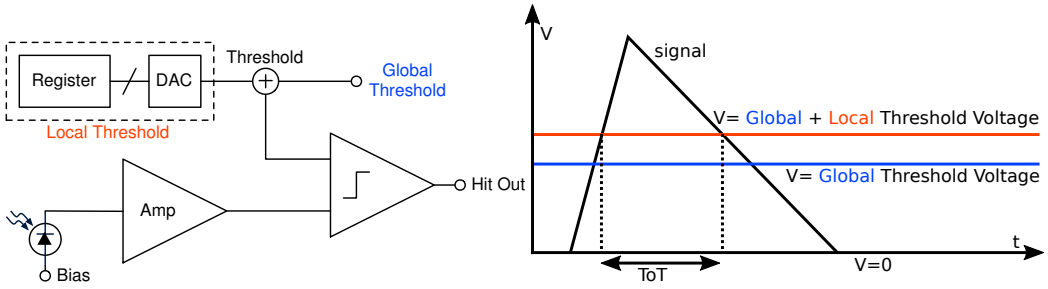

(a) (b)

Figure B.5: B.5a Simplified schematic of the FE-I4 analog front-end. B.5b Illustration of the ToT calculation for the FE-I4 analog front-end.

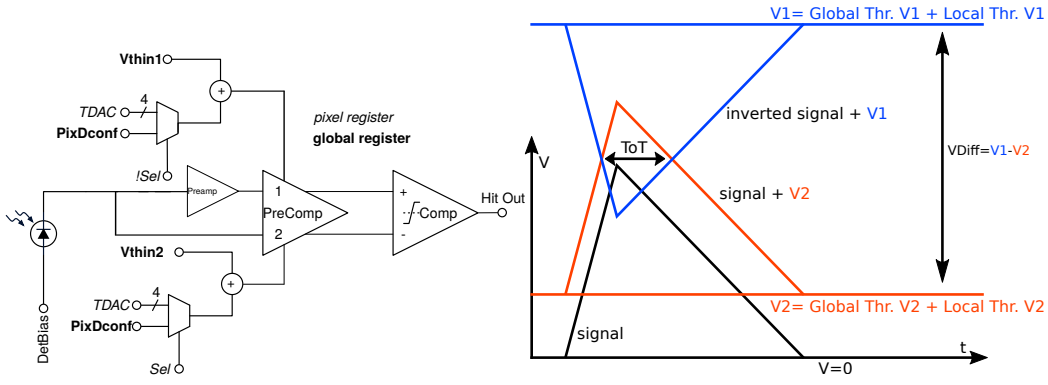

(a) (b)

Figure B.6: B.6a Schematic of the differential RD53A analog front-end. B.6b Illustration of the ToT calculation for the differential RD53A analog front-end.

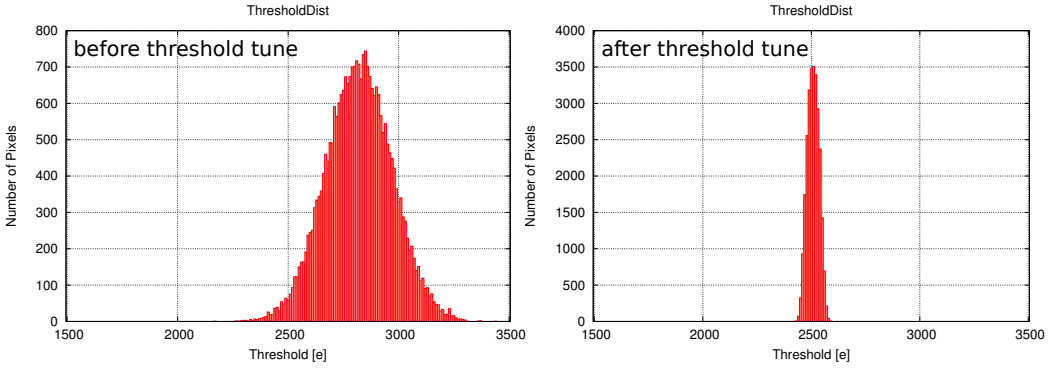

(a) (b)

Figure B.7: Threshold scans before (B.7a) and after (B.7b) applying a global and a per-pixel threshold tune using the FE-I4 software emulator.

uniformity in the virtual pixel sensor responses. The width of the threshold distribution after tuning is largely due to the level of noise simulated by the emulator.

B.2.3 Continuous Integration

Software emulators of readout chips allow a straightforward and robust way to implement continuous integration (CI) for data acquisition. CI systems are extremely useful in maintaining high quality and robust code bases - something which has historically been a weak point in collider experiments. However, CI schemes which rely on complex hardware setups involving readout chips and intermediary boards are very difficult to implement, as the CI would need to be run on dedicated servers which are always connected to, and interfaced properly with, the readout chips and intermediary boards. If any issues occur with these pieces of hardware at any time, they would need to be reset before the CI can function properly. However, replacing these pieces of hardware with software allows for the CI to run on any CI server, referred to as a "Runner," without the need to allocate and maintain a dedicated server.

The CI system designed for YARR is summarized in Figure B.8. After a developer pushes a commit to YARR's `git` repository, a Runner will checkout the developer's new

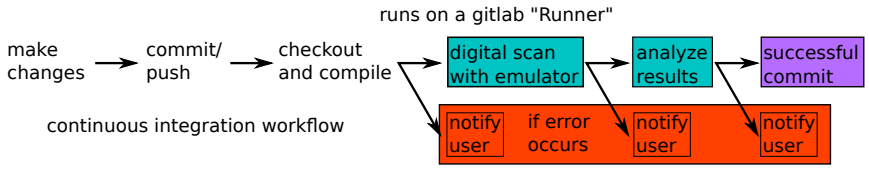

Figure B.8: The continuous integration design for YARR utilizing a pixel readout chip software emulator.

changes, compile the code, launch a digital scan interfaced with a software emulator of the FE-I4 readout chip, and run a simple bash script to analyze the results to make sure that they are consistent with expectations. If there was an error at any point in this process, for example if the code failed to compile or the analysis of results did not match what is expected, an email is sent to the developer responsible for the commit and the commit is flagged as having failed the CI.

It is then the responsibility of the development team to take these CI error notifications seriously as they either indicate that something in the code base has broken or that the expected behavior of the code base has changed. Note, however, that this system only runs a few specific tests, and could very likely miss broken code. As such, this CI scheme can and should be expanded to test more parts of the YARR software. Ideally, this CI scheme could be expanded to perform unit tests of each part of the YARR package.

It should be stressed that any CI tests beyond simple compilation of YARR software would be unfeasible without readout chip software emulators - this provides motivation for other DAQ systems to implement some form of software emulation of their hardware components in order to take advantage of CI.

Appendix C

SUMMARY OF DATA PERIODS

A break down of the luminosities for each ATLAS data taking period, and their corresponding run numbers and dates, are shown in Tables C.1, C.2, and C.3 for 2015, 2016, and 2017, respectively.

Table C.1: Table summarizing the the ATLAS 2015 dataset used.

Period	Dates	Run Numbers	$\mathcal{L}$ [pb^{-1}]
D	Aug 16 - Aug 23	276329 : 276954	51.65
E	Sep 08 - Sep 20	278880 : 279928	442.35
F	Sep 20 - Sep 26	279932 : 280368	301.69
G	Sep 27 - Oct 06	280423 : 281075	724.39
H	Oct 09 - Oct 12	281317 : 281411	264.36
J	Oct 20 - Nov 03	282625 : 284484	1434.82
D : J	2015	276329 : 284484	3219.26

Table C.2: Table summarizing the the ATLAS 2016 dataset used.

Period	Dates	Run Numbers	$\mathcal{L}$ [pb^{-1}]
A	Apr 28 - May 27	297730 : 300279	550.038
B	May 27 - Jun 06	300345 : 300908	1982.30
C	Jun 11 - Jun 21	301912 : 302393	2875.29
D	Jun 24 - Jul 10	302737 : 303560	4647.91
E	Jul 10 - Jul 16	303638 : 303892	1487.39
F	Jul 16 - Jul 25	303943 : 304494	3416.48
G	Aug 02 - Aug 17	305380 : 306451	3849.93
I	Aug 25 - Sep 10	307126 : 308084	5817.94
K	Sep 26 - Oct 03	309375 : 309759	2210.44
L	Oct 06 - Oct 26	310015 : 311481	6157.67
A : L	2016	297730 : 311481	32995.39

Table C.3: Table summarizing the the ATLAS 2017 dataset used.

Period	Dates	Run Numbers	$\mathcal{L}$ [pb^{-1}]
B	Jun 05 - Jun 30	325713 : 328393	5342.83
C	Jul 14 - Jul 24	329716 : 330470	2325.77
D	Jul 29 - Aug 10	331033 : 332304	4974.89
E	Aug 12 - Sep 04	332720 : 334779	4685.19
F	Sep 04 - Sep 13	334842 : 335290	3264.16
H	Sep 24 - Sep 27	336506 : 336719	2303.71
I	Sep 28 - Oct 12	336832 : 337833	7351.51
K	Oct 13 - Nov 10	338183 : 340453	13345.41
B : K	2017	325713 : 340453	43593.46

Appendix D

TRUTH-LEVEL SIGNAL KINEMATIC PLOTS

This Appendix presents additional plots at truth-level of various kinematic variables for the $Z'-$2HDM DM signal model. This expands upon the discussion of truth-level kinematics presented in Section 5.2.2.

For a given $m_{Z'}$, the decay products of Z' are expected to more boosted for lower m_A and less boosted for higher m_A. Figures D.1, D.2, D.3, and D.4 demonstrate this by showing the transverse momentum of of the $\chi\bar{\chi}$ system, the transverse momentum of the Higgs boson, the $\Delta\phi$ separation between the $\chi\bar{\chi}$ system and the Higgs boson, and the ΔR separation between the b-quark decay products of the Higgs boson for different values of $m_{Z'}$ and m_A. The plots show that the larger the value of $m_{Z'}$ is, or the smaller the value of m_A is for a given value of $m_{Z'}$, the larger the transverse momenta of the $\chi\bar{\chi}$ system and Higgs boson are, the larger the $\Delta\phi$ separation of the $\chi\bar{\chi}$ system and the Higgs boson is, and the smaller the ΔR separation of the b-quark decay products of the Higgs boson is. These are all kinematic trends expected of signal events with larger boosts and motivate several cuts used by the mono-Higgs analysis.

The figures also include additional plots showing the leading and sub-leading b-quark transverse momenta, and the minimum $\Delta\phi$ separation between the $\chi\bar{\chi}$ system and the leading or sub-leading b-quark. For signal models with larger boosts, the leading and sub-leading b-quark have larger, and more spread out, transverse momentum distributions, and the distribution of $\Delta\phi$ between the b-quarks becomes larger and more narrow. Again, these kinematic trends are expected of signal events with larger boosts, and motivate several cuts used by the mono-Higgs analysis.

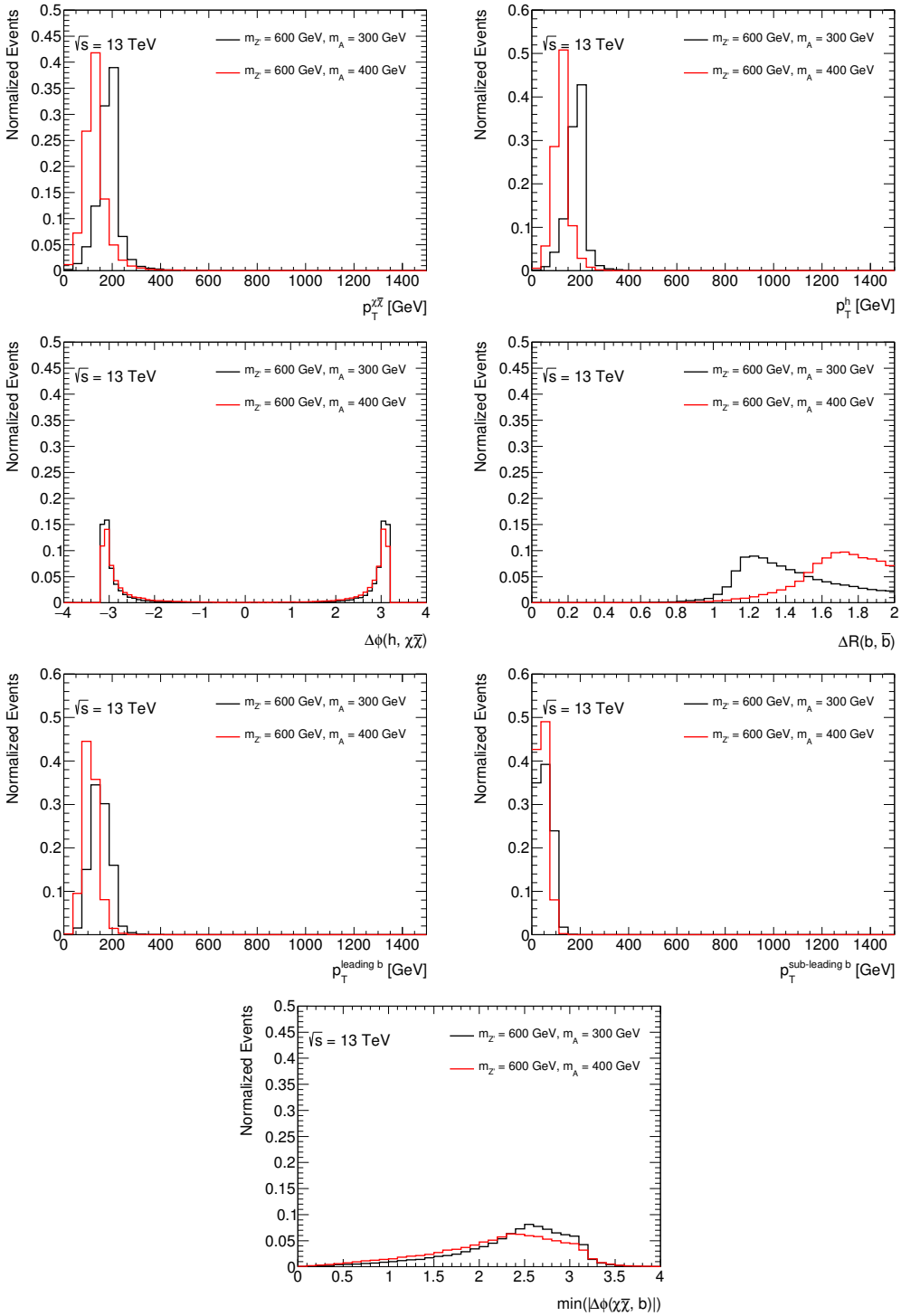

Figure D.1: Mono-Higgs truth-level kinematic distributions for $m_{Z'} = 600$ GeV.

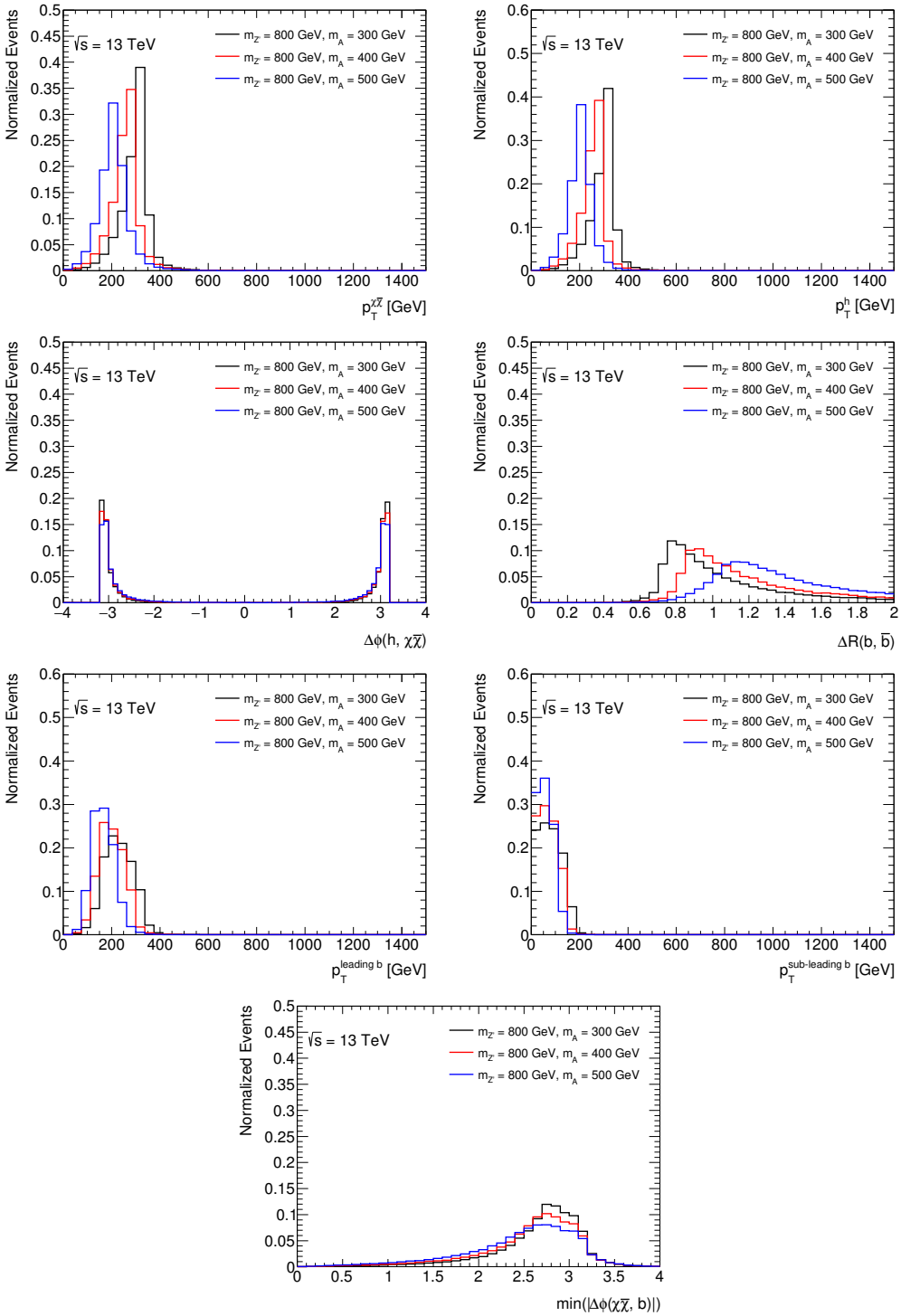

Figure D.2: Mono-Higgs truth-level kinematic distributions for $m_{Z'} = 800$ GeV.

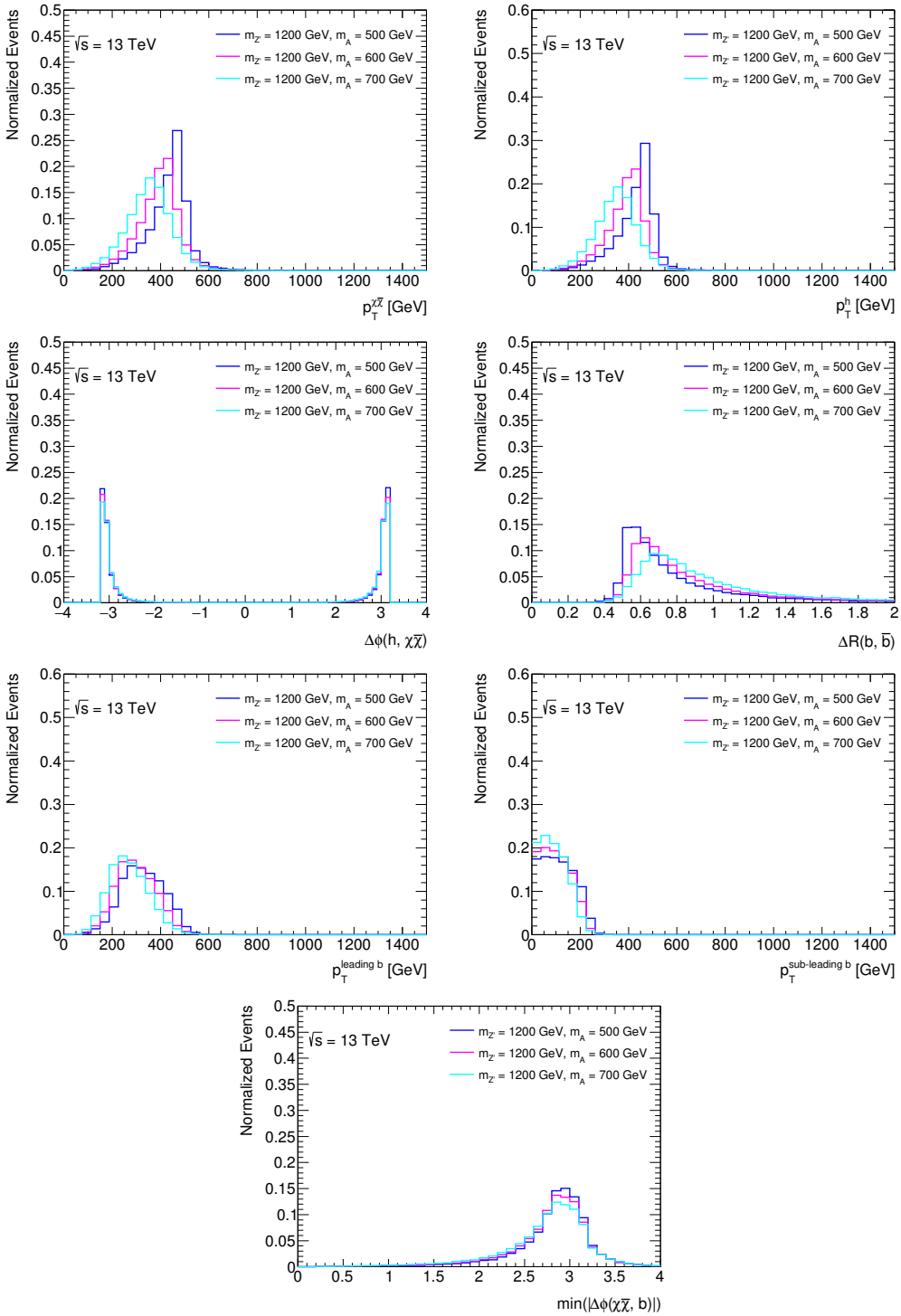

Figure D.3: Mono-Higgs truth-level kinematic distributions for $m_{Z'} = 1200$ GeV.

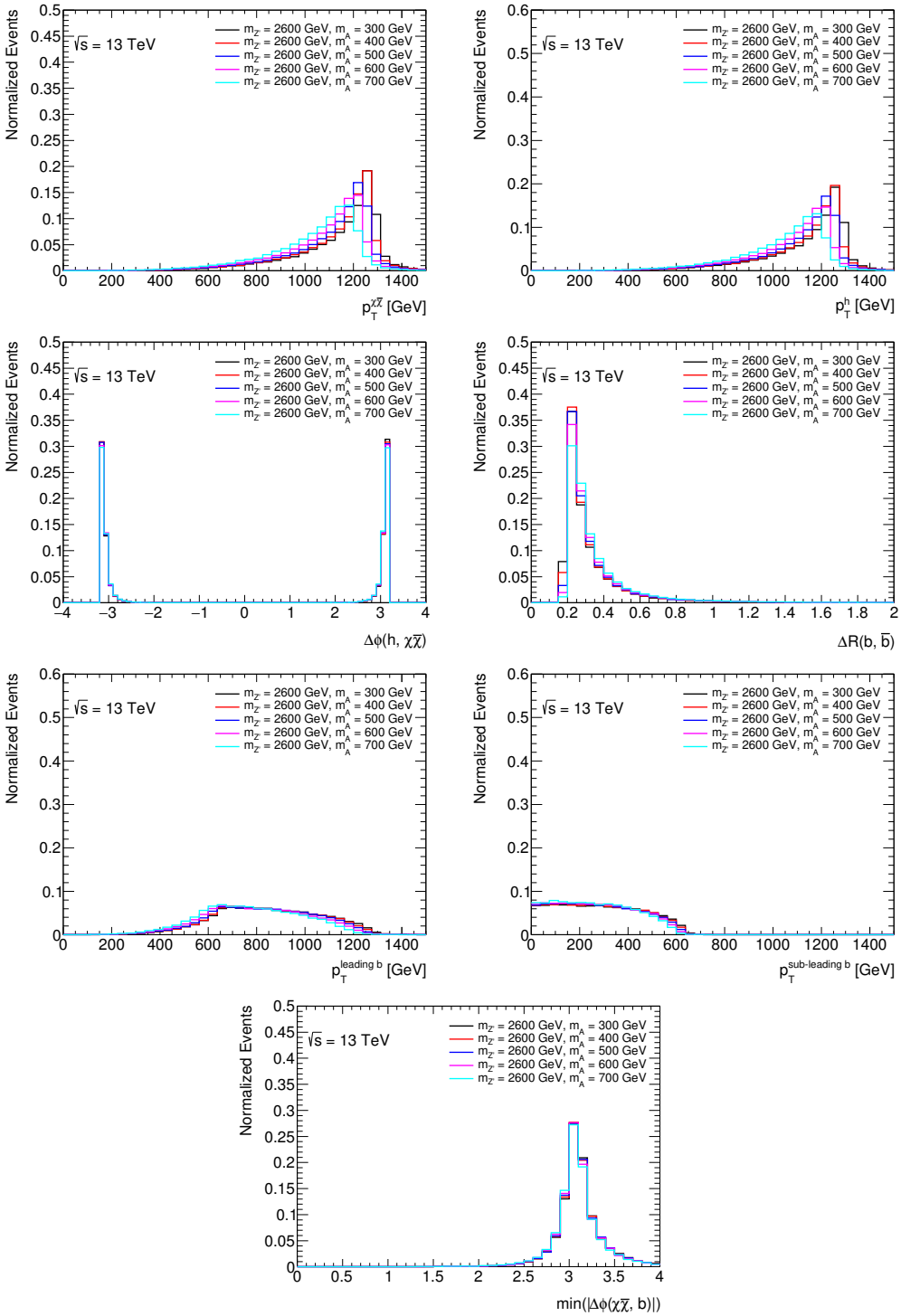

Figure D.4: Mono-Higgs truth-level kinematic distributions for $m_{Z'} = 2600$ GeV.

Appendix E

VARIABLE RADIUS JET CLUSTERING OPTIMIZATION

The variable radius (VR) jet clustering algorithm implementation used by particle physics experiments prior to 2016 was slightly worse than $O(n^2)$, which was prohibitively slow for use in searches and performance studies. In order to enable the use of VR in ATLAS searches, it was necessary to dig into the algorithm to search for ways to optimize it. Luckily, several other jet clustering implementations have achieved a lower complexity than $O(n^2)$, so adapting those implementations to work for VR provided a solution.

Several basic jet algorithms and algorithm implementations are outlined here, including their run-time complexities. The run-time performance of several implementations applied to VR jet clustering is also presented.

The implementation of VR jet clustering is now, after several discussions and demonstrations with the FastJet authors, identical to most other jet clustering techniques in the FastJet package. In particular, VR jet clustering is able to take advantage of the `N2Tiled` implementation, which can achieve a complexity much less than $O(n^2)$, depending on the radius parameter. This is what enables ATLAS and other particle physics experiments to use the variable radius jet clustering technique today.

This appendix is organized as follows. Section E.1 describes the jet clustering algorithms most used in high energy physics today. Section E.2 defines and illustrates the basic, brute force $O(n^3)$ implementation for jet clustering. Section E.3 describes a simple change to the $O(n^3)$ implementation which has a reduced complexity of $O(n^2)$. Section E.4 further optimizes the $O(n^2)$ implementation to $O(\frac{n^2}{m})$. Finally, Section E.5 presents comparisons of the computational performances of these algorithm implementations for a standard jet algorithm, and also for a VR jet algorithm.

E.1 Jet Clustering

Several clustering techniques have been developed to reconstruct QCD jets resulting from quark and gluon particle showers and hadronization. The most popular ones employed by high energy physics experiments today can be described by the follow distance measures:

$$d_{ij} = \min(k_{\mathrm{T}i}^{2p}, k_{\mathrm{T}j}^{2p}) \cdot \Delta_{ij}^2 \tag{E.1}$$

$$d_{iB} = k_{Ti}^{2p} \cdot R^2 \tag{E.2}$$

where d_{ij} is a measure of the clustering distance between the i^{th} and j^{th} input 4-momenta and d_{iB} is a measure of the clustering distance between the i^{th} input 4-momentum and the beam axis. k_{Ti} is the transverse momentum of the i^{th} input 4-momentum, Δ_{ij} is the geometric distance between the i^{th} and j^{th} input 4-momenta, and R is a radius parameter which effectively controls the maximum size of the resulting jet cone. p is typically chosen to be -1, 0, or 1, corresponding to the anti-k_{T}, Cambridge/Aachen [111], and k_{T} clustering algorithms, respectively.

The VR clustering algorithm simply replaces R in Equation E.2 with R_{eff}, defined as:

$$R_{\mathrm{eff}} = \frac{\rho}{k_{\mathrm{T}}} \tag{E.3}$$

where ρ is a free parameter and whose value can be optimized for the application. (The VR algorithm also allows for a maximum and a minimum R to be defined.) As such, the VR clustering algorithm can be used with any of the anti-k_{T}, Cambridge/Aachen, or k_{T} procedures. Theoretically, R_{eff} can be any arbitrary function of k_{T} as well, leading to a whole family of clustering algorithms. In practice, only Equation E.3 is being used as it captures the main feature of high energy jets - the higher the energy of a jet, the more collimated its constituents.

Algorithmically, VR clustering is the same as anti-k_{T}, Cambridge/Aachen, and k_{T} clustering, so it should be possible to achieve the same computational performance. While historically implemented separately, the desire to apply VR clustering to the Dark Matter analysis described in this thesis was the motivation to apply VR on top of the optimized clustering implementations of FastJet, in particular the `N2Tiled` implementation.

E.2 The `N3Dumb` *Clustering Implementation*

The most basic jet clustering implementation is a brute force approach with complexity $O(n^3)$. The implementation is summarized by the following steps:

1. calculate d_{ij} and d_{iB} for all input pseudo-jets
2. find the smallest value in the set of d_{ij}, d_{iB}
3. if it's d_{ij}, merge p_i and p_j; if it's d_{iB}, promote p_i to a jet, remove from clustering
4. repeat Steps 1-3 on the remaining pseudo-jets until no pseudo-jets remain

Step 1 has complexity $O(n^2)$, and since it will be repeated n times according to Step 4, this implementation has an overall complexity of $O(n^3)$.

To illustrate the procedure, consider the set of input pseudo-jets shown in Figure E.1a. Performing Step 1 for the first time is illustrated in Figure E.2. Then, supposing the smallest value among the d_{ij} and d_{iB} is d_{12}, for example, p_1 and p_2 are merged, resulting in the new set of pseudo-jets shown in Figure E.1b.

Performing Step 1 for a second time, now on this new set of pseudo-jets, is illustrated in Figure E.3. Now suppose the smallest distance measure is $d_{12,B}$ - p_{12} is promoted to a jet and removed from the clustering, resulting in Figure E.1c.

Performing Step 1 now for a third time on the new set of pseudo-jets is illustrated in Figure E.4, after which suppose the smallest distance measure is $d_{3,5}$ - p_3 and p_5 are merged, resulting in Figure E.1d. Performing Step 1 a fourth time on the new set of pseudo-jets is shown in Figure E.5, after which suppose $d_{4,B}$ is the smallest distance measure - p_4 is promoted to a jet and removed from the clustering, resulting in Figure E.1e. Finally, Step 1 is run on a set of inputs consisting of only the pseudo-jet p_{35}, and so $d_{35,B}$ is the smallest distance measure and p_{35} is promoted to a jet and removed from the clustering. The distribution of final clustered jets is finally shown in Figure E.1f.

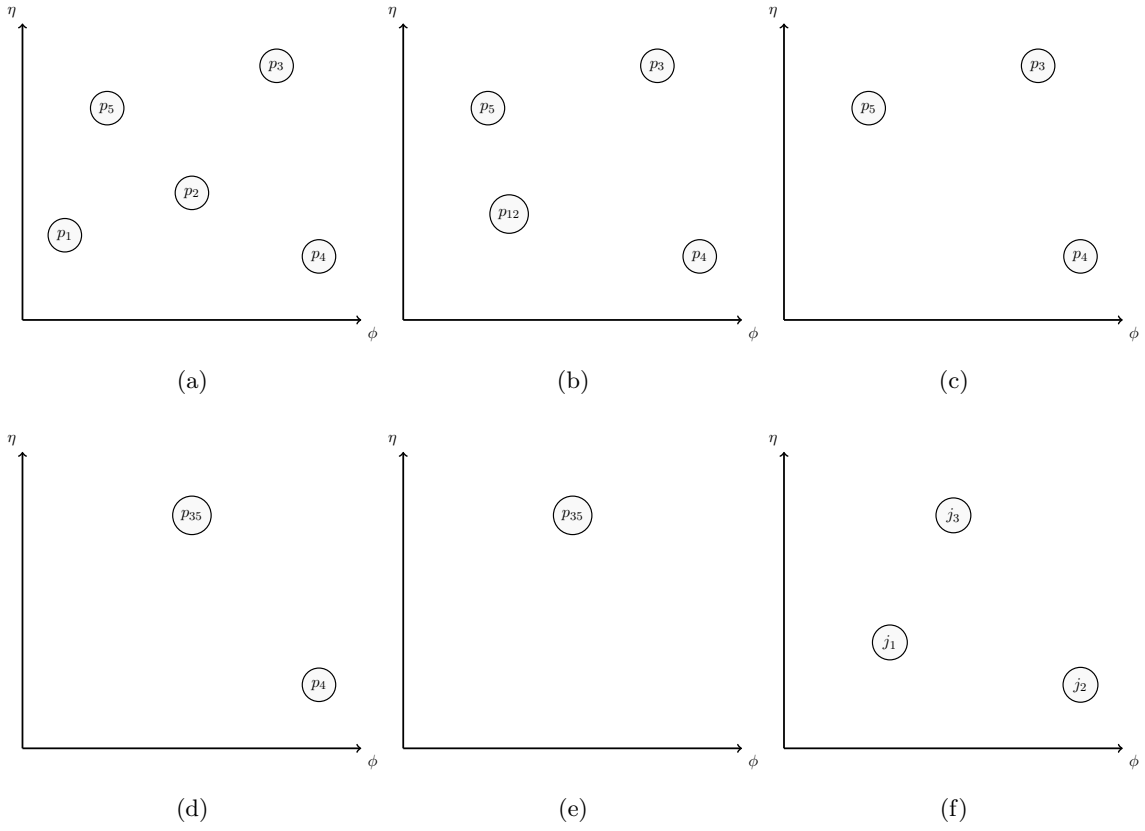

Figure E.1: E.1a–E.1e show the distribution of pseudo-jets at each iteration of the clustering algorithm. E.1f shows the final distribution of jets after all pseudo-jets have been clustered.

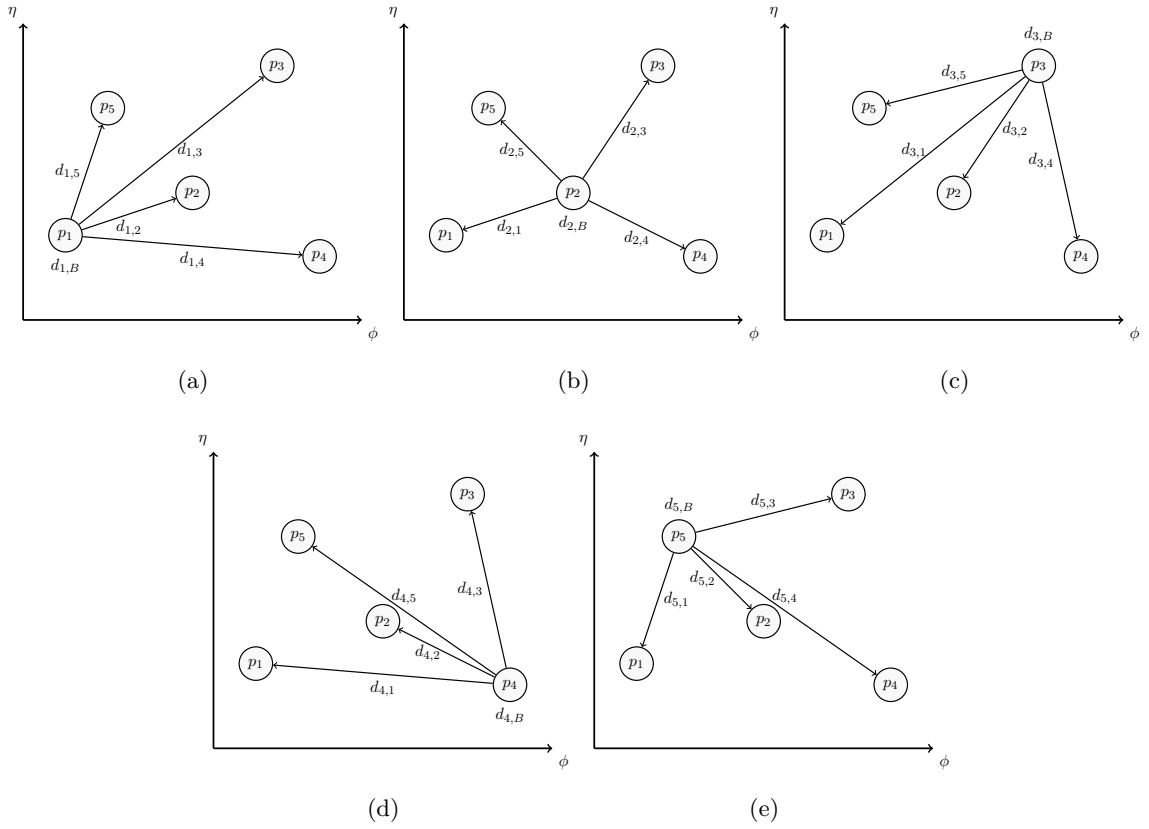

Figure E.2: The first iteration for Step 1 of the `N3Dumb` jet clustering procedure on a set of example inputs.

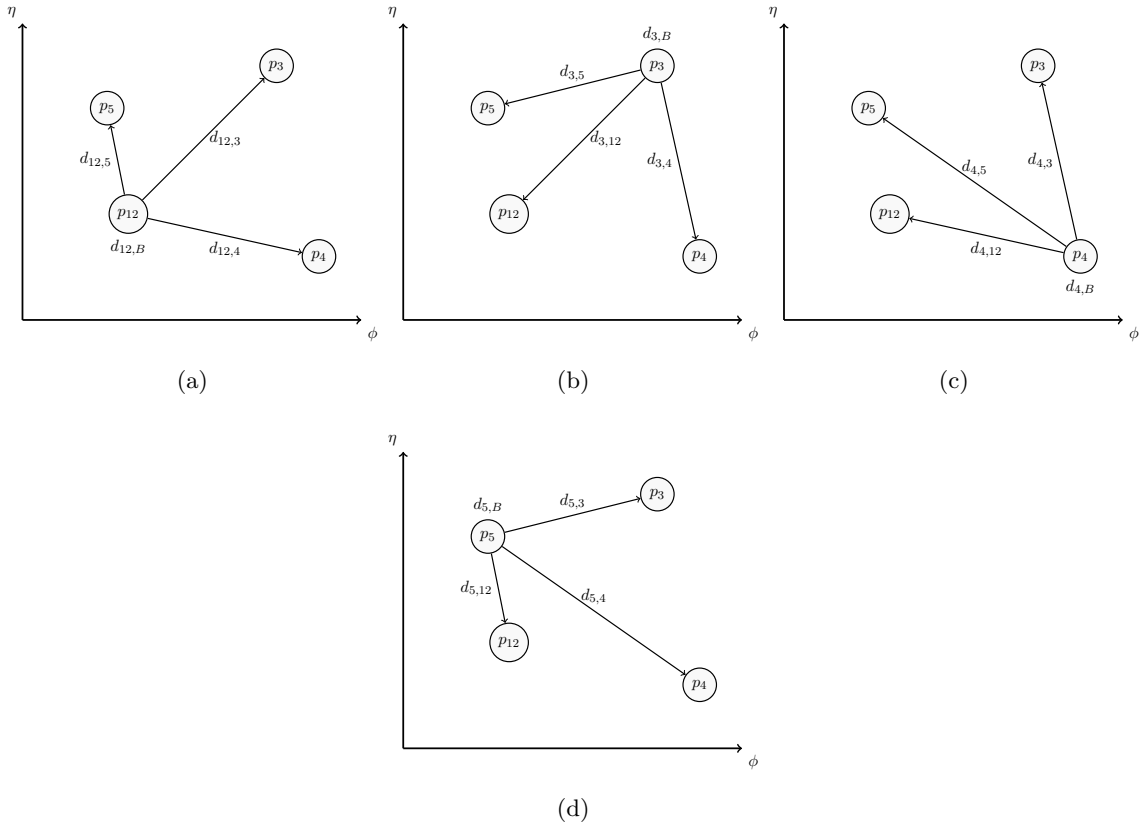

Figure E.3: The second iteration of Step 1 of the `N3Dumb` jet clustering procedure on a set of example inputs.

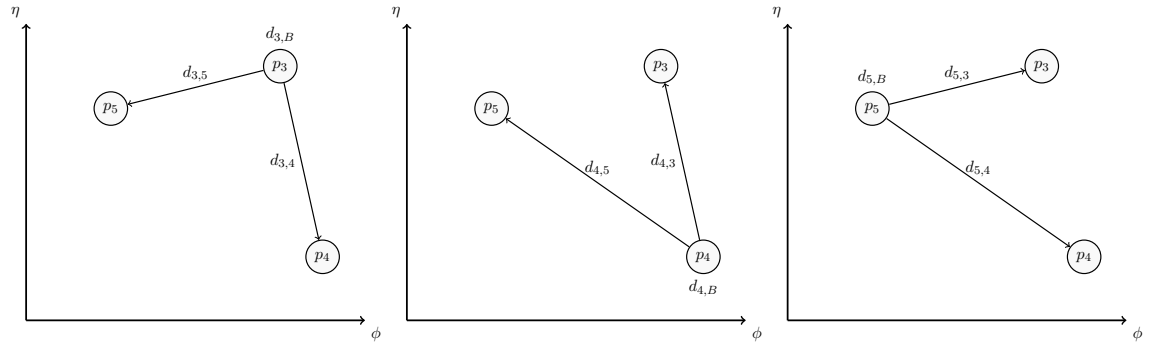

(a) (b) (c)

Figure E.4: The third iteration of Step 1 of the `N3Dumb` jet clustering procedure on a set of example inputs.

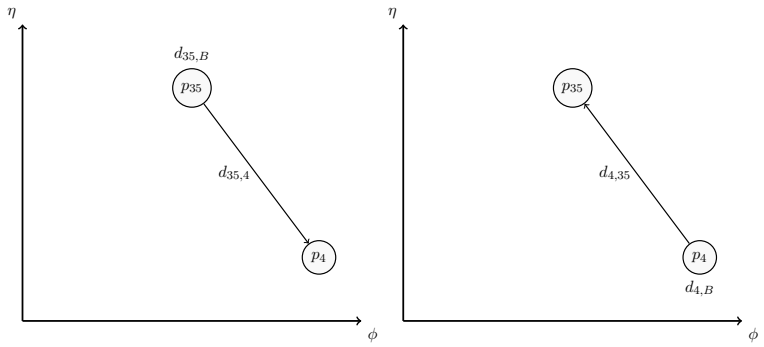

(a) (b)

Figure E.5: The fourth iteration of Step 1 of the `N3Dumb` jet clustering procedure on a set of example inputs.

Throughout the execution of this implementation, Step 1 was performed 5 times, and resulted in p_1 merging with p_2 to become a jet, p_3 merging with p_5 to become a jet, and p_4 becoming a jet.

E.3 The `N2Plain` *Clustering Implementation*

The distance measures calculated in Figures E.2b, E.2c, E.2d, and E.2e are all recalculated in Figures E.3b, E.3c, and E.3d. If instead of recalculating these distance measures at each iteration of Step 1 of the `N3Dumb` implementation, the distance measures were stored, a lot of computational time could be saved - only the distance measures of the new pseudo-jet would have to be calculated, an $O(n)$ operation. As such, the `N3Dumb` implementation can be modified to perform the following:

1. calculate d_{ij} and d_{iB} for all *new* pseudo-jets
2. find the smallest value in the set of d_{ij}, d_{iB}
3. if it's d_{ij}, merge p_i and p_j; if it's d_{iB}, promote p_i to a jet, remove from clustering
4. repeat Steps 1-3 on the remaining pseudo-jets until no pseudo-jets remain

For this new implementation, referred to as `N2Plain`, Step 1 takes $O(n^2)$ time for the first iteration, but only $O(n)$ time on each subsequent iteration, as a maximum of one new pseudo-jet will be created after Step 3. Since, after the first iteration, Step 1 will be executed $n-1$ more times, these subsequent executions of Step 1 will cumulatively take $O(n^2)$ time. Thus, the implementation as a whole takes $O(n^2)$ time.

E.4 The `N2Tiled` *Clustering Implementation*

There is a way to greatly improve the computational time of even the $O(n^2)$ `N2Plain` implementation just described. This method, referred to as `N2Tiled`, divides the 2-dimensional clustering space into tiles - then, when calculating the distance measures, it is not necessary to compare pseudo-jets in one tile with pseudo-jets in tiles which are farther away than the radius parameter, R. If the size of tiles is chosen to be R, pseudo-jets only need to be compared to other pseudo-jets in the same tile and in adjacent tiles. The algorithm implementation is summarized as follows:

1. go to the next tile
2. calculate d_{iB} for all pseudo-jets in the tile
3. calculate d_{ij} for all pseudo-jets in the tile w.r.t. other pseudo-jets in the tile
4. calculate d_{ij} for all pseudo-jets in the tile w.r.t. pseudo-jets in adjacent tiles
5. repeat Steps 1-4 for all tiles
6. find the smallest value in the set of d_{ij}, d_{iB}
7. if it's d_{ij}, merge p_i and p_j; if it's d_{iB}, promote p_i to a jet, remove from clustering
8. repeat Steps 1-7 on the remaining pseudo-jets until no pseudo-jets remain

To illustrate, suppose the implementation is considering the tile outlined in blue in Figure E.6. The implementation will calculate all d_{iB} for pseudo-jets inside the current tile (in this case there is only one). Then, the implementation will calculate the d_{ij} for all pseudo-jets inside the current tile with respect to all other pseudo-jets inside the current tile *and* adjacent tiles (i.e., the area outlined in red in Figure E.6). Again, there is no need to calculate the d_{ij} between a pseudo-jet inside the current tile and a pseudo-jet several tiles away, as long as the sides of the tiles are larger than the radius parameter, R.

After the implementation considers the tile outlined in blue in Figure E.6, it moves to the next tile and repeats the process. This is shown in Figure E.7.

By dividing the clustering space into m tiles, the computational time of the implementation can be approximated as $O(\frac{n^2}{m})$. Since m will depend on the radius parameter R, and R depends on the type of jet to be reconstructed, it is difficult to further quantify the computational improvement theoretically without picking a specific jet algorithm. However, in Section E.5, computational performances for `N2Tiled` and the other implementations discussed so far will be compared empirically for some specific jet algorithms.

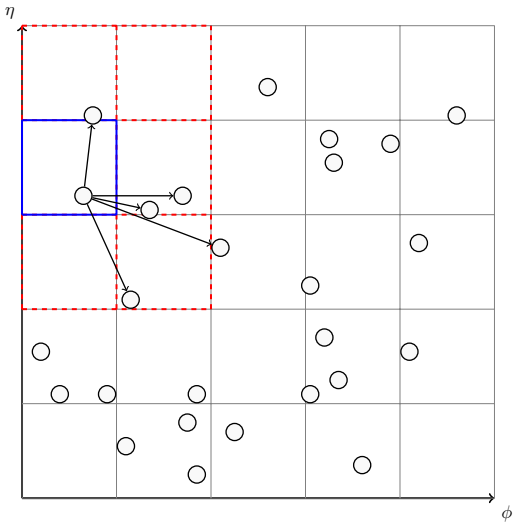

(a)

Figure E.6: Illustration of the `N2Tiled` implementation. The pseudo-jet in the blue tile is compared to pseudo-jets in adjacent tiles.

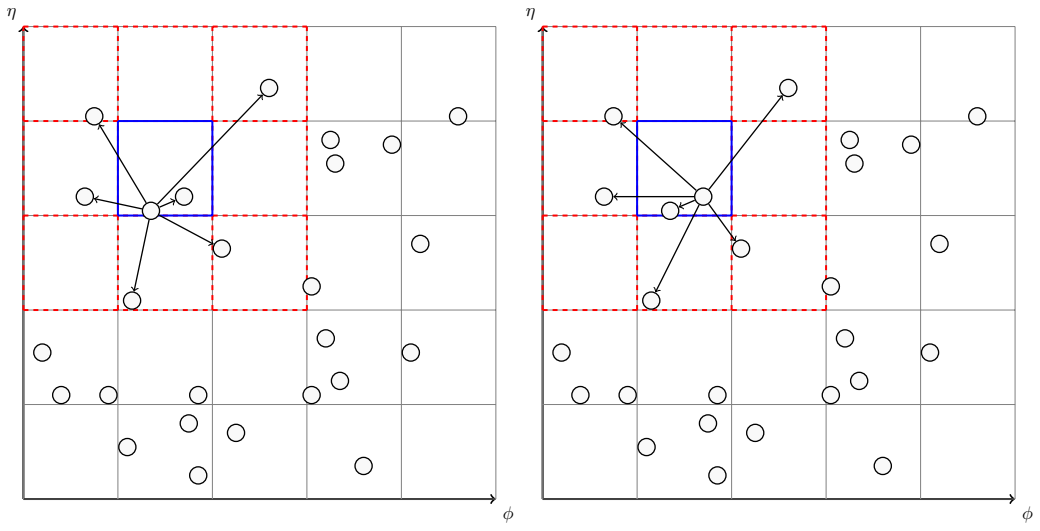

(a) (b)

Figure E.7: Illustration of the `N2Tiled` implementation. The pseudo-jets in the blue tile are compared each other and to pseudo-jets in adjacent tiles.

E.5 Empirical Performance Comparisons

While the anti-k_{T} algorithm applied on a certain set of inputs should always give the same resulting output, the implementation of the algorithm will require more or less computational resources. As described thus far, the `N3Dumb` implementation is slower than the `N2Plain` implementation which is slower than the `N2Tiled` implementation, at least from a theoretical standpoint.

To demonstrate that these algorithm implementations can be used for VR jet clustering, and to demonstrate that the use of the fast `N2Tiled` implementation in particular can greatly improve the computational time for VR jet clustering, a series of events were passed into a test program utilizing a modified FastJet to cluster the tracks. The computational time was recorded and plotted as a function of the number of input tracks. The results are shown in Figure E.8. The jet algorithms used were the anti-k_{T} algorithm with $R = 0.4$ and the VR algorithm using anti-k_{T} with $\rho = 50$ GeV, $R_{\mathrm{max}} = 0.4$, and $R_{\mathrm{min}} = 0$.

Figure E.8 shows that, indeed, the `N2Plain` and `N2Tiled` implementations were capable of outperforming the default VR clustering implementation at the time. Demonstrating this to the FastJet and FastJetContrib authors convinced them to utilize the native FastJet algorithm implementations for VR clustering.

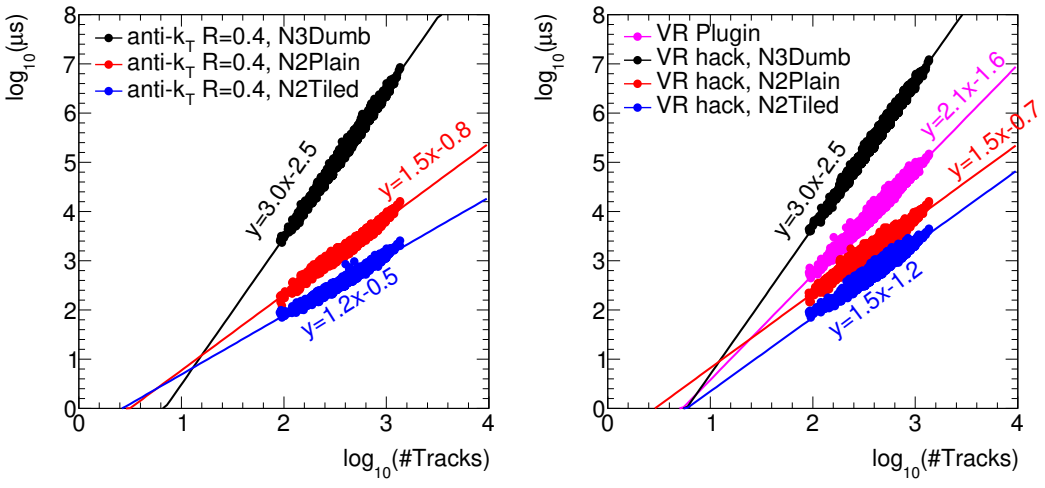

Figure E.8: Computational time as a function of the number of input tracks to various jet clustering algorithm implementations.

Appendix F
OTHER HIGGS TAGGING TECHNIQUES

The VR Higgs tagging technique is not the only new technique to try to address the issue of Higgs tagging at arbitrarily high p_{T}. Indeed, in the figures comparing VR and $R = 0.2$ track jet Higgs tagging performance shown thus far, curves for two other methods were also present. This Section describes these two other Higgs tagging techniques, and concludes with a brief mention of ideas on possible future techniques.

F.1 Exclusive-k_T Higgs Tagging

The exclusive-k_T (sometimes referred to as ExKt for short) Higgs tagging technique is illustrated in Figure F.1. The technique begins by taking all of the constituents of the trimmed large-R jet and reclustering all of them into one jet using the k_{T} algorithm. If the algorithm ended here, it would simply result in the same jet it started off with. However, the next step is to undo the very last clustering step, resulting in exactly two jets. The logic behind this is that since the k_{T} algorithm tends to cluster low p_{T} inputs first, the last two inputs to be clustered ought to represent the highest p_{T} objects comprising the final jet. Undoing this last clustering step will result in two high p_{T} subjets by construction. That these subjets truly correspond to the two b-hadrons in a Higgs jet must be tested.

Figures 7.7, 7.8, 7.9, 7.10, and 7.11 indicate that the performance of ExKt Higgs tagging is similar to that of VR Higgs tagging, and much better than $R = 0.2$ track jet Higgs tagging.

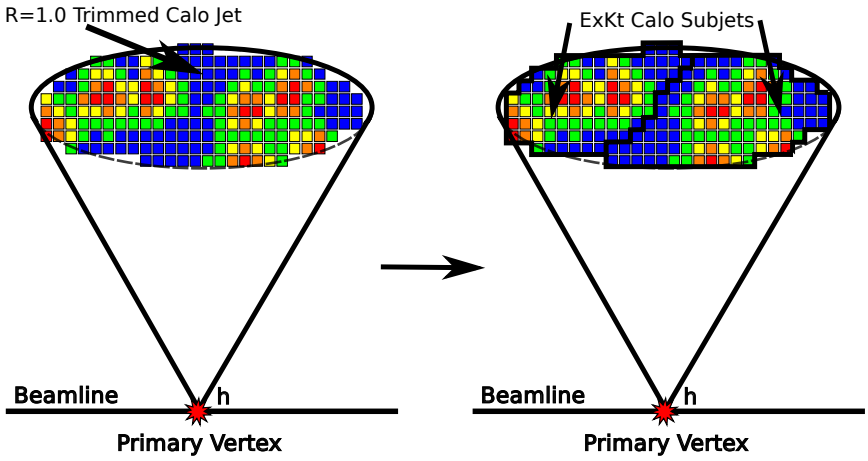

Figure F.1: A cartoon depicting the exlcusive-k_T boosted Higgs tagging technique.

F.2 Center-of-Mass (CoM) Higgs Tagging

The CoM Higgs tagging technique is illustrated in Figure F.2. The trimmed large-R jet, all of its constituents, and all tracks passing basic selection criteria and within $\Delta R < 1.0$ of the trimmed large-R jet are boosted to the center-of-mass of the trimmed large-R jet (CoM_{jet}). The calorimeter cluster constituents of the trimmed large-R jet are then clustered using the EECambridge algorithm [111] in the CoM_{jet} to form exactly two subjets. Then, in the CoM_{jet}, the tracks are associated to the two subjets. Finally, the subjets and their associated tracks are boosted back to the lab frame and used as inputs to the standard ATLAS b-tagging algorithms

The logic here is that, while two collimated decay products may be difficult to resolve in a boosted lab frame, they intuitively ought to be easier to resolve in the center-of-mass frame, where they are back to back. Figures 7.7, 7.8, 7.9, 7.10, and 7.11 indicate that the performance of CoM Higgs tagging is similar to, or even better than, that of VR Higgs tagging, and certainly much better than $R = 0.2$ track jet Higgs tagging.

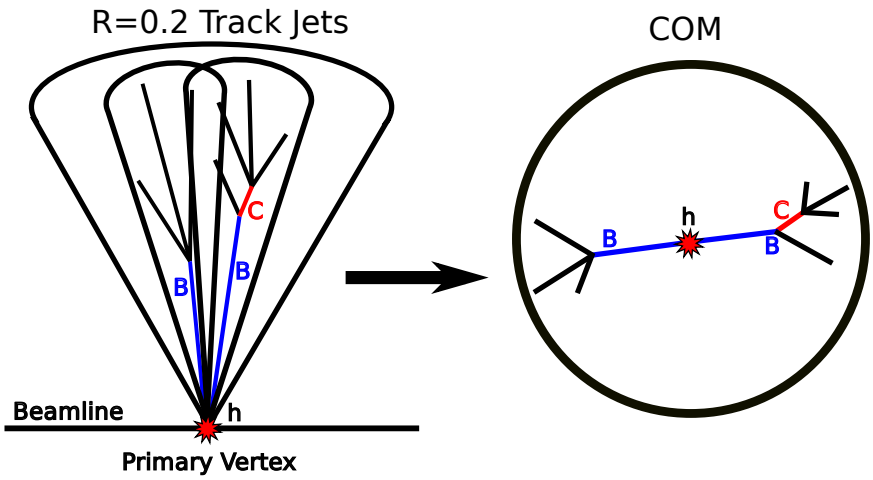

Figure F.2: A cartoon depicting the CoM boosted Higgs tagging technique.

F.3 Future Higgs Tagging Techniques

The Higgs tagging techniques studied by ATLAS have so far been based largely on b-tagging subjets. However, one can imagine an algorithm which looks holistically at all of the fundamental physics objects which can be associated to a candidate Higgs jet. This approach might take the form of a deep learning algorithm using only the trimmed large-R jet calorimeter cluster information and associated track information to form a single discriminating variable. More likely, several steps in this direction might be taken. Studies along these lines have already been started on the somewhat simpler task of b-tagging small-R jets, and these studies have been showing steady progress [113]. It is a natural extension to begin similar efforts for Higgs tagging.

Appendix G

SUMMARY OF TRIGGERS USED

A full list of the triggers used in each region is shown in Table G.1 for the 2015 data taking period, Table G.2 for the 2016 data taking period, and Table G.3 for the 2017 data taking period.

Table G.1: Table summarizing the triggers used in each analysis Region for data periods in 2015. When multiple triggers appear in the same cell, they are OR'd.

Period	0-Lepton Regions	1-Lepton Regions	2-Lepton Regions
2015 (D : J)	HLT_XE70	HLT_XE70	HLT_E24_LHMEDIUM_L1EM18VH (MC) HLT_E24_LHMEDIUM_L1EM20VH (Data) HLT_E60_LHMEDIUM HLT_E120_LHLOOSE HLT_MU20_ILOOSE_L1MU15 HLT_MU50

Table G.2: Table summarizing the triggers used in each analysis Region for data periods in 2016. When multiple triggers appear in the same cell, they are OR'd.

Period	0-Lepton Regions	1-Lepton Regions	2-Lepton Regions
2016 (A)	HLT_XE90_MHT_L1XE50	HLT_XE90_MHT_L1XE50	HLT_MU24_ILOOSE_L1MU15 (MC) HLT_MU24_ILOOSE (Data) HLT_E24_LHTIGHT_NOD0_IVARLOOSE HLT_E60_LHMEDIUM_NOD0 HLT_E60_MEDIUM HLT_E300_ETCUT HLT_E140_LHLOOSE_NOD0 HLT_MU40
2016 (B : D3)	HLT_xe90_MHT_L1XE50	HLT_XE90_MHT_L1XE50	HLT_E24_LHTIGHT_NOD0_IVARLOOSE HLT_MU24_IVARMEDIUM HLT_MU50
2016 (D4 : E)	HLT_XE100_MHT_L1XE50 HLT_XE110_MHT_L1XE50	HLT_XE100_MHT_L1XE50 HLT_XE110_MHT_L1XE50	HLT_E26_LHTIGHT_NOD0_IVARLOOSE HLT_MU24_IVARMEDIUM
2016 (F1)	HLT_XE110_MHT_L1XE50	HLT_XE110_MHT_L1XE50	HLT_MU26_IVARMEDIUM
2016 (F2 : L)	HLT_XE110_MHT_L1XE50	HLT_XE110_MHT_L1XE50	HLT_E26_LHTIGHT_NOD0_IVARLOOSE HLT_E60_LHMEDIUM_NOD0 HLT_E60_MEDIUM HLT_E300_ETCUT HLT_E140_LHLOOSE_NOD0 HLT_MU26_IVARMEDIUM HLT_MU50

Table G.3: Table summarizing the triggers used in each analysis Region for data periods in 2017. When multiple triggers appear in the same cell, they are OR'd.

Period	0-Lepton Regions	1-Lepton Regions	2-Lepton Regions
2017 (B : K)	HLT_XE110_PUFIT_L1XE55	HLT_XE110_PUFIT_L1XE55	HLT_E26_LHTIGHT_NOD0_IVARLOOSE HLT_E60_LHMEDIUM_NOD0 HLT_E140_LHLOOSE_NOD0 HLT_E300_ETCUT HLT_MU26_IVARMEDIUM HLT_MU50 HLT_MU60_0ETa105_MSONLY